A Turbulence Model for Steady

and Unsteady Boundary Layers in Strong Pressure Gradients

by

Evangelos Hytopoulos

Dissertation submitted to the Faculty of the

Virginia Polytechnic Institute and State University

in partial fulfillment of the requirements for the degree of

Ph.D

in

Aerospace Engineering

APPROVED:

Joseph A. Schetz, Chairman

Roger L. Simpson, Co-chairman

Bernard Grossman

Robert W. Walters

Max Gunzburger

J.N Reddy

February, 1994

Blacksburg, Virginia

A Turbulence Model for Steady

and Unsteady Boundary Layers in Strong Pressure Gradients

by

Evangelos Hytopoulos

Joseph A. Schetz, Chairman

Roger L. Simpson, Co-chairman

Aerospace Engineering

(ABSTRACT)

A new turbulence model designed for two-dimensional, steady and unsteady boundary layers in strong adverse pressure gradients is described. The model is developed in a rational way based on an understanding of the flow physics obtained from recent experimental observations. The turbulent shear stress is given by a mixing length model, but the variation of the mixing length in the outer region is not constant; it varies according to an integral form of the turbulence kinetic-energy equation. This approach allows for the history effects of the turbulence to be taken into account in an approximate but rational way. The form of the near-wall mixing length model is derived based on the rigorous distribution of the shear stress near the wall, and it takes into account the pressure and convection terms which become important in strong adverse pressure gradients. Since the significance of the normal stresses in turbulent kinetic-energy production is increasing as separation is approached, a model accounting for this contribution is incorporated. The model is calibrated using available experimental data. These data also indicate a change in turbulence structure near and through separation. Such a change can be significant and is accounted for here using an empirical function. The complete model was tested against steady and unsteady, two-dimensional experimental cases with adverse pressure gradient up to separation. Improved predictions compared to those obtained with other turbulence models were demonstrated. The general and rational approach that led to the derivation of the model allows the straightforward extension of the model in the region of separation. The further extension to steady and unsteady, three-dimensional cases is indicated.

Acknowledgements

The completion of the doctoral degree fulfills a dream that started 18 years ago. I would like to express my sincere appreciation to numerous individuals who provided support, guidance, and assistance during the good and bad times of my graduate career.

I would like to express my gratitude to my advisor and Committee Chairman, Dr. Joseph A. Schetz, who always directed and supported this work with great enthusiasm, patient understanding and unfailing confidence. His contribution to my academic and professional development is greatly appreciated.

I would also like to extend my gratitude to my advisor and Committee Co-Chairman, Dr. Roger L. Simpson, for his generosity with his time and expertise. His deep understanding of the physics of turbulence and his willingness to share his knowledge with me greatly facilitated my effort and widened my scientific horizons.

I would like to thank Dr. Bernard Grossman for his contribution both to this work and to my graduate education. Special thanks to Dr. Robert Walters. His answers to my numerical analysis problems have always been a constant source of confidence. His help and guidance to this work are greatly appreciated. To Dr. Max Gunzburger, I owe an enormous debt for his teaching of the Finite Element Method and his decisive help throughout this project. His clear thinking and experience provided me with answers to many knotty problems. To Dr. J.N. Reddy, I wish to express my heartfelt gratitude for his enormous contribution to my understanding and successful use of the Finite Element Method. His enlightening and motivating teaching as well as his support made him not only an excellent instructor but also a precious mentor.

Next, I would like to thank William Sydor who, as a consultant with User's Services, has always provided me with quick and accurate answers to many puzzling problems involving the use of the computers. His time and effort deserve special thanks.

Certainly, this dissertation could not have been successfully and timely completed without the help and understanding of my supervisor at Automated Analysis Corporation, Mr. Craig Birkett. I am thankful for his generous support. I would also like to thank everybody at Automated Analysis Corporation for their support and for providing the required facilities for the completion of this work. Special thanks to Mrs. Aileen Glaves for her helping me prepare a professional Ph.D defense presentation.

Sincere thanks to my friend, Ayako Koike, for her continuous support and encouragement during many troubled times of my effort. Her help and genuine friendship are greatly appreciated. I would also like to extend my appreciation to my friend, George Maglaras, for his help and support.

Special thanks to my parents, Christos and Anthoula Hytopoulos and my sister, Katerina Hytopoulou, for their love, understanding, encouragement and support over all these years. Their guidance and faith in me have provided the foundation of my education.

Finally, and most importantly, I want to thank my wife Yianna. Her patience and wholehearted support have been a unique source of strength and encouragement. Her sacrificies and love are greatly appreciated.

It is unfortunate that two of the persons that were expecting the completion of this degree with great joy are not present anymore to share this moment with me. My grandfathers, Spyros Vathis and Dimosthenis Hronas passed away while I was working for this degree. It is to those that I dedicate this work.

Table of Contents

List of Illustrations

Nomenclature

A^+	van Driest damping constant
C	constant for the outer region mixing length expression
C_d	constant for the outer region dissipation length expression
$F'_{\max}$	maximum of function $F'(y)$
$F'(y)$	$y\|\omega\|[1 - \exp(-y^+/A^+)]$
K	$= 1/2\overline{u_i u_i}$, turbulent kinetic energy
K^+	$= \dfrac{K}{u_\tau^2}$
l_m	mixing length

P mean pressure

p fluctuating pressure

Re_θ $= \rho U\theta/\mu$, Reynolds number based on momentum thickness

U_e velocity at edge of boundary layer

u_i fluctuating velocity component in the i direction

u_τ friction velocity

x_i coordinates in tensor notation

x,y,z coordinates

y^+ $= y \frac{u_\tau}{\nu}$

y_{max} value of y at which $F'(y)$ is maximum

Greek Symbols

δ boundary layer thickness

δ_{ij} Kronecker δ

δ^* displacement thickness

$\varepsilon, \bar{\varepsilon}$ dissipation of turbulent kinetic energy

ε^+ $= \varepsilon \dfrac{\nu}{u_\tau^4}$

θ momentum thickness

κ von Karman constant in log law

μ_τ eddy viscosity

ν laminar kinematic viscosity

ν_τ kinematic eddy viscosity

ρ density

σ_k constants in K - ε model

$\tau_t, -\overline{\rho uv}$ Reynolds shear stress

τ_l laminar shear stress

τ_{max} Maximum Reynolds shear stress

ω vorticity, inverse of turbulence time scale

τ_w shear stress on the wall

Subscripts

e	edge of boundary layer
in	inner
max	location of maximum stress, maximum value
o	outer

Chapter 1

1.0 Introduction

Most flows encountered in nature are turbulent, and the problem of accurately simulating turbulent flows is old and complex. The difficulties arise from several characteristics of turbulence. Turbulent flows are three-dimensional, unsteady, highly vortical and contain fluctuations in both time and space. In a fully developed turbulent flow the scales of the turbulent motion span several order of magnitudes in size. These scales can typically be 10^{-3} times the size of the domain or smaller. To resolve the motion of these elements numerically, one needs a grid that has a spacing smaller than the smallest scale. Therefore, at least 10^{9} grid points would be necessary to cover the flow domain in three dimensions [1]. Since the size of the smallest scale is a function of the Reynolds number, these numbers clearly indicate that, in spite of all the recent advances in computer technology and numerical methods, the solution of the governing equations for any practically relevant turbulent flow, requires resources that currently exceed the storage capacity and speed of present-day computers.

This difficulty has led engineers to follow a statistical approach to the problem, which was first suggested by Osborne Reynolds. The velocity and pressure fields are decomposed into a mean and a fluctuating part, and the decomposition is introduced into the Navier-Stokes equations. These equations are then time averaged over a time scale which is long compared with that of the turbulent motion. The resulting equations describe the distribution of the mean velocity and pressure in the flow. Although the process of averaging seems very appealing, it creates a new problem namely, the equations no longer constitute a closed system since they contain unknown terms representing the transport of mean momentum and mass by the turbulent motion. Solution of the system requires a mathematical model for relating these unknowns to the mean flow field. Therefore, a turbulence model is defined as a set of equations (algebraic or differential) which determine the turbulent transport terms in the mean-flow equations and thus close the system of equations. Turbulence models are based on hypotheses about turbulent processes and require empirical input in the form of constants or functions; they do not simulate details of the turbulent motion but only the effect of turbulence on the mean-flow behaviour. It is, of course, desirable in a turbulence model to achieve a good approximation for a fairly wide range of flows, but since turbulent transport processes are strongly problem-dependent, only the exact but intractable equations form a mathematical model that accurately describes the processes under all possible situations. Thus, turbulence models rely on hypotheses and experimental results and they are valid only for certain flows or at the most a range of flows.

In the present work, the focus is on accurately calculating incompressible, two-dimensional, steady and unsteady, boundary layer flows in the presence of strong adverse pressure gradient and/or separation. The wide range of practical applications that work under such conditions includes, but is not limited to, flows in diffusers, engine inlets, fans, compressors, and airfoils. The development of methods that can accurately predict those flows is of paramount importance to the engineer. Most of the prior work on turbulence modeling has been limited to steady, two-dimensional flows in the incompressible regime.

Before getting into the details of the new approach, it will be useful for the reader to have an overview of the available methodology commonly used in the area of turbulence modeling. The presentation will focus mainly on the rationale behind the models not on the detailed description of the models. The latter can be found in the literature.

1.1 Turbulence modeling

A wide variety of models are currently used for engineering calculations. Many authors have reviewed and classified those models [2,3,4,5]. According to [5], turbulence models can be classified into three major categories. The first category includes those models that make use of the Boussinesq assumption as discussed in [5]. By analogy with the laminar flow, the following assumption can be introduced for the general Reynolds stress tensor:

$$- \overline{\rho u_i u_j} = \mu_\tau \left(\frac{\partial u_i}{\partial x_j} + \frac{\partial u_j}{\partial x_i} \right) - \frac{2}{3} \delta_{ij} \left(\mu_\tau \frac{\partial u_k}{\partial x_k} + \rho K \right) \qquad [1.1.1]$$

where μ_τ is the turbulent viscosity and $K = \overline{u_i u_i}/2$ is the turbulent kinetic energy. Unlike the laminar viscosity, the eddy viscosity is not a property of the fluid, but depends on the flow itself. Using a different physical analogy, Prandtl [6] introduced the idea of the mixing length:

$$- \overline{\rho uv} = \rho l_m^2 \left| \frac{\partial U}{\partial y} \right| \frac{\partial U}{\partial y} \qquad [1.1.2]$$

The mixing length l_m can be interpreted as some *effective interaction distance* [4], similar to the mean free path between molecules used in the kinetic theory of gases. Most of the currently used turbulence models make use, in one way or another, of these two ideas. Models that fall under this category include, the zero order or algebraic models, the one equation models (based on the turbulent kinetic energy), and the two equation models (K - ε, K - ω, K - τ). The definition of the different variables will be given shortly, when the models will be described in more detail. Despite the applicability of those models to a number of different flow situations, there is no fundamental physical reason for the two ideas to hold.

The next category involves those models that solve for the Reynolds stresses directly. This category include the Reynolds stress and algebraic stress models. The transport equations, governing the development of the turbulent stresses are added to the system of mass and momentum equations, either in their differential form or in an algebraic form, respectively. These models do not assume any proportionality between the turbulent stresses and the mean strain rate. They do require though, the modeling of higher order correlations, the general behavior of which is not well known.

The third category includes models that are not entirely based on the solution of the Reynolds stress equations. Such an approach is the so-called "Large Eddy Simulation". This methodology [7, 8] attempts to resolve the large scale turbulent motion by solving a "filtered" set of equations. The effect of the scales smaller than the ones resolved on a given numerical grid, on the bigger scales is represented by a "subgrid" turbulence model. This is often an eddy viscosity type of a model. This methodology has shown promising results, but it is currently too costly to be used for realistic engineering problems.

Finally, one should not omit the Direct Numerical Simulation (DNS) [9, 10]. The attempt here is to, solve numerically for all the scales in a given turbulent flow. As discussed earlier, this requires resources not available today for realistic flow situations, and the simulations are limited to low Reynolds numbers only. Direct Numerical Simulation is a useful tool in getting a better understanding of the turbulent processes and in helping with the turbulence modeling by obtaining solutions and thus detailed "data" for a few representative flows.

Popular turbulence models

This section attempts a brief description of the most popular approaches in turbulence modeling. It is not intended as a comprehensive review of all the available models. It should inform the reader about the assumptions built into the models, their strengths and weaknesses. Several references will be given, and the interested reader is encouraged to look into them for details.

Zero order or algebraic models

All the models that fall into this category make use of the Boussinesq assumption. They appear in two forms, either as eddy viscosity or mixing length models. Since there is no universal expression valid for all flows, researchers have attempted over the years to derive expressions applicable to some simple flow situations and extend them into more complex flows. Because boundary layer flows exhibit a viscous dominated inner layer and a free shear layer like outer layer, it is expected that the modeling effort will proceed in two stages, one for each layer. The derivation of the models for the inner region of wall bounded flows is based on two major assumptions: a) the Reynolds stress is proportional to the mean strain (Boussinesq assumption), and b) the near wall shear stress is constant and equal to the wall shear stress.

These assumptions lead to the following expressions:

$$\begin{aligned} \mu_\tau &= \kappa \rho u_\tau y \quad \text{eddy viscosity} \\ l_m &= \kappa y \quad \text{mixing length} \end{aligned} \qquad [1.1.3]$$

For the outer region, it can be argued on simple physical grounds that the mixing length is proportional to the boundary layer thickness, $l_m = C\delta$. A value of 0.09

is generally accepted for C. This approach is presumed to apply to all flows, either with or without pressure gradient. Clauser [11] has developed an eddy viscosity model for the outer region by assuming a constant turbulent transport coefficient and the idea of the defect law. The final expression reads $\mu_t = 0.018 \rho U_e \delta^*$. Although the expression has been derived only for equilibrium pressure gradient boundary layers, it has been widely used for nonequilibrium ones. Cebeci and Smith [12], in attempt to extend the model to such flow conditions, have proposed a model which makes the constant dependent on the Re_θ. These models require an estimate of the boundary layer thickness, the definition and location of which are not easily determined in a Navier-Stokes code. To defeat this deficiency, Baldwin and Lomax [13] have introduced a model that replaces the product $U_e \delta^*$ with $y_{\max} F'_{\max}$. The function F' gives a measure of the slope of the profile and attains a maximum away from the wall. The location of the maximum can be used as a measure of the thickness of the boundary layer.

Two other approaches are also mentioned here. Taylor [14] assumed that the vorticity might be considered as a transferable quantity, instead of the momentum as Prandtl did. The model has the same functional form with Prandtl's model but the mixing length appearing in this expression is related to Prandtl's mixing length through a constant ($= \sqrt{2}$). Von Karman derived a similar expression where the mixing length is expressed as a function of the higher derivatives of the local velocity profile. Implicit in all these models is the assumption that the turbulence is dissipated where it is generated (production = dissipation). This means that there is no transport of turbulence in the flow field. This further implies that these models do not account for the history effect of turbulence, which becomes very important in cases of strong adverse pressure gradients.

Extension of these ideas to three dimensional flows leads to a second order tensor for the mixing length, the specification of which is not possible for general flows. Thus, most researchers have used a scalar value for all directions. The drawback of such an approach is that the directions of the shear stress and mean strain coincide. This is not supported from experimental results, especially in the near wall region.

In general, this category of models is not suitable when processes of convective or diffusive transport of turbulence are important as is the case in rapidly developing flows and recirculating flows. Also, the models perform poorly near locations where the gradient of the velocity is zero. The models predict zero Reynolds shear stresses which is not supported from experiments. Generally, these models are of little use in complex flows because of the great difficulties in specifying the mixing length.

One-equation models

The inability of the zero-equation models to account for any history effects of the turbulence and the fact that the eddy viscosity is zero when the gradient of the mean velocity is zero, has led many researchers to give up the direct link between the fluctuating velocity scale and the mean-velocity gradients and to determine this scale from a transport equation. It was the suggestion of Prandtl [15] and Kolmogorov [16] in the 1940's to let the fluctuating velocity scale to be proportional to the square root of the T.K.E ($K = \overline{u_i u_i}/2$). The eddy viscosity can then be expressed as:

$$\mu_\tau = \rho \sqrt{K}\, l \qquad [1.1.4]$$

This is the most meaningful scale since, the T.K.E is a direct measure of the intensity of the turbulence fluctuations in the three directions. As the turbulence kinetic energy is contained mainly in the large-scale fluctuations, $\sqrt{K}$ is a velocity scale for the large-scale turbulent motion. It is also an average scale for the three directions, since it doesn't distinguish between them. Therefore, eqn. (1.1.4) does not directly take into account the anisotropy of the flow. A higher or lower value of the eddy viscosity in one direction will only change the bulk value used for all three directions. The distribution of the T.K.E can be determined from a transport equation derived in exact form from the Navier-Stokes equations. For high Reynolds numbers, this equation reads [1]:

$$\frac{\partial K}{\partial t} + U_i \frac{\partial K}{\partial x_i} = - \frac{\partial}{\partial x_i} \overline{\left[u_i \left(\frac{u_j u_j}{2} + \frac{p}{\rho} \right) \right]} - \overline{u_i u_j} \frac{\partial U_i}{\partial x_j} - \nu \overline{\frac{\partial u_i}{\partial x_j} \frac{\partial u_i}{\partial x_j}} \qquad [1.1.5]$$

The terms from the left to right represent convection, diffusion due to velocity and pressure fluctuations, production by interaction of Reynolds stresses and mean-velocity gradients, and dissipation by viscous action into heat. The production term represents the transfer of kinetic energy from the mean to the turbulent motion. The same term appears with an opposite sign in the governing equation of the kinetic energy of the mean flow. Because of the new unknown correlations in the diffusion and dissipation terms, the T.K.E equation cannot be solved. To obtain a closed set of equations, these terms should be modelled. For the diffusion term, a gradient transport formulation is used and the diffusion flux is assumed proportional to the gradient of K [1]:

$$-\overline{u_i\left(\frac{u_ju_j}{2}+\frac{p}{\rho}\right)}=\frac{\nu_T}{\sigma_k}\frac{\partial K}{\partial x_i} \qquad [1.1.6]$$

where σ_k is an empirical diffusion constant. From dimensional considerations, the dissipation is modelled as:

$$\varepsilon=c\frac{K^{3/2}}{L} \qquad [1.1.7]$$

where c is another empirical constant. Introducing these models in (1.1.5), the K-equation reads:

$$\frac{\partial K}{\partial t}+U_i\frac{\partial K}{\partial x_i}=\frac{\partial}{\partial x_i}\left(\frac{\nu_\tau}{\sigma_k}\frac{\partial K}{\partial x_i}\right)+\nu_\tau\left(\frac{\partial U_i}{\partial x_j}+\frac{\partial U_j}{\partial U_i}\right)\frac{\partial U_i}{\partial x_j}-c\frac{K^{3/2}}{L} \qquad [1.1.8]$$

This is the high Reynolds number form of the transport equation for K used in most one-equation models. The model introduced so far is restricted to high Reynolds numbers only and is not applicable to the viscous sublayer near walls. Inner boundary conditions for the K equation are often supplied through the use of wall functions [17]. Another way of treating the inner boundary condition for K is to make use of the experimental observation that near the wall the convection and diffusion are negligible and thus production balances dissipation. Then, the model reduces to Prandtl's mixing length model.

Bradshaw *et al* [18] proposed a method based on the T.K.E which assumes that the turbulent shear stress is proportional to the T.K.E. along streamlines:

$$\tau_\tau = \alpha_1 \rho K \qquad \alpha_1 \simeq 0.3 \qquad [1.1.9]$$

He also proposed a different type of model for the diffusion:

$$(\rho \overline{vK} + \overline{vp}) = \tau_\tau \left(\frac{\tau_{\max}}{\rho} \right)^{1/2} G(y/\delta) \qquad [1.1.10]$$

where $G(y/\delta)$ is a universal function determined by experimental data for a flat plate flow. The set of this transformed T.K.E. equation, the momentum and the continuity equations form a system of hyperbolic equations that can be solved in a step-by-step approach. This approach has two main disadvantages [19]. The first is that it cannot easily be applied in the usually much faster momentum integral procedures. The second, and more important, is that it requires knowledge of the distribution of several empirical functions across the boundary layer, which are not known precisely, with the diffusion being the most important one.

Johnson and King [20] introduced a model which used an eddy viscosity concept, where the velocity and length scale of the turbulence are based on the maximum shear Reynolds stress. To account for convection and diffusion effects on the Reynolds shear stress development, they proposed an ODE to prescribe the maximum Reynolds shear stress development in the streamwise direction.

The model uses the same functional form for prescribing the eddy viscosity across the boundary layer as the Cebeci-Smith model [12]. This form produces a smooth transition from the inner to the outer value of the eddy viscosity. It is also a critical element of the model since ν_{t0} is used to control the rate of growth of $\overline{uv_m}$. The inner eddy viscosity is given by the following equation:

$$\nu_{ti} = D^2 \kappa y \overline{(-uv_m)}^{1/2} \qquad [1.1.11]$$

where D is the same damping term used in the Cebeci-Smith formulation. The difference compared to the typical eddy-viscosity models is the explicit linear dependence with y, instead of a quadratic one. According to the authors, this expression reduces to the usual one for zero-pressure gradient flows but behaves better for non-zero pressure gradient terms. The eddy viscosity for the outer region is assumed to have the distribution

$$\nu_{t0} = \sigma(x) 0.0168 \gamma_\kappa \int_0^\infty (U_e - U) dy \qquad [1.1.12]$$

where U_e is the local free stream velocity and γ_κ is the Klebanoff's intermittency function. The constant σ is determined at each calculation station by an iterative procedure when the following relationship is satisfied:

$$\left(\frac{\tau_m}{\rho} \right) = \nu_{\tau m} \left[\left(\frac{\partial U}{\partial y} \right) \right]_m \qquad [1.1.13]$$

The governing ODE is derived from the T.K.E equation. Using the assumptions:

$$\frac{\frac{\tau_m}{\rho}}{K_m} = a_1 = const \qquad [1.1.14]$$

$$L_m = \frac{\left(\frac{\tau_m}{\rho}\right)^{3/2}}{\varepsilon_m}$$

we end up with the following expression [21]:

$$(-\overline{uv}_m)^{1/2} = (-\overline{uv}_m)_{eq}^{1/2} - \frac{L_m U_m}{a_1(-\overline{uv}_m)} \frac{d(-\overline{uv}_m)}{dx} - \frac{L_m}{(-\overline{uv}_m)} D_m \qquad [1.1.15]$$

where D is the diffusion term and the subscript eq denotes equilibrium conditions. This equation is applicable along the path s of the maximum shear stress. The values of the different variables along this path are denoted here by the subscript m. A further simplification is introduced by assuming that s and x are nearly coincident and that y is normal to s. The extension of this assumption to unsteady flows is not obvious. The choice of $\overline{(-uv_m)}^{1/2}$ as the velocity scale is supported by the work of Perry and Schofield [22]. The quantity $\tau_{m,eq}$ is assumed to be determined from the equilibrium eddy viscosity. The turbulent diffusion term along the path of maximum Reynolds shear stress and is modelled according to the " bulk " convection hypothesis of Townsend [23].

Simpson [24] and Menter [21] have compared this model to others and concluded that it gives superior results for strong adverse pressure gradients.

Lately, a few applications of the model to unsteady flows have also been reported. Dindar and Kaynak [25] have compared the unsteady Johnson-King model predictions with those of the Baldwin-Lomax and Cebeci-Smith models for the flow over an oscillating NACA 0012 airfoil at a reduced frequency of 0.1. The comparison indicates that the Johnson -King model gives predictions in better agreement with the experimental data. Srinivasan *et al* [26] compared the performance of an algebraic eddy viscosity model based on the Renormalization Group theory [27], the Johnson-King model, the Baldwin-Barth model [28] and the Spalart-Almaras [29] for the flow over an oscillating NACA 0015 at a reduced frequency of 0.1. They found that for unsteady attached flow the first two and the last models give good agreement with experiments. For the light-stall case, the same model give only qualitatively correct results, while for the deep-stall case the Johnson-King model does not give even qualitatively correct results for the downstroke.

McDonald and Camarata [19] have proposed the use of the integral form of the T.K.E equation, which avoids the specification of the diffusion term. The integral T.K.E is used for specifying a modified mixing length value for the outer region. Applying the method to the flow studied by Goldberg [30] they obtained predictions in good agreement with the experimental data.

The area of one-equation models is not exhausted with this description. Since the new model belongs to the same category, we tried to give some more information concerning models that bear similarity with the one that is described in the present work. In conclusion, one-equation models account for convective and diffusive transport (and for the history in unsteady flows) of the turbulent velocity scale and are therefore superior to the mixing length approach when transport is important. Verification of this is provided by the performance of the Johnson-King model in 2D separated flows. These models are restricted mainly to shear layers, since it is difficult to empirically specify the length scale distribution in more complex flows. This weakness led many researchers to develop two-equation models which determine the length scale from another transport equation.

Two-equation models

The next step in deriving a more general turbulence model is the introduction of an equation for the length scale of turbulence. This length scale is characterizing the large, energy-containing eddies and can be thought of as being subjected to transport processes in a similar manner to the T.K.E. The derivation of an equation for the length scale alone is not easy conceptually and thus equations concerning combinations of the form $Z = K^m L^n$ have been proposed. All these equations possess a common form that reads:

$$\frac{\partial Z}{\partial t} + U_l \frac{\partial Z}{\partial x_l} = \frac{\partial}{\partial x_l}\left(\frac{\sqrt{K}\,L}{\sigma_z} \frac{\partial Z}{\partial x_i} \right) + c_{z1} \frac{Z}{K} P - c_{z2} Z \frac{\sqrt{K}}{L} + S \qquad [1.1.16]$$

where σ_z , c_{z1} , c_{z2} are empirical constants, P is the production of kinetic energy and S represents a secondary source term which differs according to the choice of Z. The terms represent the rate of change, the convection, the diffusion, the production and the dissipation of Z respectively. It can be shown that for different Z's all the terms except the diffusion term are equivalent. Thus the main difference rests with the diffusion term. Experience has shown that the gradient assumption for diffusion with a single constant appears to work better for Z = ε. Since the equation for this variable does not also require a source term, it has become considerably more popular than the other length scale equations.

The equation for ε can be derived in an exact form from the Navier-Stokes equations assuming high Reynolds numbers. This restriction requires modification of the model for the near wall region where the Reynolds numbers are small. The ε equation contains complex correlations whose behaviour is little known and for which fairly drastic model assumptions must be introduced in order to make the equation tractable.

The complete model can be described as follows [1]:

$$\nu_\tau = c_\mu \frac{K^2}{\varepsilon} \qquad [1.1.17]$$

This expression has been obtained using the Kolmogorov-Prandtl (eqn. 1.1.4) expression and the local equilibrium assumption.

$$\frac{\partial K}{\partial t} + U_i \frac{\partial K}{\partial x_i} = \frac{\partial}{\partial x_i}\left(\frac{\nu_\tau}{\sigma_k} \frac{\partial K}{\partial x_i} \right) + \nu_\tau \left(\frac{\partial U_i}{\partial x_j} + \frac{\partial U_j}{\partial x_i} \right) \frac{\partial U_i}{\partial x_j} - \varepsilon \qquad [1.1.18]$$

$$\frac{\partial \varepsilon}{\partial t} + U_i \frac{\partial \varepsilon}{\partial x_i} = \frac{\partial}{\partial x_i}\left(\frac{\nu_\tau}{\sigma_\varepsilon} \frac{\partial \varepsilon}{\partial x_i} \right) + c_{1\varepsilon} \frac{\varepsilon}{K} (P + G) - c_{2\varepsilon} \frac{\varepsilon^2}{K} \qquad [1.1.19]$$

where σ_k, σ_ε, $\sigma_{1\varepsilon}$, $\sigma_{2\varepsilon}$ are constants of the model. The ε - equation contains three empirical constants. The determination of the three empirical constants of the ε - equation is accomplished by applying the model to three simple flows, i.e, grid turbulence, local equilibrium (production = dissipation), and attached boundary layer flow (law of the wall). The diffusion constants σ_k and σ_ε are assumed to be close to unity and are tuned by computer optimization. There is no physical requirement for the constants to have the same values for more complex situations, in fact the do not, and thus tuning is often needed.

Despite the wide use of the model and its success in a variety of different flow situations, the K - ε model has two major shortcomings: a) it is ill-behaved approaching a solid boundary, and b) it is inaccurate for flows with adverse pressure gradient [31]. The near wall region has been treated using either "wall functions" or a number of low Reynolds number modifications. Discussion of these is beyond the scope of this presentation.

Another two-equation model that has attracted a lot of interest lately is the K - ω model of Wilcox [32,33]. The model calculates the eddy viscosity as follows:

$$\nu_\tau = a^* \frac{K}{\omega} \qquad [1.1.20]$$

where ω is the inverse of the turbulent time scale. The transport equations for K and ω are [34]:

$$\frac{D\rho K}{Dt} = \tau_{\tau,ij}\frac{\partial U_i}{\partial x_j} - \beta^* \rho\omega K + \frac{\partial}{\partial x_j}\left[(\mu + \sigma_{k1}\mu_\tau)\frac{\partial K}{\partial x_j} \right]$$

$$\frac{D\rho\omega}{Dt} = \frac{\gamma_1}{\nu_\tau}\tau_{\tau,ij}\frac{\partial U_i}{\partial x_j} - \beta_1\rho\omega^2 + \frac{\partial}{\partial x_j}\left[(\mu + \sigma_{\omega 1}\mu_\tau)\frac{\partial \omega}{\partial x_j} \right] \qquad [1.1.21]$$

where β^*, σ_{k1}, γ_1,β_1, $\sigma_{\omega 1}$ are constants of the model. The values of the constants and the near wall formulation can be found in the literature. The use of the variable ω instead of ε makes the model more computationally robust, since its near wall asymptotic behavior is better known [35]. The same authors indicate though, that the model is inconsistent in the near wall region because an exact viscous term is missing. Including this term and using the turbulence time scale (which is not singular on the wall) they have derived a new K - τ model, where τ is turbulent time scale. Menter [34] has discussed the influence of the ω freestream values on the predictions of the model and has suggested modifications that eliminate the problem. Wilcox [36] has shown comparisons with the flows used for the 1981 Stanford Conference. Overall the model performs better in strong pressure gradients than the K - ε model, and it does not employ any damping functions which is a significant advantages from a numerical point of view.

Summarizing the strengths and weaknesses of the two-equation models the following can be said. The two-equation models are the simplest models that account for the transport of both the velocity and length scale, and thus they promise success for flows for which the length scale cannot prescribed empirically in an easy way. A large number of flows have been predicted successfully with the same set of constants but experience has shown that for other flow situations, like weak shear layers and axisymmetric jets, the constants have to be replaced by functions. For unconfined recirculating flows the agreement with experiments have been found to be moderate. It should also be kept in mind that if the Boussinesq assumption is used for evaluating the Reynolds stresses, the two-equation fails whenever the Boussinesq assumption fails. Finally, assumptions have to be made in evaluating the various terms in the model transport equations. These assumptions only reflect the best understanding and intuition of the originators.

Reynolds stress models.

By Reynolds stress models we refer to these models which do not assume that the turbulent shearing stress is proportional to the rate of mean strain. The governing equations for the Reynolds stresses are derived from the dynamical equations for the fluctuating part of the velocity and can be written in the following way:

$$\frac{D\overline{u_i u_j}}{Dt} = P_{ij} + D_{ij} + \Phi_{ij} - \varepsilon_{ij} + \nu \nabla^2 \overline{u_i u_j} \qquad [1.1.22]$$

where:

$$P_{ij} = -\left(\overline{u_i u_k}\frac{\partial U_j}{\partial x_k} + \overline{u_j u_k}\frac{\partial U_i}{\partial x_k}\right) \qquad \text{Production Rate}$$

$$D_{ij} = -\frac{\partial}{\partial x_k}\overline{u_i u_j u_k} \qquad \text{Turbulent Diffusion Rate}$$

$$\Phi_{ij} = -\frac{1}{\rho}\left(\overline{u_i\frac{\partial p}{\partial x_j}} + \overline{u_j\frac{\partial p}{\partial x_i}}\right) \qquad \text{Pressure Interaction Rate}$$

$$\varepsilon_{ij} = 2\nu\,\overline{\frac{\partial u_i}{\partial x_k}\frac{\partial u_j}{\partial x_k}} \qquad \text{Dissipation Rate}$$

where the lower case letters (u_i and p) denote the fluctuating components of the variables and the capital letters (U_i) denote the time averaged-components of the variables.

As becomes obvious, the Reynolds-stress transport equation automatically accounts for the convection and diffusion of the turbulent stresses. This means that history effects are accounted for, which is an advantage over the simplest eddy viscosity models. Also the production and dissipation terms are not assumed equal and can adjust locally. This fact makes the models superior to the simpler models, in principle. Second-order closure models are obtained when the higher order correlations appearing on the right hand side of (1.1.22), are related to the Reynolds stresses, their spatial gradients, mean velocity gradient and the length scale of turbulence. The production term is straightforward and needs no modeling. The rest of the terms need to be modeled. The pressure interaction term is usually written as follows:

$$\overline{u_i \frac{\partial p}{\partial x_j}} + \overline{u_j \frac{\partial p}{\partial x_i}} = \overline{\frac{\partial (pu_i)}{\partial x_j}} + \overline{\frac{\partial (pu_j)}{\partial x_i}} - \overline{p\left(\frac{\partial u_i}{\partial x_j} + \frac{\partial u_j}{\partial x_i} \right)} \qquad [1.1.23]$$

The last term on the right side of the equation is the pressure/rate-of-strain correlation, and it is often symbolized as Π_{ij}. The other two terms represent pressure diffusion and they are grouped with the turbulent diffusion term. Thus the total turbulent diffusion term can be written as:

$$T_{ij} = -\frac{\partial}{\partial x_k}\left[\overline{u_i u_j u_k} + \frac{1}{\rho}\left(\overline{u_i p}\delta_{jk} + \overline{u_j p}\delta_{ik}\right)\right] = -\frac{\partial}{\partial x_k} T_{ijk}$$

A number of assumptions are often used in the process of modeling these terms [37]:

1. The third order transport term T_{ij} is modeled by a gradient transport hypothesis which assumes a clearcut separation of scales between mean and fluctuating fields. This separation of scales is made at the third-moment level.

2. The pressure/rate-of-strain correlation and the dissipation-rate correlation are modeled based on the ideas from homogeneous turbulence. The departures from isotropy are assumed small to allow for a Taylor-series expansion about a state of isotropic turbulence.

Near solid boundaries, the flow is strongly anisotropic, and the turbulence Reynolds number is low, thus a number of wall or damping functions are used to account for these effects.

Although attempts at modeling those terms date back to 1951, when Rotta proposed the first variant, serious use of this type of models only began in 1970, with contributions from Donaldson [38], Daly and Harlow [39], Hanjalic and Launder [40] and Launder *et al* [41]. Several models have been proposed for the different terms over the years. A review of the models as well as their performance can be found in [42].

The computational cost of those models lead researchers to seek a formulation that will allow the calculation of explicit relationships for the stresses as functions of the T.K.E., ε and the mean velocity gradients. These models are commonly known as Algebraic Stress Models. Those models are based on two assumptions: a) the ratio of the Reynolds stresses to the T.K.E. varies little along a streamline, and b) the net transport (production - dissipation) of the Reynolds stress is proportional to that of the T.K.E. [43]. These assumptions eliminate the terms that contain gradients of the Reynolds stresses and a system of algebraic equations is obtained for the stresses. These expressions together with the T.K.E. and ε equations form a two-equation model which is more general than the usual K - ε model. The expressions for the Reynolds stresses constitute eddy-viscosity relationships, where the constant is a function of the ratio (production of K) / (dissipation of K). Gatski and Speziale [44] have obtained explicit algebraic stress models for two and three dimensional turbulent flows, in noninertial frames from second-order closure models that are tensorially linear in the Reynolds stress anisotropy. The local equilibrium hypothesis is used in their derivation, thus they are a generalization of the traditional algebraic stress models including non-inertial effects. In summary, the Reynolds stress models have been considered very promising for complex flow situations. The big advantage of these models over the rest of the models is the anisotropy that they predict. Although they often give superior predictions for some flow situations, the difficulty of modeling the different terms, especially the pressure-rate-of-strain term, leads to results that are not better than those obtained from simpler models. The *ad hoc* dependence of the near wall modifications for this term on the unit normal and the satisfaction of asymptotic consistency through singular differential equations are two of the major drawbacks in the case of wall bounded flows.

Large Eddy Simulation

In Large Eddy Simulation (LES) one predicts turbulent flows by computing the dynamics of the large, energy-containing structures while modeling the effect of the smaller structures (subgrid scales) [45]. The basis for this method lies in the experimentally observed spectral character of turbulent flow fields. Generally, the large eddies are relatively long lived, anisotropic and different in every type of flow. These eddies break up to produce smaller eddies while smaller eddies interact and merge to form large eddies. This process of the production of smaller eddies through instabilities and the recombination of eddies continues until a continuous spectrum of eddies is generated. The process reaches a stationary random state when eddies are produced that are so small that the viscosity of the fluid enhances their stability and provides the means for dissipating their energy to heat. These smallest eddies have a short life and tend to be isotropic in character. This process is not generally uniform but intermittent involving such events as " bursts" and " spots " of turbulence. Large eddy simulation of turbulence computes these mechanisms for the largest eddies that contain most of the energy of the turbulence and models the effects of the eddies smaller than the finite difference mesh can resolve. By modeling only a fraction of the turbulence, the overall accuracy of the method becomes less dependent on the accuracies of the closure models than statistical models, where all of the turbulence is modeled. Also, the isotropic and, hopefully, universal character of the small scale eddies may permit the development of closure models based on sound physical arguments.

The elements of a large eddy simulation are [46]:

(i) Filtering: defines the resolvable field

(ii) Subgrid scale model: A mechanism by which energy is extracted from the resolved field

(iii) Numerical method: Space and time discretization, boundary and initial conditions

(iv) Difiltering: recovering from the resolved field information concerning the total turbulence energy. This problem becomes more critical when more than 10-20 percent of the T.K.E is in the subgrid scale motion.

In the large eddy simulation of turbulence, any flow variable f is decomposed into a mean and a fluctuating part as follows [47]:

$$f=\bar{f}+f' \qquad [1.1.24]$$

where

$$\bar{f}=\int_D G(\mathbf{x}-\mathbf{x}', \Delta)f(\mathbf{x}')d^3\mathbf{x}' \qquad [1.1.25]$$

In the last equation G is a filter function which depends on the relative position vector $\mathbf{x}-\mathbf{x}'$ in the fluid domain D and on the computational mesh size δ. The function G is normalized, i.e.,

$$\int_D G(\mathbf{x}-\mathbf{x}', \Delta)d^3\mathbf{x}' = 1 \qquad [1.1.26]$$

Unlike conventional averaging, in LES filtering in general $\bar{f}\neq 0$ and $\bar{\bar{f}}\neq\bar{f}$ since a second smoothing removes additional structure from the resolved field. The equalities hold for sharp cut-off filters.

When the filtering operation is applied to the Navier-Stokes and continuity equations one obtains the equations of motion for the large scales [45]:

$$\frac{\partial U_i}{\partial t}+\frac{\partial}{\partial x_j}(\overline{\overline{U_i}\overline{U_j}}) = -\frac{\partial P}{\partial x_i}-\frac{\partial \tau_{ij}}{\partial x_j}+\frac{1}{Re}\frac{\partial^2}{\partial x_j \partial x_j}\overline{U_i} \qquad [1.1.27]$$

$$\frac{\partial \overline{U}_i}{\partial x_i} = 0 \qquad [1.1.28]$$

in which the term

$$\tau_{ij} = \overline{\overline{U}_i u_j} + \overline{\overline{U}_j u_i} + \overline{u_i u_j} \qquad [1.1.29]$$

represents the subgrid Reynolds stresses and has to be modeled. The importance of the subgrid scale model increases as the Reynolds number increases, on a grid with fixed spacing, since the range of unresolved small scale of eddies is increasing.

The large eddy simulation has been used successfully mostly for homogeneous flows or simple inhomogeneous turbulent flow. Despite the expectations regarding the predicting capabilities of the method, the accomplishments of LES have been somewhat dissapointing until today [48].

There are, however, new developments in the field of the subgrid modeling that have brought a renaissance in LES [49].

In summary, the widest application of LES is currently in atmospheric science but there have not been many applications of LES for solution of engineering problems as yet.

This completes the section on the turbulence modeling levels used for engineering calculations. The next section outlines the new model that we propose for boundary layers in strong adverse pressure gradient.

1.2 Present work

In this work, we introduce a new, general approach to the prediction of boundary layer flows in the presence of strong pressure gradients. The assumptions built into the model have been chosen to be consistent with experimental and theoretical findings, so that the model can be rationally extended to the prediction of unsteady and three-dimensional flows. The basic features of the turbulence model include: a) the use of the integrated T.K.E. equation as a way of taking into account in an approximate, but plausible, way the "history" effects on the mixing length, b) the use of τ_{max} as the correct scaling factor, c) the specification of a rigorous model for the distribution of the shear stress profile in the near wall region, where the assumption $\tau \simeq \tau_w$, is not valid for strong adverse pressure gradients, d) the contribution of normal stresses as separation is approached, and e) the use of an empirical function that attempts to take into account the change of the turbulence structure near separation. All of this results in an auxiliary equation for the constant in the outer region mixing length model. This is coupled to a modern treatment of the differential equations of motion. Comparisons of predictions and measurements for steady and unsteady, two-dimensional cases with strong adverse pressure gradients are presented. The model gives improved results over the simple algebraic model and good agreement with the experiments.

Chapter 2

Chapter 2

2.1 Overview of the development of the model

In the following sections, a detailed description of the development of the new turbulence model is undertaken. The description is subdivided into five sections: a) the role of the T.K.E equation, b) the calculation of the ratio of the shear stress to the T.K.E, c) the normal stress contribution, d) the calculation of the dissipation term, and e) the development of the new mixing length distribution,

2.2 The role of the T.K.E equation

The need for accurate methods for the prediction of separating or separated flows under steady and unsteady conditions has led researchers to develop a number of approaches. Most of these approaches make use of established ideas for equilibrium attached turbulent boundary layers such as eddy viscosity, mixing length, turbulence kinetic energy, and entrainment models as well as empirical correlations. The major weakness of the simple algebraic models is their inability to take into account the history of turbulence. Despite this shortcoming, their predictive capability and especially their computational economy have made them popular in the prediction of a wide variety of flows, even those that lie outside their range of applicability. Higher order methods require the solution of a number of additional differential equations, thus adding numerical complexity and increasing the computational time required for obtaining a converged solution. Although these methods are based on equations that introduce more information on the physics of the flow, they also require modeling of terms that are often only poorly known. The modeling of those terms, especially in the near wall region is concerned, is problematic, and this leads to results that are not impressively better than those predicted by simpler methods [50, 42]. These observations have led us towards a simpler model that attempts to capture the physically important information rather than describe every detail of the flow field.

Reynolds stress and Turbulent Kinetic Energy equations

One of the most important pieces of information is the observation that for boundary layers in strong adverse pressure gradients and separated flows the most important scaling parameter is not the wall stress, which tends to zero, but the maximum shear stress. The general form of the Reynolds stress equations, which govern the development of the turbulent stresses, is [51]:

$$\frac{D\overline{u_i u_j}}{Dt} = P_{ij} + \Pi_{ij} - \varepsilon_{ij} - D_{ij} \qquad [2.2.1]$$

where:

Production: $$P_{ij} = -\overline{u_i u_k}\frac{\partial U_j}{\partial x_k} - \overline{u_j u_k}\frac{\partial U_i}{x_k} \qquad [2.2.1a]$$

Pressure-rate-of-strain: $$\Pi_{ij} = \frac{1}{\rho}\overline{p\left(\frac{\partial u_i}{\partial x_j} + \frac{\partial u_j}{\partial x_i}\right)} \qquad [2.2.1b]$$

Dissipation: $$\varepsilon_{ij} = 2\nu\overline{\left(\frac{\partial u_i}{\partial x_k}E_{jk} + \frac{\partial u_j}{\partial x_k}E_{ik}\right)} \qquad [2.2.1c]$$

Diffusion: $$D_{ij} = \frac{\partial}{\partial x_k}\left(\frac{1}{\rho}\left(\overline{pu_i}\delta_{jk} + \overline{pu_j}\delta_{ik}\right) + \overline{u_i u_j u_k} - \nu\left(\frac{\partial \overline{u_i u_j}}{\partial x_k} + \frac{\partial \overline{u_j u_k}}{\partial x_i} + \frac{\partial \overline{u_i u_k}}{\partial x_j}\right) + 2\nu\overline{u_k E_{ij}}\right) \qquad [2.2.1d]$$

The symbol E_{ij} represents the rate-of-strain, which is equal to:

$$E_{ij} = \frac{1}{2}\left(\frac{\partial u_i}{\partial x_j} + \frac{\partial u_j}{\partial x_i} \right) \qquad [2.2.1e]$$

This form of the Reynolds stress equation is not the one used in the second order turbulence modeling approach, although it is the proper form leading to the T.K.E equation with contraction of the indices i and j. For flows varying rapidly in the streamwise direction, the convection, diffusion and dissipation of the Reynolds shear stresses cannot be neglected, so models based on the equilibrium assumption are not appropriate. Since the Reynolds stress transport equations automatically account for these effects, it seems that these models are superior to the simple models, in principle. Second-order closure models are obtained when the higher order correlations appearing on the right hand side of equation (2.2.1), are related to the Reynolds stresses, their spatial gradients, mean velocity gradients and the length scale of turbulence. The production term is straightforward and needs no modeling, the rest of the terms need to be modeled. Many models have been proposed, but most of them are not adequate in the near wall region. This has led many researchers to transform the T.K.E equation into a governing equation for the development of the Reynolds shear stress. In the following paragraphs, a detailed presentation of the assumptions involved and the limitations introduced are examined.

As is already known, the exact T.K.E equation can be derived from equation (2.2.1) by contracting the indices i and j. This leads to the following expression:

$$\frac{DK}{Dt} = -\overline{u_i u_j}\frac{\partial U_i}{\partial x_j} - \frac{\partial}{\partial x_j}\left(\frac{1}{\rho}\overline{pu_j} + \overline{u_j\frac{u_i^2}{2}} - \overline{\nu u_i\left(\frac{\partial u_i}{\partial x_j} + \frac{\partial u_j}{\partial x_i}\right)}\right) - \varepsilon \qquad [2.2.2]$$

where:

$$K = \frac{1}{2}\,\overline{u_i u_i} \qquad [2.2.2a]$$

$$\varepsilon = \nu\,\overline{\frac{\partial u_i}{\partial x_k}\left(\frac{\partial u_i}{\partial x_k} + \frac{\partial u_k}{\partial x_i}\right)} \qquad [2.2.2b]$$

The first term on the right hand side of equation (2.2.2) represents the production of the T.K.E, the second term represents the diffusion of T.K.E and the third term represents the dissipation of T.K.E. One very important observation is the elimination of the pressure-rate-of-strain term, the modeling of which is a major stumbling block for the second-order closure models. The presence of the diffusion and dissipation terms makes the modeling of the T.K.E equation still problematic. These two terms are not well known and they require the introduction of empirical correlations. It would be advantageous to eliminate these terms or express them in terms of other terms that have a more well known behavior under different flow conditions. Unfortunately, very little can be done as far as the dissipation term is concerned. The diffusion term can be eliminated under special conditions. To see that, one must integrate equation (2.2.2) over a fixed volume $\mathbf{V}$. Using the Gauss theorem one obtains:

$$\frac{D}{Dt}\int_V K dV = \int_V -\overline{u_i u_j}\frac{\partial U_i}{\partial x_j} dV - \int_S \left[\overline{u_j\left(\frac{p}{\rho}+\frac{u_i u_i}{2}\right)} - 2\nu\overline{u_i E_{ij}}\right] n_j ds - \int_V \varepsilon dV \qquad [2.2.3]$$

where S is the bounding surface of the volume, and n_j is the component of the normal vector to the surface.

This equation indicates that the diffusion term disappears if the domain has solid boundaries, where the fluctuating velocities are zero. This also holds true in the freestream portion of the domain where again the fluctuating quantities become zero. In practical terms, the contribution of the wall and the freestream diffusion will be zero if the integrated T.K.E equation is used, but the contributions of the inlet and outlet boundaries are not zero. Those terms can be approximately dropped if it is assumed that the diffusion in the direction normal to the flow is much higher compared to the one in the direction of the flow. This assumption holds true in many real flows.

Because of the uncertainty in the specification of the diffusion term, it was decided that an integral approach was advantageous. The integral form has the added advantage of making the application of the model independent of some arbitrary path, such as the trace of the maximum shear stress. Such a path was needed in previous formulations in order to get an ordinary differential equation for steady, two-dimensional flows [20]. This direction was subsequently taken as simply the streamwise direction. The extension of this assumption to unsteady and/or three-dimensional cases is not obvious.

The modeling of the dissipation term requires the transformation of the T.K.E equation (2.2.2) into an equivalent form. This is the form that is usually used in the two-equation and second-order turbulence modeling. This form is as follows:

$$\frac{DK}{Dt} = -\overline{u_i u_j}\frac{\partial U_i}{\partial x_j} - \frac{\partial}{\partial x_j}\left[\overline{\frac{p}{\rho}u_j} + \overline{u_j\frac{u_i u_i}{2}}\right] + \nu\frac{\partial^2 K}{\partial x_j^2} - \nu\overline{\left(\frac{\partial u_i}{\partial x_j}\right)^2} \qquad [2.2.4]$$

This equation can be obtained from eqn. (2.2.2) by combining the viscous part of the diffusion term with the dissipation term as follows:

$$\frac{\partial}{\partial x_j}\overline{u_i\left(\frac{\partial u_i}{\partial x_j} + \frac{\partial u_j}{\partial x_i}\right)} - \overline{\left(\frac{\partial u_i}{\partial x_j} + \frac{\partial u_j}{\partial x_i}\right)\frac{\partial u_j}{\partial x_i}} = \frac{\partial^2 K}{\partial x_j^2} - \overline{\frac{\partial u_i}{\partial x_j}\frac{\partial u_i}{\partial x_j}} \qquad [2.2.5]$$

The only difference between the two forms can be found in the diffusion and dissipation terms. Although this "dissipation" is not the real dissipation, it is the form that is modeled by most researchers. A detailed description of the modeled form is given in a later section.

Until now, the reader has been exposed to different manipulations of the general T.K.E equation. Since the main focus in this work is the simulation of two-dimensional boundary layer flows, it is helpful to give the form of the T.K.E equation as it is used in the development of the model for such flows. It is imperative to note here that the use of the two-dimensional form of the equation does not imply any restriction for the applicability of the general model in three-dimensional flows. The T.K.E equation for two-dimensional flows follows from eqn. (2.2.4), if one sets the mean variables and their derivatives in the z-direction equal to zero:

$$
\begin{aligned}
&\frac{\partial K}{\partial t} + U\frac{\partial K}{\partial x} + V\frac{\partial K}{\partial y} = -\overline{u^2}\,\frac{\partial U}{\partial x} - \overline{uv}\,\frac{\partial U}{\partial y} - \overline{v^2}\,\frac{\partial V}{\partial y} \\
&- \overline{vu}\,\frac{\partial V}{\partial x} - \frac{\partial}{\partial x}\left(\overline{\frac{p}{\rho}u} + \overline{uk} - \nu\frac{\partial K}{\partial x}\right) - \frac{\partial}{\partial y}\left(\overline{\frac{p}{\rho}v} + \overline{vk} - \nu\frac{\partial K}{\partial y}\right) - \bar{\varepsilon}
\end{aligned}
\qquad [2.2.6]
$$

where $k = 1/2u_i^2$ and $\bar{\varepsilon}$ is equal to the last term of equation 2.2.4. This term involves derivatives of the fluctuating quantities with respect to z. These derivatives cannot be dropped since they exist inside the average, thus this term is not expanded here.

Following Launder *et al* [52], the form of the T.K.E equation for plane two-dimensional boundary layer flow at high Reynolds numbers, keeping the production due to normal stresses term is:

$$
\begin{aligned}
&\frac{\partial K}{\partial t} + U\frac{\partial K}{\partial x} + V\frac{\partial K}{\partial y} + (\overline{u^2} - \overline{v^2})\frac{\partial U}{\partial x} \\
&+ \overline{uv}\,\frac{\partial U}{\partial y} + \frac{\partial}{\partial y}\left(\overline{\frac{p}{\rho}v} + \overline{vk}\right) + \bar{\varepsilon} = 0
\end{aligned}
\qquad [2.2.7]
$$

As mentioned earlier, the integral form of the equation offers several advantages. Integration of equation (2.2.7) across the viscous layer eliminates the diffusion and laminar viscous dissipation terms exactly within the limits of the boundary layer assumptions. Making use of the continuity equation and integrating by parts, the previous equation can be written in the following form:

$$\int_V \left(\frac{\partial K}{\partial t} + \frac{\partial UK}{\partial x} + \overline{uv}\,\frac{\partial U}{\partial y} + (\overline{u^2} - \overline{v^2})\,\frac{\partial U}{\partial x} + \bar{\varepsilon} \right) dy \;+\; VK\Big]_0^{\infty} = 0 \qquad [2.2.8]$$

The last term of the equation is identically equal to zero in many cases since $V = 0$ on the wall and usually $K = 0$ in the freestream. The equation has no dependence on the y coordinate. The only independent variables are the time (t), and the spatial component (x). This will eventually lead to a governing equation that is a Partial Differential Equation (P.D.E) in case of unsteady flow, or an Ordinary Differential Equation (O.D.E) in case of steady flow.

Up to this point, the analysis has not led to an equation that governs the development of the shear stress in the flow. This transformation is the result of the experimental observation that the ratio of the Reynolds shear stress to the T.K.E is almost constant across the boundary layer (at least for $.15\delta \leq y \leq 0.75\delta$). The constant has a value between 0.25 and 0.30 for zero pressure gradient. The ratio assumes lower values for adverse pressure gradient flows [53] but most methods assume a constant value independent of the flow situation. As shown later, this is not the case with the present model. Before transforming the equation, a few definitions must be introduced:

$$\tau = -\rho\overline{uv}$$
$$K = \frac{1}{2}\overline{u_i^2} \qquad [2.2.9a]$$

$$F = 1 + \frac{(\overline{u^2} - \overline{v^2})\dfrac{\partial U}{\partial x}}{\overline{uv}\dfrac{\partial U}{\partial y}} \qquad [2.2.9b]$$

$$\frac{\tau}{\rho K} = A_1 F^{-p} = \alpha_1 \qquad [2.2.9c]$$

$$\frac{\tau}{\tau_{\max}} = f(x, \frac{y}{\delta}, t) \qquad [2.2.9d]$$

$$\bar{\varepsilon} = \frac{\tau^{3/2}}{L_d} \qquad [2.2.9e]$$

The factor F expresses the ratio of the total turbulence energy production to the shear-stress-related turbulence energy production [54]. An average value of 1.25 has been determined experimentally for the exponent p [54]. Introducing equations (2.2.9a - 2.2.9e) into equation (2.2.8), one gets the following equation for the development of the maximum shear stress:

$$\frac{\partial}{\partial t}\int_0^\infty \frac{\tau_{\max} f F^p}{A_1}\, dy + \frac{\partial}{\partial x}\int_0^\infty U\tau_{\max}\frac{fF^p}{A_1}\, dy - \int_0^\infty \tau_{\max} f\frac{\partial U}{\partial y} F dy + \int_0^\infty \tau_{\max}^{3/2}\frac{f^{3/2}}{L_d}\, dy = 0 \qquad [2.2.10]$$

or

$$\frac{\partial}{\partial t}(\tau_{\max} I_t) + \frac{\partial}{\partial x}(\tau_{\max} I_c) - (\tau_{\max} I_p) + (\tau_{\max}^{3/2} I_d) = 0 \qquad [2.2.11]$$

where:

$$I_t = \int_0^\infty \frac{fF^p}{A_1}\, dy \qquad [2.2.12]$$

$$I_c = \int_0^\infty U \frac{fF^p}{A_1}\, dy \qquad [2.2.13]$$

$$I_p = \int_0^\infty \frac{\partial U}{\partial y} fF dy \qquad [2.2.14]$$

$$I_d = \int_0^\infty \frac{f^{3/2}}{L_d}\, dy \qquad [2.2.15]$$

The four integrals are functions of the time (t) and space (x) variables only. The factor F, that was defined earlier, represents increased production due to normal stresses. Unlike other models, the contribution of the normal stresses in the production of turbulence is included in the present model. The reason for this is the experimental observation that the production due to normal stresses can be as high as 50 percent of the production due to shear stresses [55]. The modeling of this term will be discussed shortly.

The function f gives the non-dimensionalized stress profile for each station. The calculation of this term is performed by dividing the values of the shear stress at the centroid of each element by the maximum value of the profile before the evaluation of the integrals (2.2.12 - 2.2.15).

In the case of a steady flow, the time derivative is zero and eqn. (2.2.11) becomes an O.D.E. The integration of the equation requires the specification of the maximum shear stress as an initial condition at the begining of the computational domain. This condition can be either given from experimental results or using an algebraic model. The application of the model also requires an initial distribution for the velocity and stress fields. This information can be supplied by initially solving for the flow variables using a simple algebraic model. More details concerning the numerical implementation of the model will be given in the next chapter (Chapter 3). In the case of an unsteady flow, eqn. (2.2.11) becomes a P.D.E. Both initial and boundary conditions are required for the integration of the equation. An initial distribution of the maximum shear stress as a function of the spatial coordinate (x) at time $t=0$, as well as the value of τ_{max} at $x = x_0$ as a function of time, are required. The first condition can be obtained by a steady solution at $t=0$. The second condition can be given either by experimental results or by a simple algebraic model. Concluding this section, the reader should keep in mind that compared to other methods, no assumptions concerning the path of the maximum shear stress have been included in the model, and both convective terms have been kept. The latter is another advantage of the integral formulation. The elimination of the assumption concerning the path of the maximum shear stress becomes more important in the case of unsteady flows.

2.3 *The variation of* α_1

In the previous section, it was shown that the T.K.E. equation can be transformed into an approximate equation governing the evolution of τ_{max} by introducing into the equation the ratio of the shear stress to the T.K.E. It was also noted that this ratio is assumed constant, independent of the flow conditions. This is not exact. It is observed experimentally that the ratio of the shear stress to the T.K.E. is reduced in the presence of adverse pressure gradient [53]. This is probably due to the change in the structure of the turbulent boundary layer as separation is approached. This change is taken into account here through an empirical relationship based on experimental observations [54]. The ratio is taken to be equal to $A_1 F^{-p}$, where F is the factor that accounts for the increased production due to normal stresses, and A_1 is a constant that varies between 0.25 and 0.3. In the present work, the constant has been chosen equal to 0.25. Numerical simulations using the value of 0.3 were performed with no significant changes in the results. The value of the exponent p is equal to 1.25 according to [54].

2.4 Normal stress contribution to T.K.E production

It is usually assumed that the production due to normal stresses in the T.K.E equation can be neglected compared to that due to shear stresses. Although this can be safely assumed as approximately correct for equilibrium attached boundary layers, as separation is approached both the normal stresses and the velocity gradient in the x direction increase, resulting in increased production of T.K.E. due to the normal stresses. At the same time, the production due to shear stresses is decreasing, resulting in a ratio between the two terms of up to 0.5. This justifies an attempt at modelling this term in a rational way. The model proposed by Collins and Simpson [56] and Shiloh, Shivaprasad and Simpson [54] is used here. This model is based on the assumption that the stresses can be related to the T.K.E., at the location where the shear stress becomes maximum, in the following way:

$$\overline{u^2} - \overline{v^2} = 2C_1 K / F^{.25} \qquad [2.4.16]$$

Using the definition of F and the ratio of the shear stress to the T.K.E ($= A_1 F^{-1.25} = a_1$) one can find the following expression for F:

$$F = \frac{1}{\left(1 + \frac{C_1}{A_1} \frac{\frac{\partial U}{\partial x}}{\frac{\partial U}{\partial y}}\right)} \qquad [2.4.17]$$

where the values of A_1 and C_1 are calibrated using experimental data. An average value of 2.79 is reported in [54] for the ratio of the two constants.

2.5 Calculation of the dissipation term

In section 2.2, the following expression was introduced for the calculation of the dissipation term:

$$\bar{\varepsilon} = \frac{\tau^{1.5}}{L_d} \qquad [2.5.18]$$

In the present section, the calculation of dissipation is discussed in more detail. Equation (2.5.18) is derived from dimensional considerations. This equation also requires the specification of a dissipation length (L_d). The dissipation length is taken to be equal to the mixing length in the law of the wall region. This is consistent with the observation that the production and the dissipation are the two dominant terms in this region of the flow and they almost cancel each other, being closely equal and opposite in magnitude. The problem with equation (2.5.18) is that it predicts zero dissipation on the wall. This result is incorrect as can be verified from both theoretical and Direct Numerical Simulation results (DNS) [57]. The asymptotic value on the wall is equal to:

$$\varepsilon^+ = 2\,\frac{K^+}{(y^+)^2} \qquad [2.5.19]$$

Despite this deficiency, the model equation predicts a maximum at about the same location where DNS solutions predict the existence of a plateau. The failure of the model in the viscous sublayer is expected, since the dimensional arguments used for deriving this expression are not valid there. Modification of the situation can be accomplished in a number of ways. The simplest approach and the one followed here is to assume that the dissipation between the wall and the location where the model predicts a maximum value is constant and equal to the maximum value. Although the value on the wall is then high, this approach neglects a smaller portion of the true dissipation when the latter is integrated across the boundary layer, compared to the unmodified version. An alternate approach would make use of the asymptotic value of the dissipation near the wall. Assuming that this relationship is valid for a few y^+ units away from the wall, and using the ratio of the shear stress to the T.K.E. along with the predicted value of the Reynolds stress in the near wall region, one can get an approximate curve for the viscous sublayer region. This curve along with the predictions of eqn. (2.5.18) are presented in Fig. (1).

The dissipation length in the near wall region has to be modified using the van Driest damping function. From the previous figure, it becomes obvious that a different damping constant is required for the results to be consistent with the values predicted from DNS. Wolfstein [58] has also adopted different values for the mixing and dissipation lengths in his near wall damping functions. His approach uses the Reynolds number of turbulence instead of y^+ as a measure of the wall influence on the turbulence. A value of A^+ between 12 and 14 seems to give good agreement. The value of 14 has been used in the present study. The dissipation length for the outer region is assumed proportional to the boundary layer just as for the mixing length. The constant of proportionality has been chosen equal to 0.082, a value which is lower than the usually used value of 0.09, but in good agreement with the experimentally observed values of Simpson, Strickland and Barr [55], for flow developing in the presence of strong pressure gradients. Here, it was found useful to have the dissipation length in the outer region mimic the behaviour of the mixing length in that region as governed by the auxiliary equation. In equilibrium regions, we take the mixing length in the outer region to be $l_m = C\delta$ with $C = 0.09$ and and the dissipation length to be $L_d = C_d\delta$ with $C_d = 0.082$. As C is reduced by the auxiliary equation in strong adverse pressure gradients, it is assumed that $C_d = (0.082/0.09)C$. This point will be better understood in the section that follows, where, the mixing length distribution across the boundary layer is introduced.

2.6 Mixing length distribution

In the previous sections, the governing equation for the maximum shear stress was developed. This equation is not predicting the shear stress across the boundary layer. It only provides a scaling factor for the shear stress profile at each x location. To complete the calculation of the shear stress, a formula that relates the shear stress to the other mean flow variables, and its maximum value must be proposed. In this work, a mixing length approach has been chosen to accomplish this task. This new mixing length formula is based on a rigorous distribution of the stress profile.

The simple mixing length formulation has been used extensively in the calculation of attached flows, even in cases of strong adverse pressure gradients [4]. The mixing length is assumed to be proportional to the distance from the wall for the near wall region, while it becomes proportional to the boundary layer thickness in the outer region. This formulation does not yield satisfactory results when applied to cases with strong adverse pressure gradients. This is because the near wall formulation assumes a constant distribution of shear stress. The stress is given as the product of the mixing length, κy, the velocity scale, $\kappa y \partial U/\partial y$, and the velocity gradient. In an attempt to improve this deficiency, Johnson and King [20] proposed a near wall model that uses the same length scale but introduces the square root of the maximum shear stress as the characteristic velocity scale in their eddy viscosity formulation. Johnson and Coakley [59] have proposed another algebraic velocity scale which is derived based on the assumption of a linear stress distribution between the wall and the maximum value of the shear stress.

In the present work, a new mixing length formulation is proposed based on a rigorous distribution of the stress profile. The derivation is based on the experimental observation that the law of the wall remains valid even in the presence of strong adverse pressure gradients [60,61]. While this remains a subject of debate and study [62,63], the preponderance of evidence supports the validity of the law of the wall. Coles [64] has expressed the momentum equation for steady, two-dimensional flow in nondimensional terms as:

$$\frac{\tau}{\tau_w} = 1 \; + \; y^+p^+ \; + \; \frac{\nu}{u_\tau^2}\frac{du_\tau}{dx}\int_0^{y^+} h^2(y^+)dy^+ \tag{2.6.20}$$

$$y^+ = y\frac{u_\tau}{\nu} \tag{2.6.21}$$

$$p^+ = \frac{\nu}{\rho u_\tau^3}\frac{dP}{dx} \tag{2.6.22}$$

$$h(y^+) = \frac{U}{u_\tau} \quad , \quad u_\tau = \sqrt{\frac{\tau_w}{\rho}} \tag{2.6.23}$$

where $\tau = \tau_l + \tau_t$. In a similar way, for unsteady, two-dimensional flow and neglecting the normal stress term, the momentum equation can be written in nondimensional terms in the following way:

$$\frac{\tau}{\tau_w} = 1 \; + \; y^+p^+ \; + \; \frac{\nu}{u_\tau^2}\frac{du_\tau}{dx}\int_0^{y^+} h^2(y^+)dy^+ + \frac{\nu}{u_\tau^3}\frac{\partial u_\tau}{\partial t}y^+h(y^+) \tag{2.6.24}$$

The function $h(\bullet)$ is a function of y^+ only and it can be calculated from the near wall velocity profile of the universal law of the wall. An extended mixing length formula for the inner region consistent with strong adverse pressure gradients can be derived, if we require that:

$$l_m^2\left(\frac{\partial U}{\partial y}\right)^2 = \tau \qquad [2.6.25]$$

where τ is given by eqn. (2.6.24), rather than the usual assumption $\tau = \tau_w$ or some *ad hoc* assumed variation. The expression for the mixing length becomes:

$$l_{m,In} = \kappa y D\left(1 \; + \; y^+p^+ \; + \; \frac{\nu}{u_\tau^2}\frac{\partial u_\tau}{\partial x}\int_0^{y^+} h^2(y^+)dy^+ + \frac{\nu}{u_\tau^3}\frac{\partial u_\tau}{\partial t}y^+h(y^+)\right)^{1/2} \qquad [2.6.26]$$

where D is the van Driest damping function that modifies the mixing length in the buffer zone and the viscous sublayer.

The importance of this extended formulation becomes obvious when one considers the derivative of the velocity profile that results from the application of the usual mixing length model. Starting from the expression for the total stress in the near wall region:

$$(1 + \frac{l_m^2}{\nu}\frac{\partial U}{\partial y})\frac{dU^+}{dy^+} = \frac{\tau}{\tau_w} \qquad [2.6.27]$$

where the right hand side is given by equation (2.6.24) and solving for the non-dimensional velocity gradient, one obtains the following expression:

$$\frac{dU^+}{dy^+} = \frac{2(1 + p^+y^+ + \frac{\nu}{u_\tau^{\,2}}\frac{\partial u_\tau}{\partial x}\int h^2 dy^+ \frac{\nu}{u_\tau^{\,3}}\frac{\partial u_\tau}{\partial t}y^+ h)}{1 + (1 + 4\kappa^2 y^{+2} D^2)^{1/2}} \qquad [2.6.28]$$

In the limit of $y^+ >> 1$, the slope can be expressed as follows:

$$\frac{dU^+}{dy^+} \rightarrow \frac{1}{\kappa y^+} + \frac{p^+}{\kappa} + \frac{\nu}{\kappa u_\tau^{\,2}}\left(\frac{\partial u_\tau}{\partial x}\frac{\int h^2 dy^+}{y^+} + \frac{1}{u_\tau}\frac{\partial u_\tau}{\partial t}h\right) \qquad [2.6.29]$$

and thus it fails to reproduce the law of the wall, proving the need for the complete formulation in eqn. (2.6.26). This completes the development of the near wall mixing length formula.

The expression for the mixing length in the outer region is $l_{m,o} = C\delta$, where δ is the boundary layer thickness and C is a constant with respect to y. Rather than adopting the equilibrium value of 0.09, the value of C at each station and time step is determined here so that the maximum value of the shear stress predicted from eqn. (2.6.25) is equal to the one predicted from the auxiliary equation, eqn. (2.2.10), at the same location.

A hyperbolic tangent function is used for blending the inner and outer mixing length region expressions, in the following way:

$$l_m = l_{m,o}\left(\tanh\left(\frac{l_{m,in}^n}{l_{m,o}^n}\right)\right)^{1/n} \qquad [2.6.30]$$

A smooth distribution is required for two reasons. First, it produces a smooth shear stress profile, which is important in locating the maximum value using a numerical procedure like the Newton-Raphson method. Second, it makes l_m functionally dependent on C across most of the boundary layer. This is critical in matching the maximum shear stress through the variation of this constant. The value of the exponent (n) used in the present work is chosen equal to 1. As the exponent increases, the blending becomes sharper and approaches the distribution:

$$\begin{aligned} l_m &= \kappa y \qquad (inner \quad region) \\ l_m &= C\delta \qquad (outer \quad region) \end{aligned} \tag{2.6.31}$$

which has a discontinuous derivative. Such a discontinuous distribution is not suited for a numerical estimation of the location of the maximum shear stress. Higher values of the exponent (n) were used but they did not work well, especially in the region of attached flow with low pressure gradient. This can be explained taking into account the proximity of the location of the maximum shear stress to the wall, the flatness of the shear profile in the same region, and the small influence that the variation of C has on the value of the mixing length in the inner region for the sharper blending. For the regions of the flow with low or zero pressure gradient, the stress profile in the near wall region is almost flat. The reader should recall that for such flow situations $\tau \simeq \tau_w$ near the wall. Under these conditions, the influence of the value of C on the value of the mixing length in the near wall region diminishes, as the wall is approached and the value of the exponent increases. As a result, the numerical method often oscillates predicting unreasonably high values for C, or completely fails to converge.

Chapter 3

Chapter 3

3.1 Numerical implementation of the new model

In the previous chapter, the theoretical development of the new model was presented in detail. The present chapter focuses on the numerical implementation of the new model. The description of the numerical method used for solving the equations of motion is presented in Appendix A.

3.2 The governing equations

In order for the reader to better understand the solution strategy that is followed in the present work, it was decided that a short presentation of the system of governing equations and their interdependence is required.

The present model has been incorporated in a Finite Element Method (F.E.M) code that solves the incompressible, steady and unsteady, two-dimensional boundary layer equations in the direct mode, that is the free-stream pressure gradient or free-stream velocity needs to be specified [65]. The use of a boundary layer code does not imply any restriction concerning the implementation of the new model into a full Navier-Stokes code. The use of the F.E.M for the solution of the boundary layer equations is also unrelated to the implementation of the model. That means that the model can be easily implemented into a Finite Difference or Finite Volume type of solver if that is preferable. As it will be shown in a later section, this flexibility of implementation is accomplished primarily through the way that the equations of motion are coupled to the auxiliary P.D.E (or O.D.E for steady cases) that governs the development of the maximum shear stress.

Continuity equation

$$\frac{\partial U}{\partial x} + \frac{\partial V}{\partial y} = 0 \qquad [3.2.1]$$

x-Momentum equation

$$\frac{\partial U}{\partial t} + U\frac{\partial U}{\partial x} + V\frac{\partial V}{\partial y} = -\frac{1}{\rho}\frac{dP}{dx} + \frac{\partial}{\partial y}\left((\nu \ + \ l_m{}^2\left(\frac{\partial U}{\partial y}\right))\frac{\partial U}{\partial y}\right) \qquad [3.2.2]$$

y-Momentum equation

$$\frac{\partial P}{\partial y} \approx 0 \qquad [3.2.3]$$

P.D.E governing maximum shear stress evolution

$$\frac{\partial}{\partial t}(\tau_{\max} I_t) + \frac{\partial}{\partial x}(\tau_{\max} I_c) - (\tau_{\max} I_p) + (\tau_{\max}^{3/2} I_d) = 0 \qquad [3.2.4]$$

Relationship between outer mixing length constant (C) and maximum shear stress

$$l_m^2(C)\left(\frac{\partial U}{\partial y}\right)\Big]_{\max} = \tau_{\max} \qquad [3.2.5]$$

Mixing length distribution

$$l_{m,In} = \kappa y D\left(= 1 \ + \ y^+ p^+ \ + \ \frac{\nu}{u_\tau^2}\frac{du_\tau}{dx}\int_0^{y^+} h^2(y^+)dy^+ + \frac{\nu}{u_\tau^3}\frac{\partial u_\tau}{\partial t} y^+ h(y^+)\right)^{1/2}$$

$$l_{m,o} = C\delta \qquad [3.2.6]$$

$$l_m = l_{m,o}\left(\tanh\left(\frac{l_{m,In}}{l_{m,o}}\right)\right)$$

As the reader can see, the system of equations is nonlinear, and an iterative scheme is needed for its solution. It should also be clear now that the numerical method used for solving for the equations of motion, and the one used for the equation governing the evolution of the maximum shear stress do not have to be the same. The two sets of equations are related only through the mixing length, which is an algebraic relationship. Once a distribution of mixing length is known, the equations of motion can be solved using any appropriate numerical method.

The solution strategy used can be seen in Figs. 2, 3. A description of each step and the details of the implementation follow:

Step 1

An initial guess for the velocity and stress field is needed in order for the integrals in eqns. (2.2.12 - 2.2.15) to be evaluated. For both steady and unsteady flows, such a guess can be obtained using a simple algebraic model in a numerical solution procedure. In the present work, the simple algebraic mixing length model:

$$\begin{aligned} l_{m,in} &= D\kappa y \\ l_{m,o} &= 0.09\delta \end{aligned} \qquad [3.2.7]$$

is used, where D is the van Driest damping function which is defined as $(1 - \exp(-y^+/A^+))^2$. The value of A^+ depends on the constants κ and C of the law of the wall. The value of $A^+ = 24.5$ is used here. This corresponds to κ = 0.41 and C =5.0. The solution that we obtain is the answer that the algebraic model predicts for the flow. It is also the initial guess for the new model. The velocity profile at the inlet plane can be specified either by an analytic solution or experimental data. The freestream velocity, or pressure gradient, must also be given for the solution of the boundary layer equations.

Step 2

Once a " trial " solution is known, the integrals in eqns. (2.2.12 - 2.2.15) are evaluated for each location (x) and time (t). Two methods of numerical integration were used: a) the trapezoidal rule, and b) integration of the spline that interpolates the pointwise values. Both methods gave similar results, thus it was decided that the trapezoidal rule is adequate. This result can be explained as follows. The integrands are varying faster in the near wall region. This is also the region where there is a higher concentration of mesh points, and this high resolution of the integrating function reduces the numerical error.

Step 3

For unsteady flows, the P.D.E. is integrated in time (t) and space (x) yielding a new distribution of τ_{max}. For steady flows, one only needs to integrate in space. At this point, the convergence of the method is checked. The following norm is used:

$$\left(\frac{\sum_i (\tau^n_{\max}(x_i) - \tau^{n-1}_{\max}(x_i))^2}{\sum_i (\tau^n_{\max}(x_i))^2} \right)^{1/2} \le \varepsilon_1 \qquad [3.2.8]$$

If the norm is smaller than a specified upper limit (ε_1), then convergence has been obtained and the postprocessing can start. If not, the next step is executed.

In order to avoid big steps in the iterative solution for $\tau_{\max}$, underelaxation is applied to the new values predicted from the auxilliary P.D.E (O.D.E). This means that the new distribution of the maximum shear stress is given as a linear combination of the current and previous iteration, i.e.:

$$\tau^{(new)}_{\max} = a\tau^{(n)}_{\max} + \tau^{(n-1)}_{\max}(1 - a) \qquad [3.2.9]$$

Here, we make reference to the iterations resolving the nonlinearity of the system and not the time iterations. Because of the importance of the auxiliary equation, presentation of the integration method used follows in the next section.

Figure 4 shows schematically the location of the $\tau_{\max}$ "nodes" in a numerical grid composed of bilinear elements. Although the integrals are evaluated at the centroid of the element, the maximum shear stress is not really assigned to "nodes". It is associated with each column of elements. Within each element, the stress is calculated at the quadrature points during the integration of the momentum equations. These values are then interpolated at the centroid of the element. The requirement that the maximum stress of each column of elements coincide with the one predicted from the auxiliary equation gives a new value of C. This is described in the next step of the algorithm.

Step 4

This step involves the calculation of a new value for the constant (C) of the outer mixing length. This requires: a) calculating the maximum shear stress for each stress profile, b) finding the value of C that satisfies eqn. (3.2.5), i.e., finding the value of C that makes the maximum value of each shear stress profile equal to the one predicted from the auxilliary P.D.E (O.D.E) for the same location. For the first part, the method initially searches the solution of the differential equations of motion for the pointwise maximum value at the centroid of each element. Once the location and the value are found, a cubic polynomial is used to interpolate for the stress profile around the point of interest. At the location of the maximum, the derivative of the interpolant should be equal to zero. The derivative is a quadratic polynomial, the roots of which can be found analytically. Once the location of the maximum is found, the interpolant is used for calculating the value of the maximum stress. This value must be the same, within some prescribed tolerance, to the value predicted from the auxilliary P.D.E. (O.D.E.) at the same location. This is accomplished by adjusting the value of C in eqn. (3.2.5). The value of τ_{max} on the right hand side of the equation is the one predicted from the auxilliary equation. This is a root finding problem, and a number of well-known numerical methods can be used [66]. The one used here is the

Newton-Raphson method. The reason for choosing this method is its quadratic convergence. Since the root finding problem is repeated a lot, a fast method had to be implemented. For each x location, a first guess is required. The converged solution for the previous station is used as the initial guess. This choice has been proven to be very robust. For the upstream location, the value predicted from the algebraic model can be used as the first guess. Applying the method to eqn. (3.2.5), leads to the following expression for the value of C:

$$C_{i+1} = c_i\left(1 - \frac{\tau_m(C_i) - \tau_{\max}}{2\tau_m(C_i)\left(1 - 2\dfrac{l_{m,in}}{l_{m,o}}\dfrac{1}{\sinh\left(\dfrac{2l_{m,in}}{l_{m,o}}\right)}\right)}\right) \qquad [3.2.10]$$

Here, $\tau_m(C_i)$ is the maximum shear stress of the profile, and $\tau_{\max}$ is the value predicted from the auxiliary equation for the same location.

Usually, two to three iterations are needed for convergence. The following criterion for convergence is used:

$$\left| \frac{\tau_{\max} - \tau_m(C_i)}{\tau_{\max}} \right| \leq 5 \times 10^{-3} \qquad [3.2.11]$$

The method has been proven very robust for almost all flow situations. Some convergence difficulties have been observed in the case of strong favorable pressure gradients, which force the location of the maximum shear stress closer to the wall. For those cases, the method is not used, and the C value is automatically set equal to 0.09. The explanation for these problems can be found in the inability of the constant C to influence the value of the mixing length in the near wall region. Extensive numerical experimentation has indicated that when the value of the mixing length at the location of the maximum shear stress is higher than 0.96 κ y, the method has no convergence difficulties.

A constraint has also be placed on the amount that C can change from one iteration to the next. The allowable change is $\mp$ 5 % of the previous value. This constraint prohibits any sudden changes that may occur, but at the same time it prohibits quadratic convergence. In practice, the constraint was rarely active.

Step 5

Once a new distribution of C has been obtained, the equations of motion can be solved again, producing new velocity and stress distributions. During this part of the solution strategy, the new model behaves simply as an algebraic model with a modified outer constant. Once a new solution has been obtained, the solution is repeated starting from Step 2.

For the steady flows tested in this work, six to eight iterations were required for convergence to a tolerance of 1×10^{-3}. For the unsteady flow, two iterations per time step were adequate.

Initially, a different approach was tested. In that approach, the domain was divided into two regions. For the first region, the algebraic model, eqn. (3.2.7), was used. The equations of motion were integrated only once. The second region was starting at the end of the first one, and the starting point of this region was chosen in the flow region where turbulence was assumed to be in equilibrium.

This implies that the favorable and zero pressure gradient regions of the flow were solved using the simple algebraic model, while the adverse pressure gradient region was solved using the new model. Although it seemed a reasonable approach at first, it had a major problem. The slope of the maximum shear stress at the switching point was discontinuous. The problem was mainly due to the discontinuous distribution of the mixing length in the inner region. While the simple algebraic model uses $\kappa y D$ as the value of the mixing length, the new model uses the expression given by eqn. (2.6.26). The problem was more intense for unsteady flow. Thus, the approach was abandoned in favor of the one described earlier.

3.3 Integration of the auxiliary equation

The form of the auxiliary equation for the steady and unsteady flows was given in the previous chapter. Here, the numerical integration of the equation will be presented. Because of the difference in the classification of the equation for the steady and unsteady case, the numerical method used for each of them will be presented separately.

(A) Steady flow

For steady flow, eqn. 2.2.11 takes the following form:

$$\frac{d\tau_{\max}}{dx} I_c + \tau_{\max}\left(\frac{dI_c}{dx} - I_p\right) + \tau_{\max}^{3/2} I_d = 0 \qquad [3.3.12]$$

This is a nonlinear ordinary differential equation but the nonlinearity of the equation can be removed using the following transformation:

$$T = \tau_{\max}^{-1/2} \qquad [3.3.13]$$

This is the same transformation that Johnson and King [20] used for transforming their auxiliary equation. Inserting eqn. (3.3.13) into (3.3.12), one obtains:

$$\frac{dT}{dx} = T\frac{1}{2I_c}\left(\frac{dI_c}{dx} - I_p\right) + \frac{I_d}{2I_c} \qquad [3.3.14]$$

or

$$\frac{dT}{dx} = AT + B \qquad [3.3.15]$$

where:

$$A = \frac{1}{2I_c}\left(\frac{dI_c}{dx} - I_p\right)$$
$$B = \frac{I_d}{2I_c} \qquad [3.3.16]$$

The numerical integration of this equation is performed using a fourth-order Runge - Kutta method. The integration scheme can be written as follows:

$$
\begin{aligned}
k_1 &= (x_i - x_{i-1})(A_{i-1}T_{i-1} + B_{i-1}) \\
k_2 &= (x_i - x_{i-1})((T_{i-1} + \frac{1}{2}k_1)A_{i-\frac{1}{2}} + B_{i-\frac{1}{2}}) \\
k_3 &= (x_i - x_{i-1})((T_{i-1} + \frac{1}{2}k_2)A_{i-\frac{1}{2}} + B_{i-\frac{1}{2}}) \\
k_4 &= (x_i - x_{i-1})((T_{i-1} + k_3)A_i + B_i) \\
T_i &= T_{i-1} + \frac{1}{6}(k_1 + 2k_2 + 2k_3 + k_4)
\end{aligned}
\tag{3.3.17}
$$

The x_i corresponds to the centroid of the elements, which is also the location where the maximum shear stress and the integrals are stored. Since the integration method requires the values of the integrals at the faces of elements, a cubic spline is used to interpolate for those locations. The presence of the spatial derivative of I_c requires some attention. Because the presence of the derivative in the numerical scheme can amplify any noise present in the integrals, it was decided that a least square cubic spline had to be used. The choice of the cubic spline that most faithfully follows the pointwise distribution of values was based on the observation that the pointwise values were, in general, very smooth. The purpose of the least squares approach was to eliminate any localized discrepancies due to the numerical evaluation of the integrals. An initial value (T_0) is required for the integration of the ordinary differential equation. This value is obtained from the use of the simple algebraic model. Although, this value can be the τ_{max} that corresponds to the initial profile, a later value had to be used. This was done in order for the solution to adjust to any mismatch of the initial conditions for the velocity profiles. In general, the use of the value that corresponds to the fifth or sixth station was found satisfactory for the results presented here.

(A) Unsteady flow

For unsteady flows, eqn. (2.2.11) is a partial differential equation. Using the following transformation:

$$Q = I_t \tau_{\max} \tag{3.3.18}$$

the P.D.E. can be written as follows:

$$\frac{\partial Q}{\partial t} + \frac{\partial (WQ)}{\partial x} - AQ + BQ^{3/2} = 0 \tag{3.3.19}$$

where:

$$A = \frac{I_p}{I_t}$$
$$B = \frac{I_d}{I_t^{3/2}} \tag{3.3.20}$$
$$W = \frac{I_c}{I_t}$$

Equation (3.3.19) has the form of a wave equation, and it must be integrated using appropriate methods. The coefficient W represents the speed of propagation of the wave. The equation has been integrated using the Crank-Nicolson method [5].

Crank-Nickolson (Trapezoidal) scheme

Equation (3.3.19) can be rewritten in the following way:

$$Q_t + R = 0$$
$$R = (WQ)_x - AQ + BQ^{3/2} \qquad [3.3.21]$$

Applying Crank-Nicolson time differencing in this equation, one obtains:

$$Q_i^{n+1} = Q_i^n + \frac{\Delta t}{2}(Q_t^{n+1} + Q_t^n)_i + O(\Delta t^3) \qquad [3.3.22]$$

and replacing Q_t with R, the discrete equation reads:

$$Q_i^{n+1} = Q_i^n - \frac{\Delta t}{2}\left(\frac{(WQ)_{i+1}^{n+1} - (WQ)_{i-1}^{n+1}}{2\Delta x} + \frac{(WQ)_{i+1}^{n} - (WQ)_{i-1}^{n}}{2\Delta x}\right) + \qquad [3.3.23]$$
$$\frac{\Delta t}{2}((AQ)_i^{n+1} + (AQ)_i n) - \frac{\Delta t}{2}((BQ^{3/2})_i^{n+1} + (BQ^{3/2})_i^n)$$

This system of equations is nonlinear. Both the wave speed, the coefficients A and B, as well as the value of Q^{n+1} that appears in the nonhomogeneous part of the equation are not known *a priori*. The equation needs to be linearized. At present, an iterative approach is used. The linearization of the coefficients A,B,W is accomplished by using the most recent values calculated during the iterative solution for the global system of equations (see Step 2). These coefficients will be denoted by $\overline{n+1}$, and are kept constant during the iterative solution of the system of equations eqn. (3.3.23). The term Q^{n+1} in the nonhomogeneous part of the equation is linearized by replacing it with the most recent value predicted from eqn. (3.3.23) during the iterative solution. Denoting this term as $Q^{\overline{\overline{n+1}}}$, the scheme can finally be written as:

$$Q_i^{n+1} = Q_i^n - \frac{\Delta t}{2}\left(\frac{W_{i+1}^{\overline{n+1}}Q_{i+1}^{n+1} - W_{i-1}^{\overline{n+1}}Q_{i-1}^{n+1}}{2\Delta x} + \frac{(WQ)_{i+1}^n - (WQ)_{i-1}^n}{2\Delta x} \right) + \qquad [3.3.24]$$
$$\frac{\Delta t}{2}\,(A_i^{\overline{n+1}}Q_i^{\overline{\overline{n+1}}} + (AQ)_i^n) - \frac{\Delta t}{2}\,(B_i^{\overline{n+1}}(Q_i^{\overline{\overline{n+1}}})^{3/2} + (BQ^{3/2})_i^n)$$

All the variables that have an (n) as the time index are evaluated at the previous time step. The Thomas algorithm is used during each iteration for the solution of the tridiagonal system of equations. Two to three iterations are usually needed for convergence of the method.

Due to the central differencing in space, special treatment for the last node is required. An equation for this node can be obtained using either an implicit or an explicit one-sided scheme. The implicit scheme is preferred due to the lack of any limitation for the time step. The discrete equation reads:

$$(1 + \frac{\Delta t}{\Delta x}\,W_j^{n+1})Q_j^{n+1} - \frac{\Delta t}{\Delta x}\,W_{j-1}^{n+1}Q_{j-1}^{n+1} = (1 + A_j^n\Delta t)Q_j^n - B_j^n(Q^{3/2})_j^n\Delta t \quad [3.3.25]$$

This scheme is second order accurate in both space and time. Linear stability analysis of the Crank-Nickolson scheme applied to the homogeneous wave equation with constant coefficients indicates that the scheme is unconditionally stable. This analysis does not include the effect of the nonhomogeneous terms and the variable wave speed on the stability. Numerical experimentation with different values of Δt for the auxiliary equation indicated no tendency for instability.

3.4 Boundary and Initial conditions

The integration of the auxiliary equation require both boundary and initial conditions for τ_{max}. The boundary condition at the upstream location, for each time step, is given by the application of the mixing length model. In order to avoid any discontinuities in the τ_{max} distribution, the mixing length distribution given by eqn. (2.6.26) is used for the inner region, while the mixing length for the outer region is taken equal to 0.09 δ. The starting point is chosen in the region where the turbulence is considered to be in equilibrium at all times. For starting the calculation, initial conditions are required. For the test case presented in the next chapter, the initial conditions were obtained through a steady state simulation at time $t=0$. Since this is a periodic flow, after several periods, the influence of the initial conditions disappears. The phase of the cycle with the maximum freestream velocity was chosen as the starting point of the calculation.

This concludes the presentation of the numerical implementation of the model. In the next chapter, the predictive capabilities of the new model will be presented. Both steady and unsteady results are considered and discussed.

Chapter 4

Chapter 4

4.1 Test cases and performance of the model

The predictive ability of the model has been evaluated using as test cases four well documented incompressible, turbulent flows. These flows are: (a) turbulent flow over a flat plate, (b) Samuel and Joubert steady, strong adverse pressure gradient flow [67], (c) Simpson, Chew and Shivaprasad steady, strong adverse pressure gradient flow with separation [68], and (d) Simpson, Chew, and Shivaprasad unsteady, strong adverse pressure gradient flow with separation [69].

The first case is standard test for all turbulence models. This is the simplest turbulent flow, it is well documented and all proposed models must be able to predict it correctly. The next two steady flow cases have been used as test cases for the 1980-1981 AFOSR-HTTM-Stanford conference on complex turbulent flows [31]. This allows the comparison of the performance of the new model with the performance of a number of models used at the conference. Finally, the unsteady flow of Simpson *et al* was chosen for two main reasons: a) it is a logical extension to the steady experiment (case c) and b) the reduced frequency of the experiment makes an excellent representation of flows of engineering interest.

4.2 Turbulent flow over a flat plate.

Consider first the flow over a flat plate with zero pressure gradient. This case might be a trivial test. Nevertheless, every turbulence model must be able to, at least, predict correctly this flow. This test case is also used as a way of evaluating the influence of the dissipation length constant on the results. As was mentioned earlier, the constant for the dissipation length in the outer region, was chosen equal to 0.082 instead of the usual value of 0.09, based on experimental observations for adverse pressure gradient flows.

The inlet profile was created by using the log law for the inner region and the Coles law of the wake for the outer region. The Reynolds number for the flow, at the inlet, based on the displacement thickness was equal to 5000. This value seems to be an adequate lower limit for obtaining fully developed turbulent flow with the usual constants for the law of the wall. The skin friction coefficient calculated using both the new model and the simple algebraic model are presented in Fig. 5. The comparison shows a very small effect on the skin friction, with the value predicted from the new model overlapping with the predictions of the simple model for most of the domain. Both results are also in excellent agreement with the skin friction coefficient calculated from the following expression:

$$\left(\frac{2}{c_f}\right)^{1/2} = \frac{1}{\kappa}\ln\left(Re_\delta\left(\frac{c_f}{2}\right)^{1/2}\right) + C - B \qquad [4.2.1]$$

where B = -2.5, κ = 0.41 and C = 5.0 [70]. This expression can be derived from the log law of the wall [4]. The value of δ used in the equation is obtained from the use of an integral method [4]. The one seventh law for the velocity profile is used for its derivation. This leads to the following ratios for the displacement (δ^*) and momentum (θ) thicknesses that are compared in Figs. 6 and 7:

$$\frac{\delta^*}{\delta} = \frac{1}{8} \quad , \quad \frac{\theta}{\delta} = \frac{7}{72} \qquad [4.2.2]$$

Both the new and the simple algebraic models predict identical curves for the displacement and momentum thicknesses. Those predictions are in very good agreement with the expressions given by Eq. (4.2.2).

Figure 8 presents the predictions concerning the velocity profile plotted on semilogarithmic scale. The agreement with the law of the wall is excellent. These results indicate that the auxiliary equation is behaving properly for the case of zero pressure gradient, which assures that no major violation of the physics in favor of the adverse pressure gradient flows has been committed. It is also indicating that the dissipation is rather insensitive with respect to the outer layer constant. This observation is important, since, as was mentioned earlier, the value used here agrees mainly with results obtained for adverse pressure gradient flows.

4.3 Samuel and Joubert steady adverse pressure gradient flow

The case considered here involves a flow with increasingly adverse pressure gradient. Figure 9, which is taken from [67], presents the geometry of the tunnel, the pressure distribution along the wall and its pressure gradients. The calculation starts at station 1 of the experiment which is located at $x = 0.855$ meters. The U-component of the velocity was taken from the experimental results. A least square, cubic spline approach [71] was used for smoothing the experimental data. The V-component of the velocity was set to zero. The solution of the boundary layer equations also requires the specification of the free-stream velocity or pressure gradient and the experimentally obtained pressure gradient was used. The same least square subroutine that was applied to the velocity profile was also used for the pressure gradient. The reader should recall that the pressure gradient enters directly into the mixing length expression (see eqn. 2.6.26) making the use of a smooth distribution rather important. The domain ends at $x = 3.4$ meters, which is the end of the experiment. The results that are presented in this section have been obtained using 200 stations in the x-direction and 74 elements in the y-direction. The nodes in the x-direction are equally spaced, while a geometric progression is used for the nodes in the y-direction. Numerical experimentation indicated that the location of the first node off the wall was very important in accurately predicting the flow, especially the skin friction coefficient. Values of y^+ between 1 and 3 seem to be adequate for obtaining grid independent solutions.

Consider first the skin friction coefficient for this case. Figure 10 presents the prediction for the skin friction using the usual van Driest inner region mixing length model with $l_m = 0.09\delta$ in the outer region and the new model and the data. Three different experimental methods have been used for obtaining the skin friction. The results from both models are within the experimental uncertainty. The new model tends to predict higher values compared to the simple algebraic one, especially in the region where the adverse pressure gradient is stronger. The next two figures (Figs. 11,12) present the predictions of several models for the skin friction coefficient. The results that correspond to the calculations of Donaldson, Hanjalic, Rodi, and Murphy have been taken from the plots presented in [31]. Since no tabulated data were available, the curves were read using a digitizer. In this reference, the local shear stress is nondimensionalized using a reference velocity and not the local free-stream velocity, as the definition of the skin friction requires. Here, the results are consistent with the definition of the skin friction. The computations presented by Donaldson *et al* have been obtained using a Reynolds stress model. The turbulence length scale is determined from either an algebraic or differential equation. Hanjalic *et al* also solved the full differential transport equation for each component of the Reynolds-stress tensor and, in addition, the differential equation governing the decay of the turbulent kinetic energy. Rodi *et al* used a low Re K - ε model. Murphy *et al* have used several models. The results presented here correspond to the model of Glushko [72], with the eddy viscosity prescribed through a T.K.E. formulation. The results that correspond to the Johnson-King and K - ω models have been taken from Menter [21]. Finally, Bradshaw's results have been provided to us after request. The comparison shows that the new model performs equal well or better than the other models.

Figure 13 presents the predictions for the displacement thickness. Both models perform, well with the new model giving values closer to the data. The predictions for the momentum thickness are in excellent agreement with the experimental data. As Fig. 14 indicates, the momentum thickness seems to be less sensitive than the displacement thickness. This is surprising if one examines the velocity profiles. The velocity profiles for the last three experimental location are given in Figs. 15 through 17. The new model performs better as the pressure gradient increases, compared to the algebraic model. Figures 18 through 21 present the performance of the different models for the last two station where experimental data exist. This comparison clearly shows that the predictions of the new model are again equally well or better compared to all the models. In order for the reader to see the superiority of the new model, the velocity profiles have to be plotted in a semilogarithmic scale. The results are shown in figures

22 through 24 for three stations, scanning the entire length of the domain. For the stations where the pressure gradient is still low (Fig. 22), both models perform equally well. As the pressure gradient is increasing, the simple algebraic model fails to reproduce the law of the wall, which the experimental results obey [67]. The difference between the predictions of the simple model and the experimental data is increasing as the pressure gradient becomes stronger. The new model, on the other hand, faithfully reproduces the experimental profiles. The predictions of the simple algebraic model and the new model for the stress profiles are presented in Figs. 25-27. As before, the predictions are almost identical for the early stations, but they differ considerably in the adverse pressure gradient region. The new model reproduces the profiles accurately, while the simple model overpredicts them. Comparison between the predictions of the new model and those of the other models for the last two stations are presented in figures 28 through 31. The comparison indicates that even for this sensitive variable, the new model performs equally well or better than any other model.

From these figures, it becomes obvious that the new model successfully reproduces the most important features of this flow. The next case has a much stronger pressure gradient, and it is a very challenging test case.

4.4 Simpson, Chew and Shivaprasad steady flow with separation

This is an airfoil-type flow in which the flow is accelerated and then decelerated until separation. The geometry of the experiment, as well as the variation of the pressure gradient are given in Fig. 32 [68]. Compared to the previous case, this flow has a much stronger adverse pressure gradient (see Fig. 33), which makes it a challenging test case. The experimental location x = 0.8051 meters was chosen as the starting point. There was some concern regarding the low Reynolds number based on the momentum thickness at this station ($Re_\theta = 1677$). Below $Re_\theta \simeq 5000$, some suggest a variation of the constants describing the law of the wall with the Reynolds number. Despite that, it was finally decided to start the calculation at this point, which is also suggested by the investigators of the case. The numerical domain is extended up to the point that the method predicts separation. This is done for two reasons: a) a boundary layer code, using the direct form, cannot solve for reverse flow, and b) the mixing length expression for the inner region is not compatible with the experimental observations for separated flows. Several runs were performed for determining an appropriate grid for this case. The node nearest to the wall was again chosen so that the y^+ value lies between 1 and 3. The results that follow have been obtained on a 200*75 grid. The grid is equally spaced in the x-direction. A geometric progression has been used for the nodes in the y-direction.

The U-velocity profile at the inlet is obtained from the experimental results, after smoothing it with the use of the least square approach that was used before. The V-velocity is set to zero. The free-stream velocity is applied as a boundary condition on the upper boundary. The pressure gradient is then calculated using the Bernoulli equation. The predictions of the two models for the skin friction are compared to the experimental results in Fig. 34. The improved performance of the new model is clear. Close to separation, the new model follows the experimental results and finally predicts separation accurately. The simple algebraic model fails to separate. Figure 35 shows the predictions of a number of different models for the skin friction. The results that correspond to the Johnson-King model have been taken from the original reference [20]. The results that correspond to the calculations of Mellor *et al* and Pletcher *et al* are from [31]. The results of Pletcher *et al* were obtained using a one-half equation model. The inner region is modeled using a mixing length approach, while the velocity and length scales for the outer region are provided through the T.K.E and a one-dimensional transport equation for the length (L). Mellor *et al* have used a five equation Reynolds stress model.

The comparison indicates that the performance of the new model is very good compared to the other models. The comparison for the displacement thickness is not as favorable, as illustrated in Fig. 36. The new model tends to follow better the rapid increase in the displacement thickness as separation is approached, but the predictions are lower than the data. Similar results are obtained for the momentum thickness (Fig. 37), although the difference is not as dramatic. The difference between the two models becomes more obvious, when the velocity profiles are plotted in semilogarithmic coordinates. The results for three locations spanning the flow are presented in Figs. 38 through 40. The models agree in the region where the pressure gradient is still low (Fig. 38), but they differ a lot as it becomes stronger. The comparison indicates that as separation is approached, a log region still exists but the U^+ intercept of the law of the wall seems to be lower, which implies a change in the constant in the law of the wall. This is more clearly indicated in Fig. 41, where the experimentally obtained velocity profiles, for the near separation region, are plotted in semilogarithmic coordinates. As mentioned earlier, the new model assumes that the constants of the law of the wall remain unchanged. As a result, the model will predict a velocity profile which is consistent with this assumption.

The question that arises is why the constant seems to be lower for this region. The answer is not clear but it seems that the appearance of intermittent backflow might be playing an important role. Since the behavior of the flow in the near wall region strongly affects the flow in the logarithmic region, the presence of intermittent backflow which first appears very close to the wall can strongly affect the constant of the log law.

It is interesting to note that in the previous test case (Samuel and Joubert case), all the velocity profiles overlap in the log region, and the predictions reproduce this faithfully. This difference indicates that more research must be performed to determine what is the cause, if any, for this apparent change in the constants. This is beyond the scope of the present work. The next two figures

(Figs. 42, 43) compare the predictions of the new model for the velocity profile at $x=3.01$ meters with those of Pletcher (Fig. 42) and Johnson-King (Fig. 43). The comparison indicates that the new model tends to give a fuller profile for this location. The predictions of the model of Mellor *et al* for the velocity profiles at $x=2.673$ and 2.987 meters are compared to those of the new model in figures 44, 45 respectively. At $x=2.673$ meters, the two models predict velocity profiles that are in closer agreement. At $x=2.987$ meters, both models seem to overpredict the velocity profile in the near wall region. In the outer region the model of Mellor *et al* seem to give predictions that are closer to the experimental observations.

Finally, the stress profiles are presented in Figs. 46-48. Comparison for all stations indicates that the predictions of the new model are in better agreement with the data compared to those of the simple model. Compared to the results of Pletcher (Fig. 49) and Mellor (Fig. 50), the predictions of the new model are again equally well or superior to those of the other models.

The comparison indicates that overall the new model performs as well as any other model examined, and even better for some parameters for the steady flows examined here. This is very encouraging for the extension of the model to the unsteady cases. The results for the unsteady flow of Simpson *et al* follow.

4.5 *Simpson, Chew and Shivaprasad unsteady flow with separation*

This is an experiment very similar to the steady one. The experimenters attempted to recreate an unsteady flow with the mean value of the pressure gradient being almost identical to the one that corresponds to the steady flow. The amplitude of the unsteady motion is approximately equal to 0.3, and the reduced frequency $f = \omega \times L/2\overline{U}_{ei}$ was equal to 0.61. This is a realistic representation of many unsteady flows like flows over helicopter blades, compressors, etc.

The simulation of an unsteady flow is always more complicated and time consuming compared to a steady one. The first major step was to obtain a smooth representation of the experimental velocity profiles at the starting point. The experiment was divided into 96 bins. Data were collected repeatedly for each of the 96 bins and the phase averaged results were reported. The choice of the initial station was again not easy due to the low Reynolds number effects. Taking into account the experience that was gained from the steady case, it was decided that the same x location could be used for the unsteady flow. Since the initial location was in the accelerating portion of the flow, a composite profile consisting of the law of the wall for the inner region and the Coles profile for the outer region, should be able to represent the profiles. The only problem with this approach lies in the selection of the constants for the law of the wall. Because of the low Reynolds number effects, the constants seemed to deviate from the 0.4

and 5.1 values given in the paper but in most of the cases, the difference was very small. It was thus decided that these values would be used for all the profiles.

The accurate representation of the time variation of the free-stream velocity is also important for simulating the flow. According to the experimenters, the free-stream velocity could be written in terms of a Fourier series as follows:

$$U_e = \overline{U}_e(1 + \sum_{i=1}^{n} \frac{\tilde{U}_{ie}}{\overline{U}_e} \cos(\omega t - \phi_{ie}))$$

where $\tilde{U}_{ie}$ is the amplitude of each harmonic, and ϕ_{ie} is the phase lag. The ratio of the first harmonic to the mean velocity was experimentally found to be approximately constant up to x = 3.0 meters. The phase lag (ϕ_{ie}) was approximately 200 degrees. The higher harmonics have amplitudes of less than three percent of the mean value. Based on these observations, the numerical representation of the free-stream velocity includes only the first harmonic. In this case, a phase lag of 196 degrees gives better agreement with the experiment. The mean free-stream velocity for each x station was calculated by averaging the results of three experiental curves obtained on different days.

Based on the experimental results, intermittent backflow of as much as 1.5 percent was measured 0.048 inches from the wall at x=2.8544 m. In order to avoid any numerical problems because of the boundary layer approach used for solving the momentum equations, the end of the domain was selected at x=2.75 meters. The existence of experimental data at this location also made this location a natural choice. The domain was divided into 130 stations in the streamwise direction and 50 nodes in the y direction. The total height of the domain was chosen so that the boundary layer lies well within the numerical domain at all phases. The results from the steady cases were used as a guide for the choices concerning the distribution of the nodal points.

An Euler implicit integration scheme was used for the integration of the momentum equations. The trapezoidal scheme was used for the integration of the auxiliary P.D.E. The cycle was divided into 1350 steps. The selection of the time step took into account both time accuracy and computational cost. The C.F.L number for the Crank-Nickolson scheme was monitored. This was done, because the stability criteria are based on linear analysis considerations. The value of the C.F.L number did not exceed 2 at any point of the cycle. The evolution of the unsteady solution over parts of the cycle using different time steps was used as a test for checking the effect of the time step on the accuracy. Since the unsteady solution is expensive, the choice of the time step is important.

The repeatability of the solution was checked using the maximum shear stress, displacement and momentum thickness as criteria. All of those parameters indicated that by the third cycle a periodic solution was obtained. As an example, the maximum turbulent shear stress at two phases of the cycle is given in Figs. 51 and 52 respectively. Figure 51 clearly shows how the solution changes from a steady first guess (cycle 1) to a fully periodic, unsteady solution (later cycles). The choice of the starting point in time is not by chance. Since initial conditions are not known for the velocity field, it was decided that the calculation should start at a time when the time derivative of the free-stream velocity is zero. Since we use only one harmonic to describe the free-stream velocity, the time derivative is zero for each x. This choice gives a smoother transition to the fully unsteady flow. The starting time was the instance where the free-stream velocity is maximum.

The presentation of the results starts with the average skin friction coefficient. The average skin friction is equal to the average wall shear over a cycle divided by one half the average free-stream velocity value squared. Figure 53 shows the predictions of the new model, the algebraic model, the unsteady data and the steady data. Both models give results in very good agreement with the unsteady experiment up to x = 2.3 m. After this point, the models seem to agree more with the steady solution, while the mean unsteady skin friction seems to assume slightly higher values. Both results are within the experimental uncertainty. Unfortunately, the solution method does not allow for further investigation of the behavior in the region where intermittent flow appears. The reader should recall that the algebraic model does not predict separation in the steady flow. The same seems to be true here, at least up to x=3.0 m.

The next important variable is the displacement thickness. As the reader must recall, in the steady flow, the new model gave improved results over the algebraic model. Here, the comparison indicates that the predictions of the two models concerning the average displacement thickness over a cycle are in good agreement with the experimental results. Although it is not very obvious from Fig. 54, the new model gives much improved predictions concerning the mean velocity profiles as separation is approached. This will become obvious shortly when the velocity profiles are presented. The predictions for the mean momentum thickness (Fig. 55) do not show any difference and are in agreement with the experiment. The same behavior was observed previously for the steady flow results.

The mean velocity profiles for three locations are presented in Figs. 56 through 58. The first two locations, $x = 1.88$ and 2.22 meters do not experience very severe pressure gradient during any phase of the cycle, and this results in accurate predictions from both models. The last location, $x = 2.75$ meters is close to the point where intermittent backflow appears, and has stronger pressure gradients during part of the cycle. The difference in the predictions (Fig. 58) is obvious. The new model proves that it has a superior performance in strong pressure gradients.

Turning attention from the time averaged results to instantaneous variations, we first present the phase lag of the wall shear stress with respect to the free-stream velocity. Both models give almost identical results which are in good agreement with the experiment. Both the numerical and experimental data indicate that the phase lag increases as the pressure gradient becomes stronger, and the backflow starts to appear. The models predict a faster drop than the experiment.

The next figure (Fig. 60) presents the ratio of the 1st harmonic of the wall shear stress to the mean value. Both models seem to predict the same ratio, which is lower than the 0.667 that the experiment seems to indicate. The two models tend to indicate an increasing amplitude as the pressure gradient becomes stronger and backflow appears, which is in contrast with experimental results. The same behavior but with a sharper increase is exhibited by the quasi-steady model of Houdeville & Cousteix [73, 74]. The derivation of the later starts the steady flow skin friction law that is derived based on the velocity-defect law. By introducing phase-averaged quantities into the equation and by expanding the result, terms for the oscillatory flow are produced. A more detailed description of the derivation is given in the references.

The ratio of the first harmonic of the velocity to the mean value as a function of y for the location x=2.74 meters is presented in figure 61. The comparison indicates that both the new model and the simple algebraic model predict the correct trends but, the new model gives values that are in better agreement with the experimental results. The phase lag of the first harmonic is as predicted from the two models for x = 2.74 meters is shown in figure 62. Since no data are presented for this station in [69], two other stations one in the attached portion of the flow and one near the location where intermittent detachment is observed are used for comparison. The comparison indicates that both models depict the same trends which are in agreement with the experimental results. The values that they predict are slightly lower than the experimental ones.

The next four figures (Fig. 63 - 66) compare the velocity profiles predicted from the two models and the experiment for x=2.74 meters. These are the phase averaged profiles that correspond to the following phases: a) the free-stream velocity has its minimum value, b) the free-stream velocity is equal to the average velocity and increasing, c) the free-stream velocity is maximum, and d) the free-stream velocity is equal to the average value and decreasing. All four figures indicate that the new model gives profiles that are in better agreement with the experimental profiles compared to the simple algebraic model. This result clearly shows that the new model gives superior predictions, compared to the algebraic model, for both the time and phase averaged velocity profiles.

Discussion

Chapter 5

5.1 Discussion

A new, general and rational approach has been developed for the prediction of steady and unsteady, turbulent boundary layer flows under the presence of strong adverse pressure gradients up to separation. The foundations of the new method are based on experimental observations.

The model uses the integrated T.K.E equation in an attempt to take into account the "history" effects of turbulence. The use of the integrated form of the T.K.E equation eliminates the need for any assumptions concerning the path of the maximum shear stress. This becomes very important in the case of unsteady flows where the assumption that the path is parallel to the x-axis is questionable. The integrated formulation also eliminates the diffusion term of the equation, the modeling of which is uncertain. The resulting auxilliary differential equation governs the develpment of the maximum shear stress which is a scaling parameter. A mixing length approach is used for describing the stress profile across the boundary layer. A model based on the rigorous distribution of the near wall shear stress has been developed for the inner mixing length. The mixing length for the outer region is assumed proportional to the boundary layer thickness, but the proportionality constant can vary with the streamwise distance. The variation of the this factor is governed by the requirement that the maximum value of the stress profile must be equal to the value that the auxilliary equation predicts.

The new model also incorporates the important contribution of the normal stresses in the T.K.E production. This term has been modeled in an approximate, but rational way. In order to account for the change of the turbulence structure as separation is approached, a model has been incorporated for the variation of the Bradshaw constant α_1. It was also found that the variation of the outer layer dissipation constant proportionally with the mixing length constant improved the results.

The complete model was implemented into a Finite Element Method code solving the boundary layer equations. The implementation of the model into any other numerical method is straightforward. The model is designed in such way that the momentum equations solver sees it only as a mean of providing eddy viscosity values.

The model was tested against four flow cases. For the turbulent flat plate case, the model gave identical results with the simple algebraic model proving that no violation of the physics was introduced. The next two cases tested the ability of the model for steady flows in the presence of strong pressure gradients up to, but not including, separation. Solving for the separated zone was avoided for two main reasons: a) the boundary layer equations are not valid in separated flows, and b) the mixing length approach is not meaningful in the separated flow. The new model gave improved results compared to the algebraic model for all flow variables. Specifically, the new model gave excellent results for all flow variables when compared with the experimental results of Samuel and Joubert. The predictions of the model, for this case, are also equally well or better when compared to the predictions of other turbulence models examined. For the Simpson experiment, which has a much stronger pressure gradient the results were improved over the algebraic model. Some differences with the experimental results may be the result of the some of the modeling assumptions breaking down very close to separation. In general though, the new model exhibited the correct trends for this test case. The real strength of the model becomes obvious when the velocity profiles are plotted on a semilogarithmic scale. Unlike the algebraic model, the new model reproduces the law of the wall, as the experimental results indicate. The model assumes universal constants for the law of the wall, and its predictions are consistent with this assumption. The indication that this may not be exactly the case very close to separation must be further examined experimentally. Even if this is the case, the model can incorporate this with some computational cost, since the integrals in the mixing length will be functions of x and y, and they will have to be evaluated for the different streamwise locations.

For the unsteady flow, the new model showed improved performance in predicting the time average values of the flow variables. The velocity profiles near separation are in excellent agreement with the experimental data. The good agreement between the predicted and the experimentally phase averaged velocity profiles indicates the ability of the model to give superior results not only in the time averaged sense but also for each phase of the cycle.

The framework presented in this work is general and rational. It can be extended to the calculation of three dimensional and separated flows. In such efforts, it is important to always keep in mind the physics that the experimental data reveal. Such data indicate that mixing length or eddy viscosity approaches are not applicable in separated flows and that the use of the law of the wall as the basis for developing mixing length models is not appropriate for three-dimensional flows. In the next section, some directions for further research are presented.

5.2 Future directions

The present method has shown some promising features in predicting flows with strong pressure gradients. There are still many things that should be investigated.

A question that must adressed is the question of the constants of the law of the wall. More experimental effort must be devoted to answering the question if those constants are affected by strong pressure gradients. Some experiments [63] and a recent Direct Numerical Calculation [62] seem to indicate that the constants are affected, but both results have been obtained for low Reynolds numbers based on momentum thickness. It would be useful to test some of the existing formulas [12, 75, 76, 77] for the variation of the constants as functions of the pressure gradient or the Reynolds number.

Another significant issue is the variation of the dissipation length in the proximity of separation. Here, it is assumed that for the inner region the dissipation and mixing length are equal, which implies that the production is equal to dissipation. Experimental results [55] indicate that the dissipation length reduces even in the near wall region as separation is approached.

The application of the model in three-dimensional cases requires more assumptions, since no universal wall law is known, and one must also deal with the anisotropy of the eddy viscosity.

The next step must be the extension of the method to the calculation of the separated regions of the flow. As we mentioned, earlier a mixing length or eddy viscosity approach is not consistent with experimental data and must be avoided. There exist several experimental observations that must be used in arriving at a new model for the near wall region. The most important are: a) the T.K.E production is almost zero in the recirculating zone, b) energy is brought from the outer section of the flow through entrainment due to the large eddies, c) the turbulent shear stress is almost zero in the separated zone, and d) the maximum shear stress is still an appropriate scaling parameter for the flow, e) there exists large hysterisis within the separated flow region.

The treatment of flows with separation requires coupling with a Navier-Stokes formulation. It will also require a method of transition from the mixing length model to the model for the separated flow. An approach similar to the one that is presented in [68] (see eqn. 9 of the paper) seems possible for the near wall region. For some more ideas concerning the modeling of the separated region the reader must consult Appendix B.

FIGURES

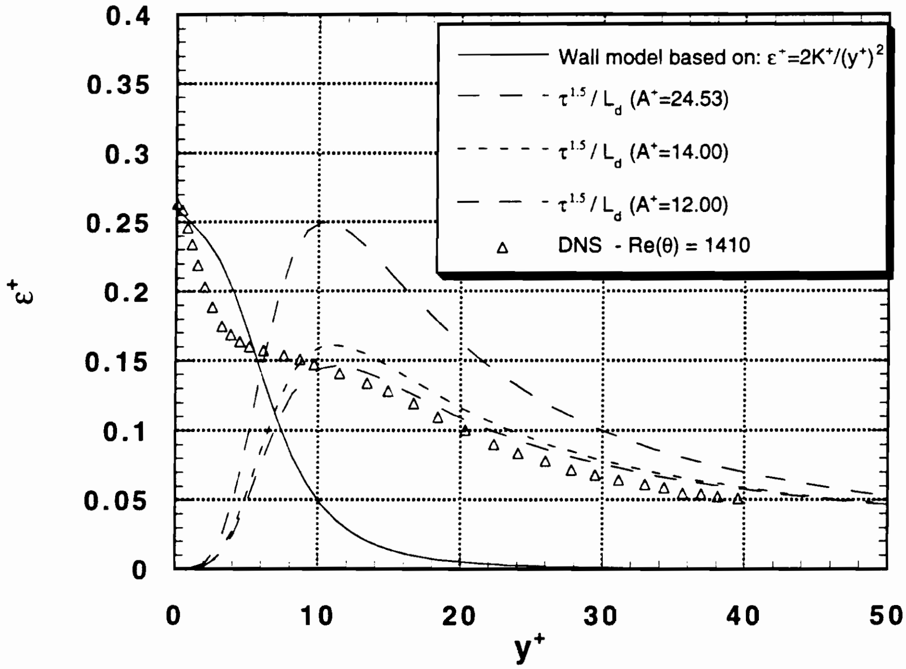

Figure 1. : Nondimensional dissipation in the near wall region. The effect of the damping constant, DNS results, and viscous sublayer model.

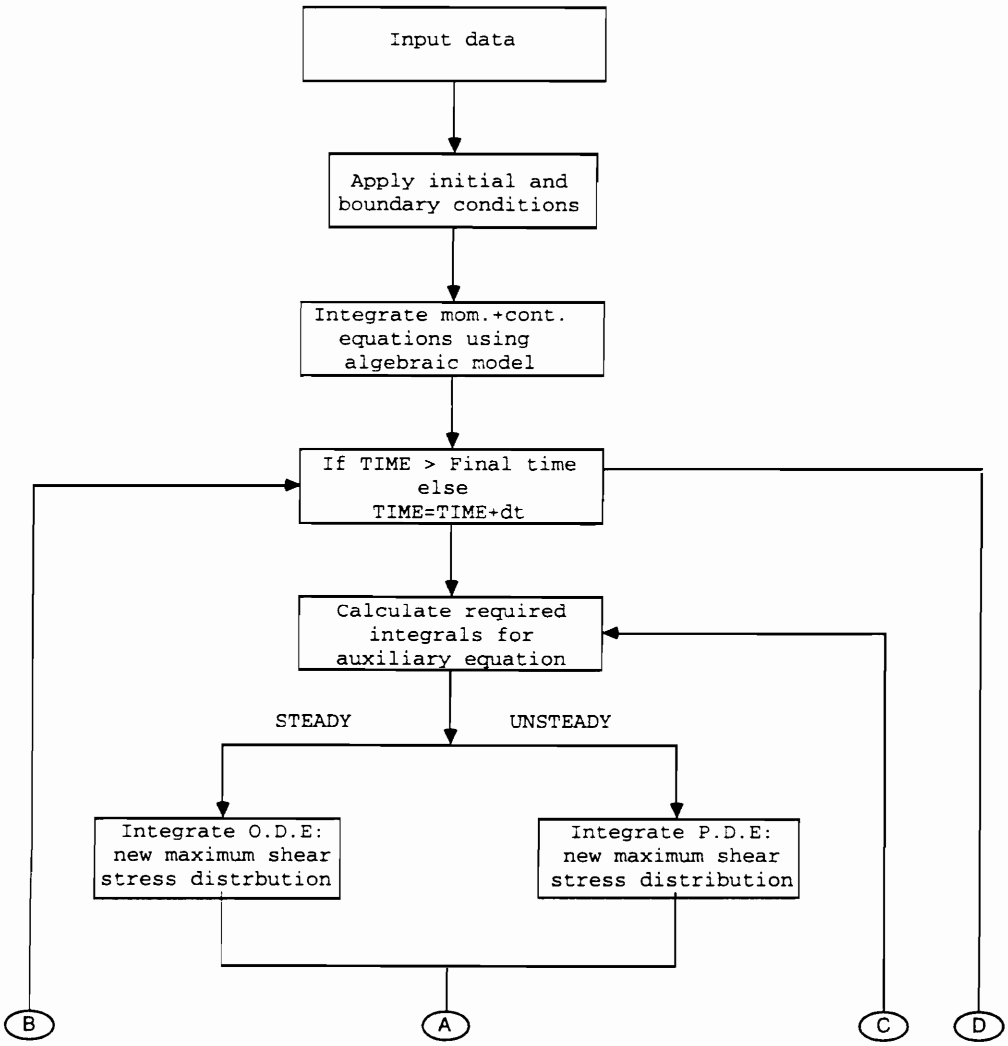

Figure 2. : Flow chart. Implementation of the new turbulence model in the flow solver.

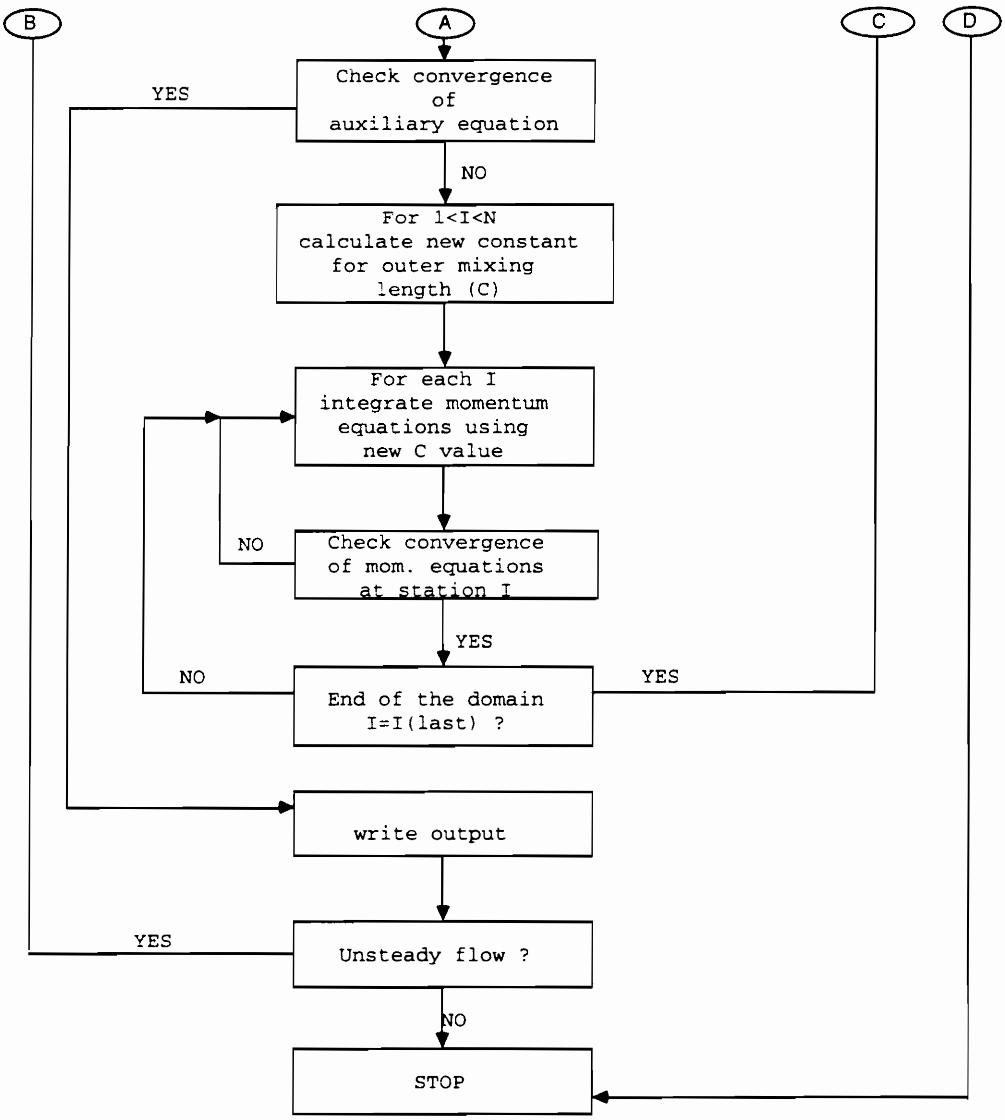

Figure 3. : Flow chart. Implementation of the new turbulence model in the flow solver (cont'd).

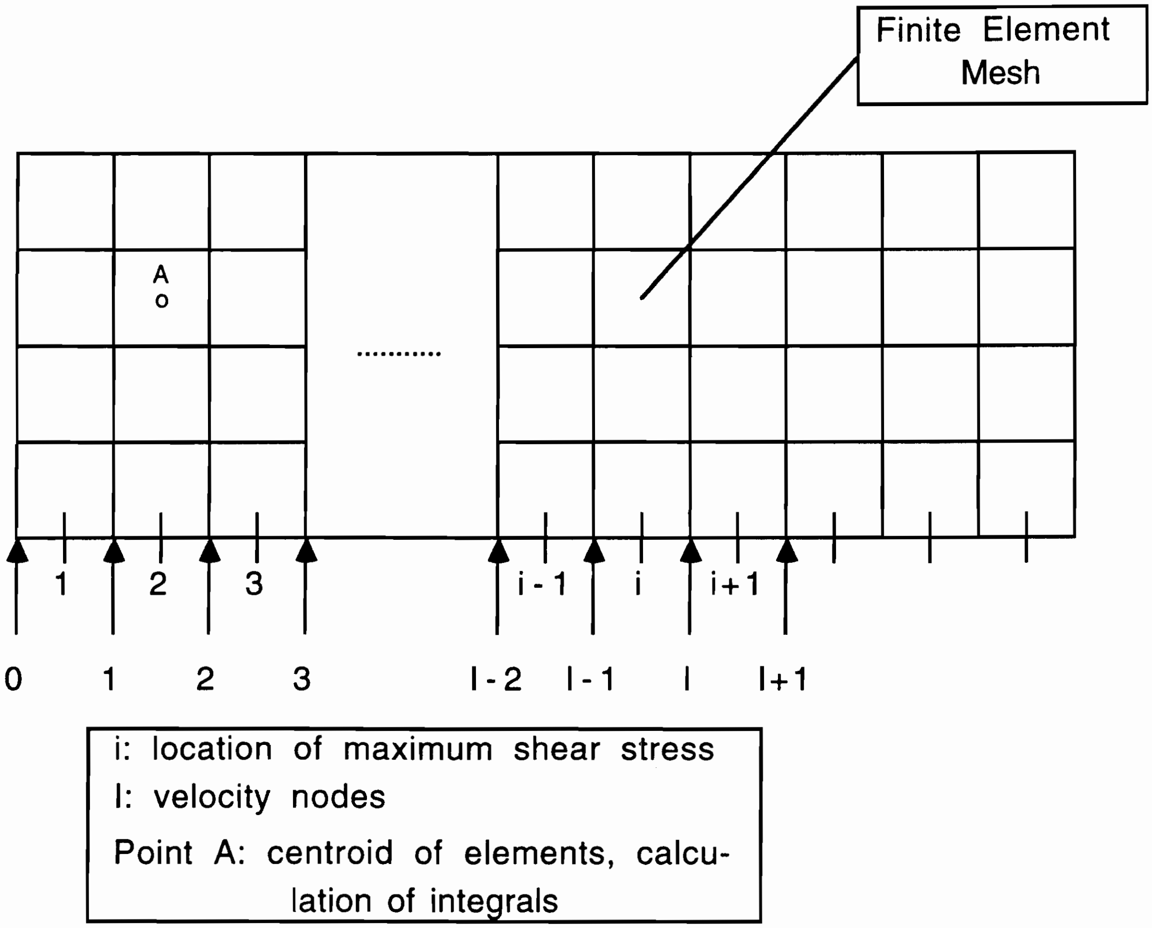

Figure 4. : Velocity and maximum shear stress nodal locations in the mesh.

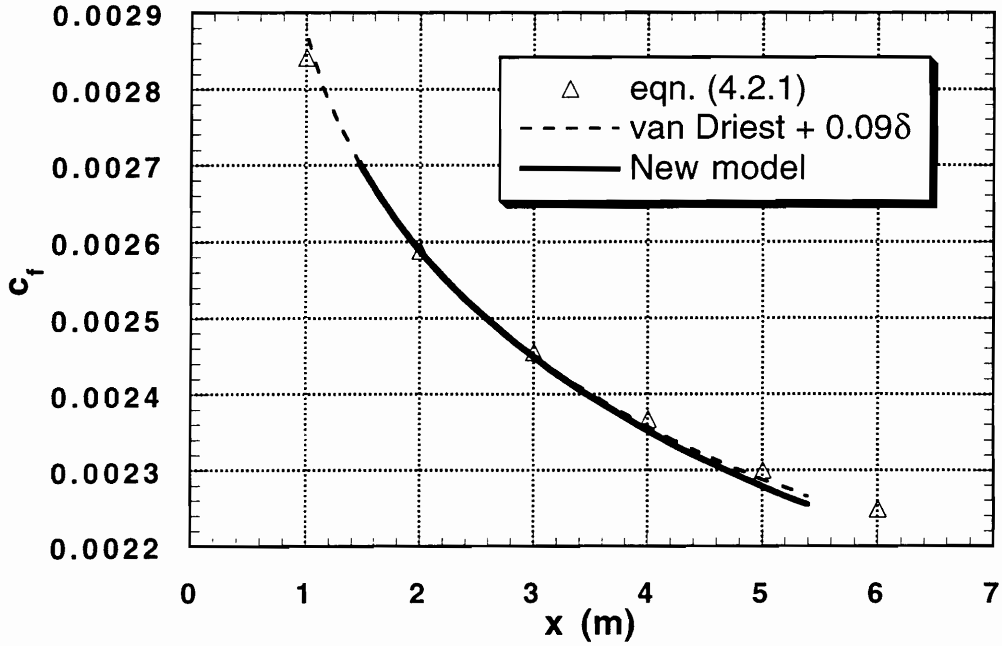

Figure 5. : Turbulent flow over a flat plate. Skin friction coefficient.

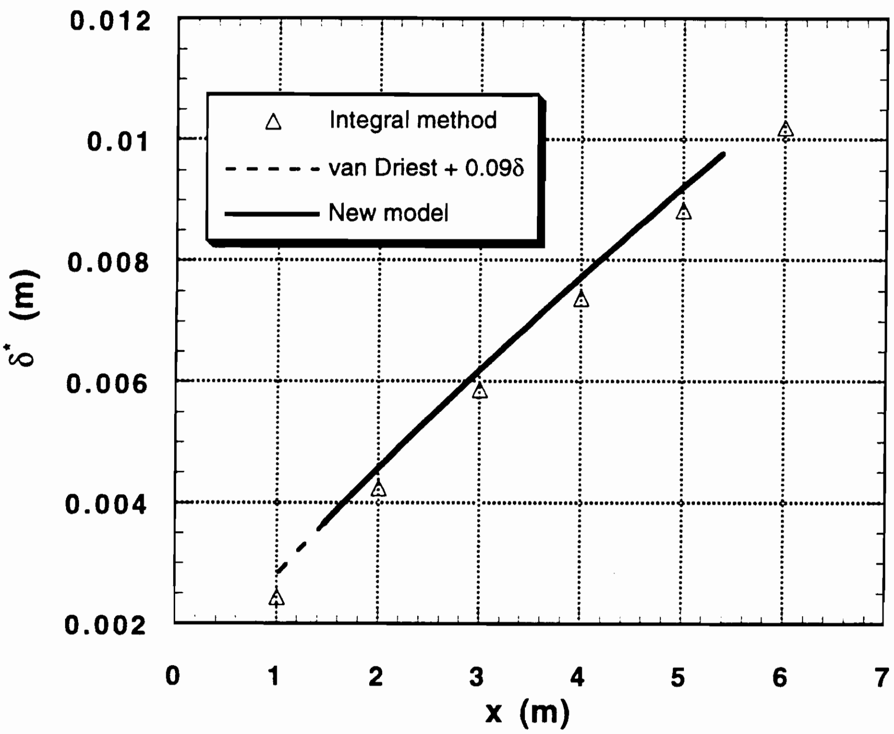

Figure 6. : Turbulent flow over a flat plate. Displacement thickness.

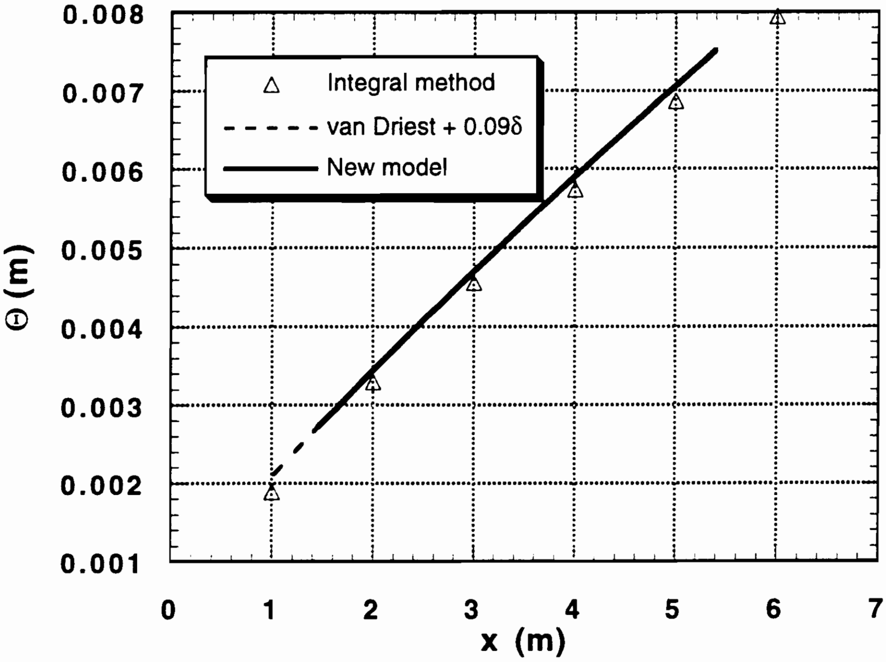

Figure 7. : Turbulent flow over a flat plate. Momentum thickness.

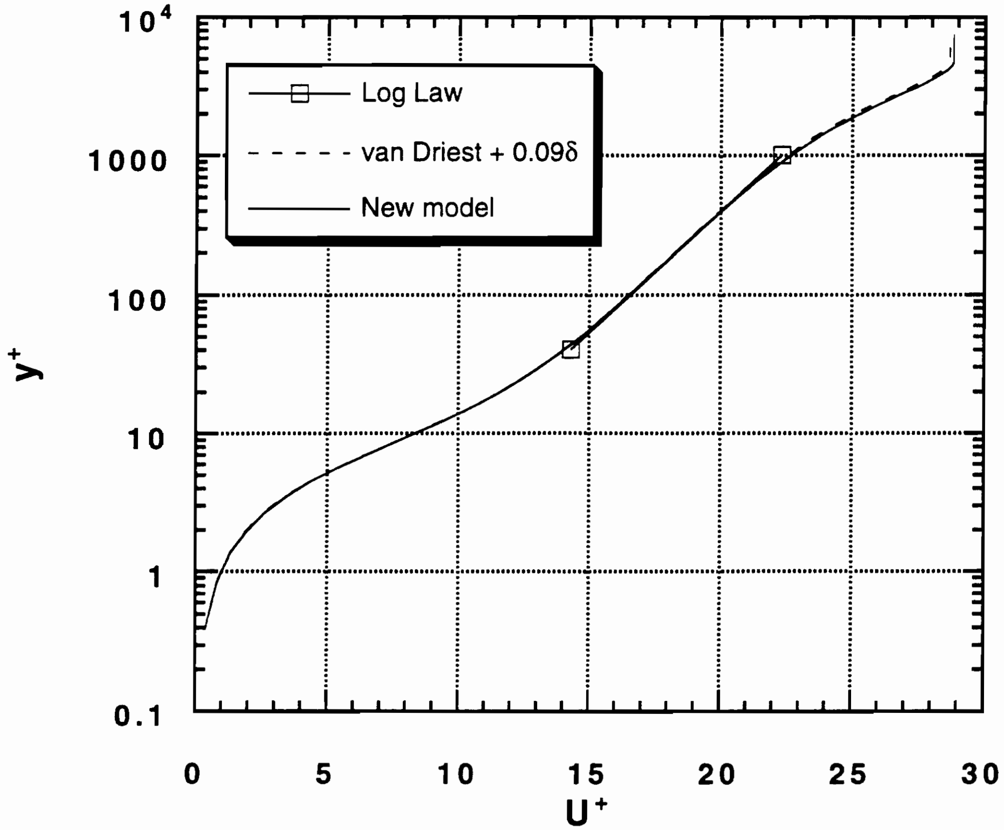

Figure 8. : Turbulent flow over a flat plate. Velocity profile in semilogarithmic coordinates. Re(θ) = 12000.

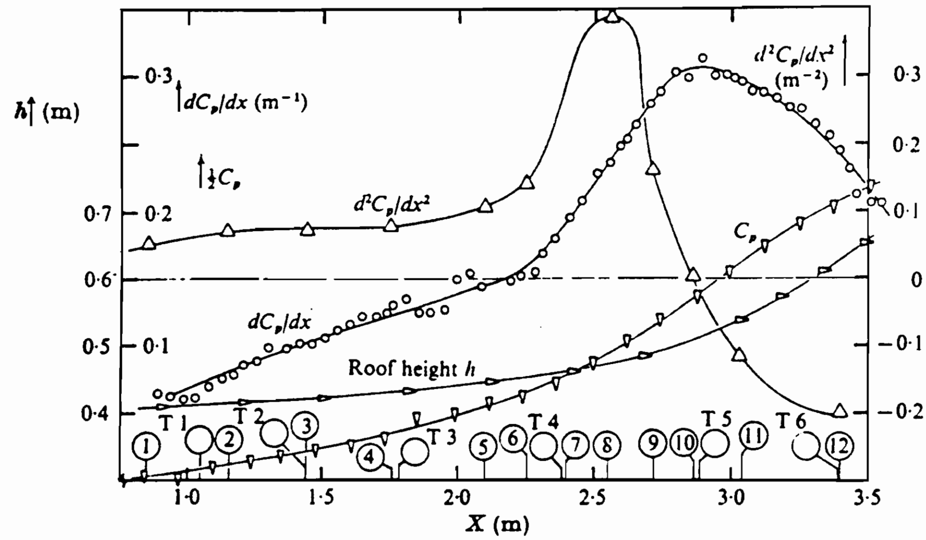

Figure 9. : Samuel and Joubert experiment. Characteristics of the pressure gradient.

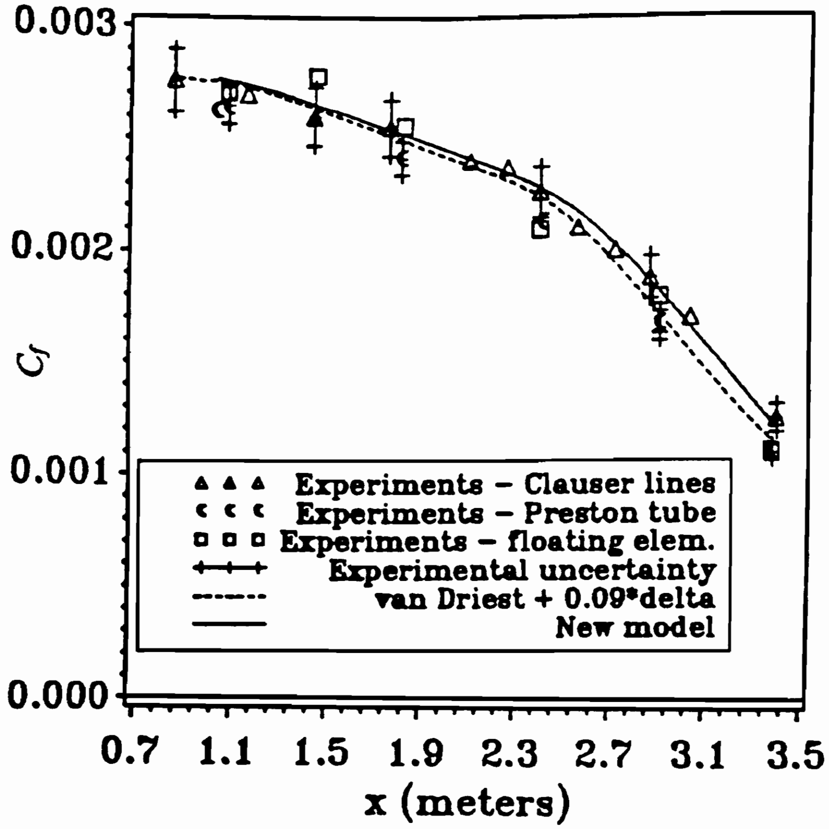

Figure 10. : Samuel and Joubert experiment. Skin friction coefficient.

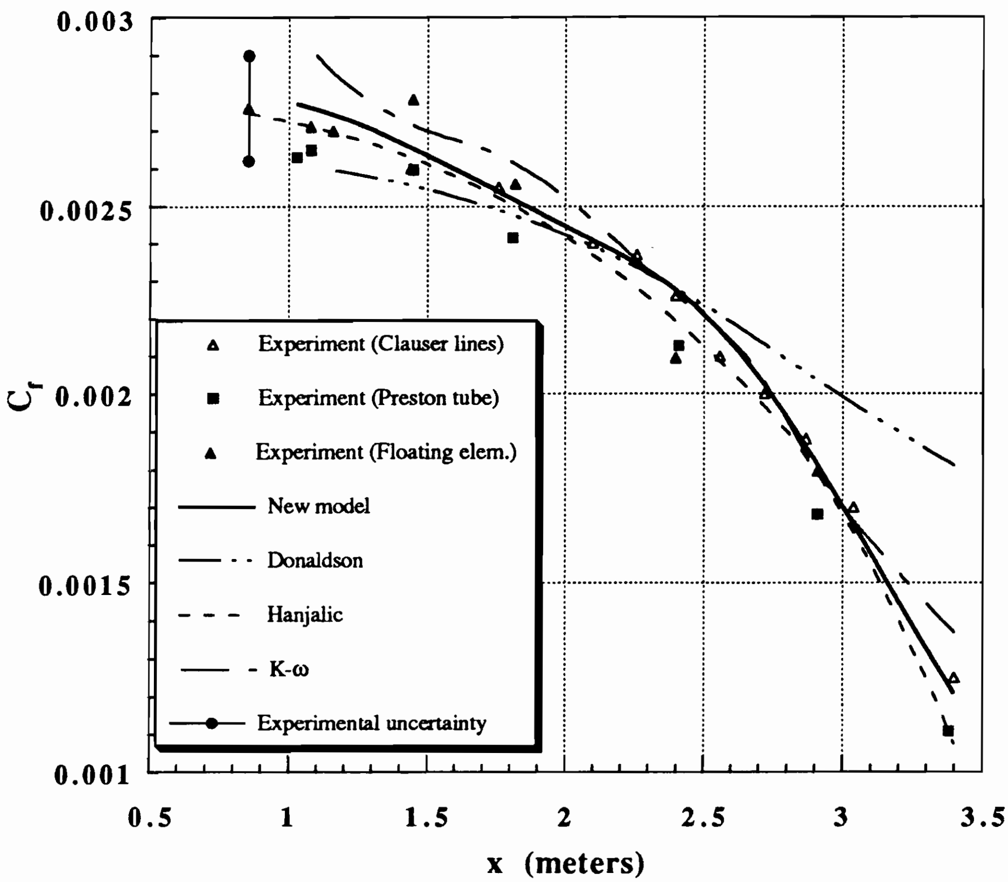

Figure 11. : Samuel and Joubert experiment. Skin friction coefficient. Comparison with other models.

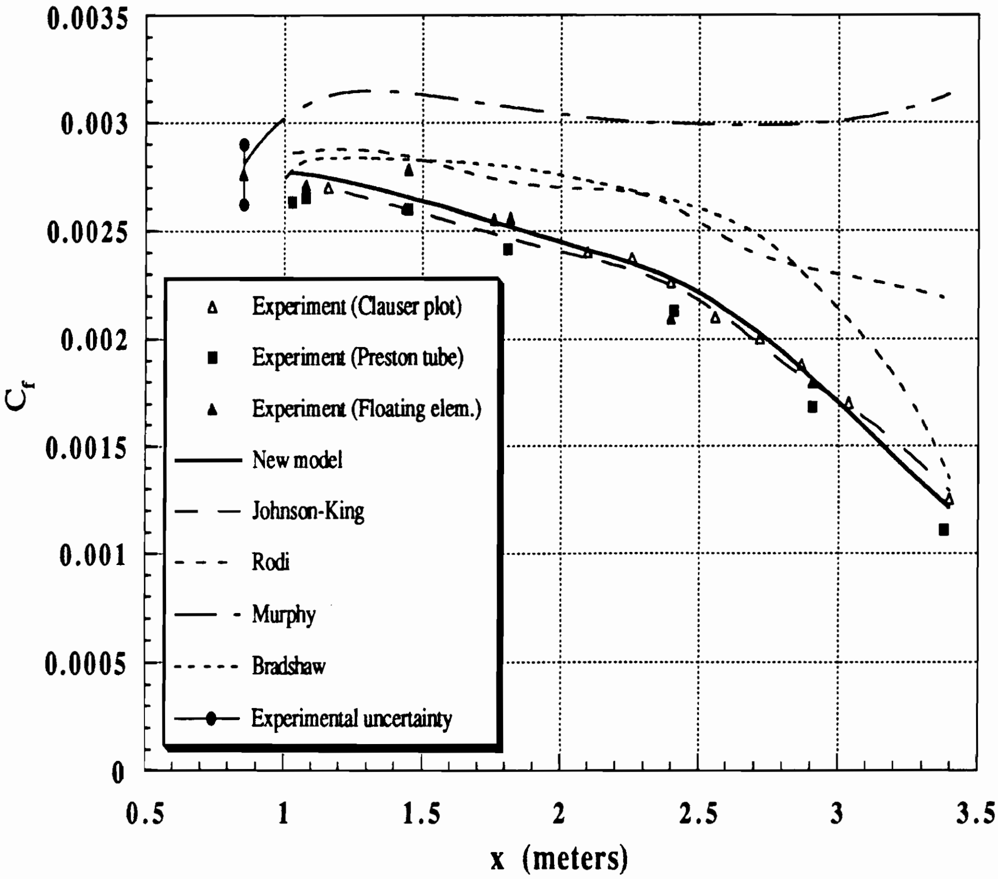

Figure 12. : Samuel and Joubert experiment. Skin friction coefficient. Comparison with other models.

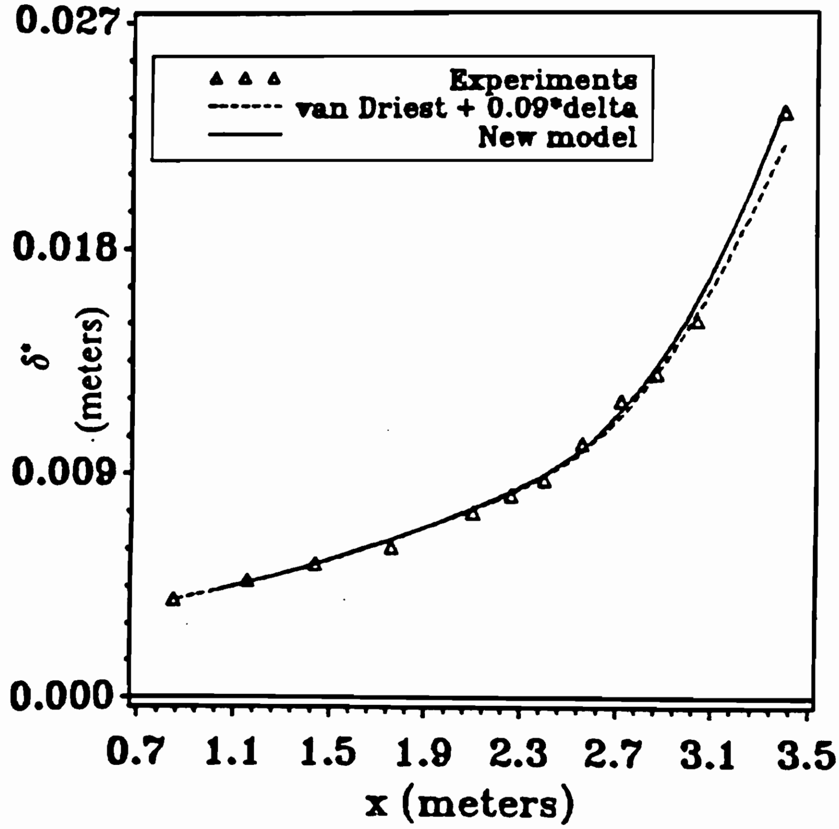

Figure 13. : Samuel and Joubert experiment. Displacement thickness.

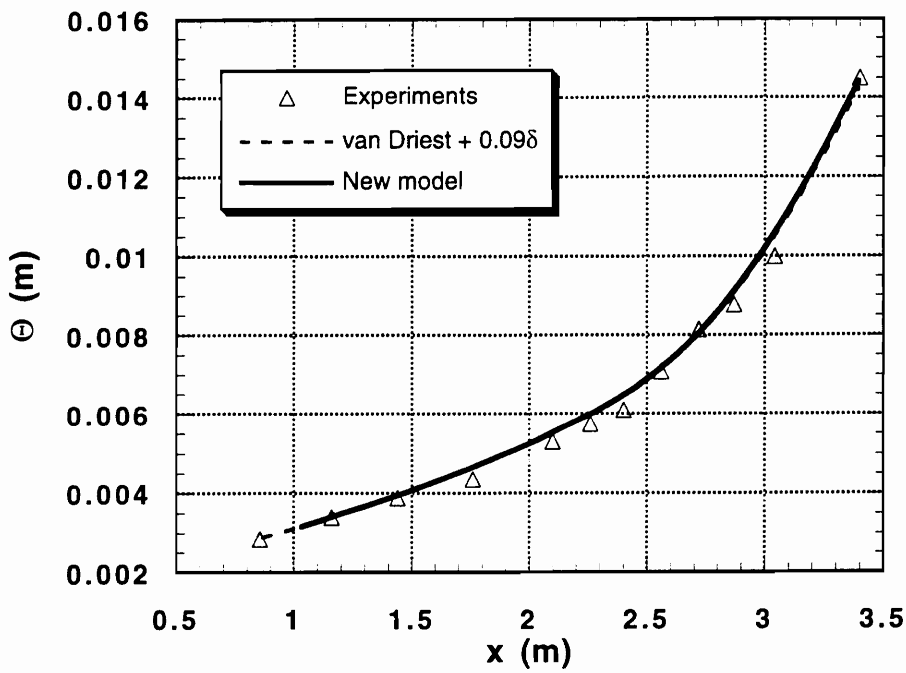

Figure 14. : Samuel and Joubert experiment. Momentum thickness.

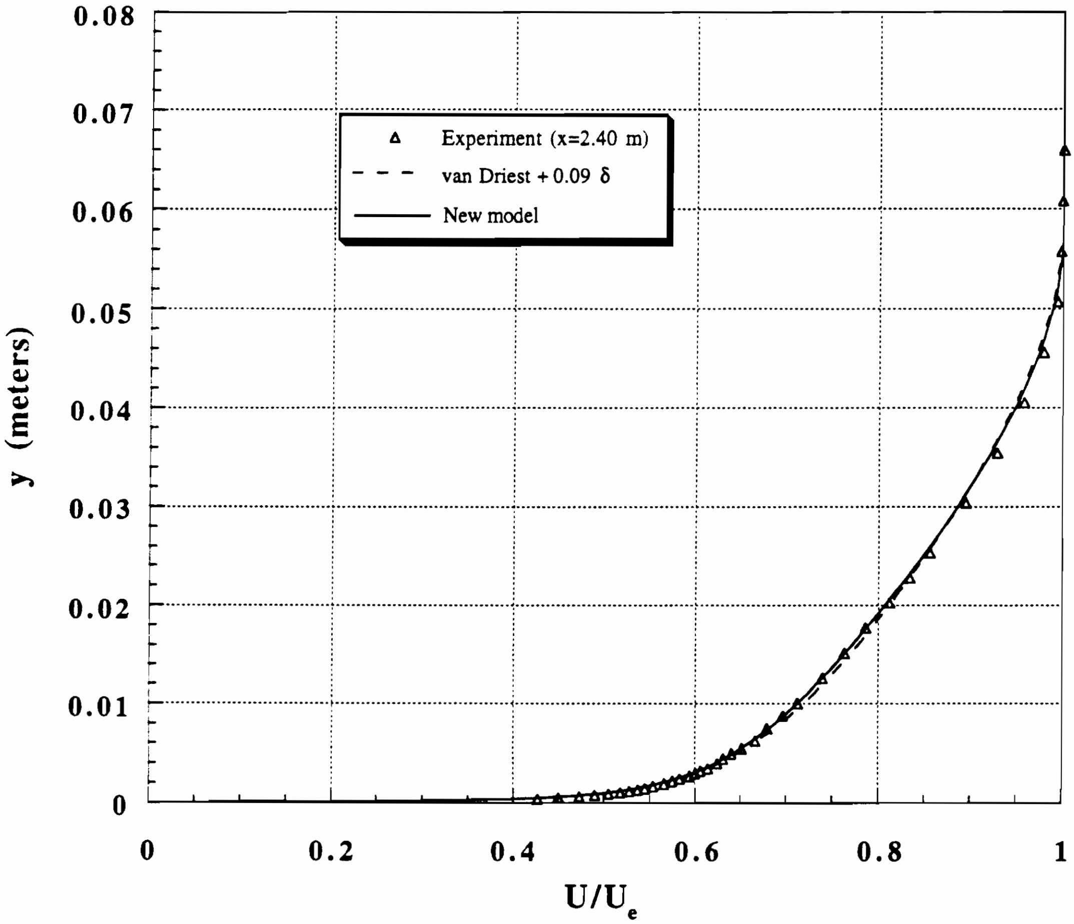

Figure 15. : Samuel and Joubert experiment. Velocity profile at x = 2.40 (m).

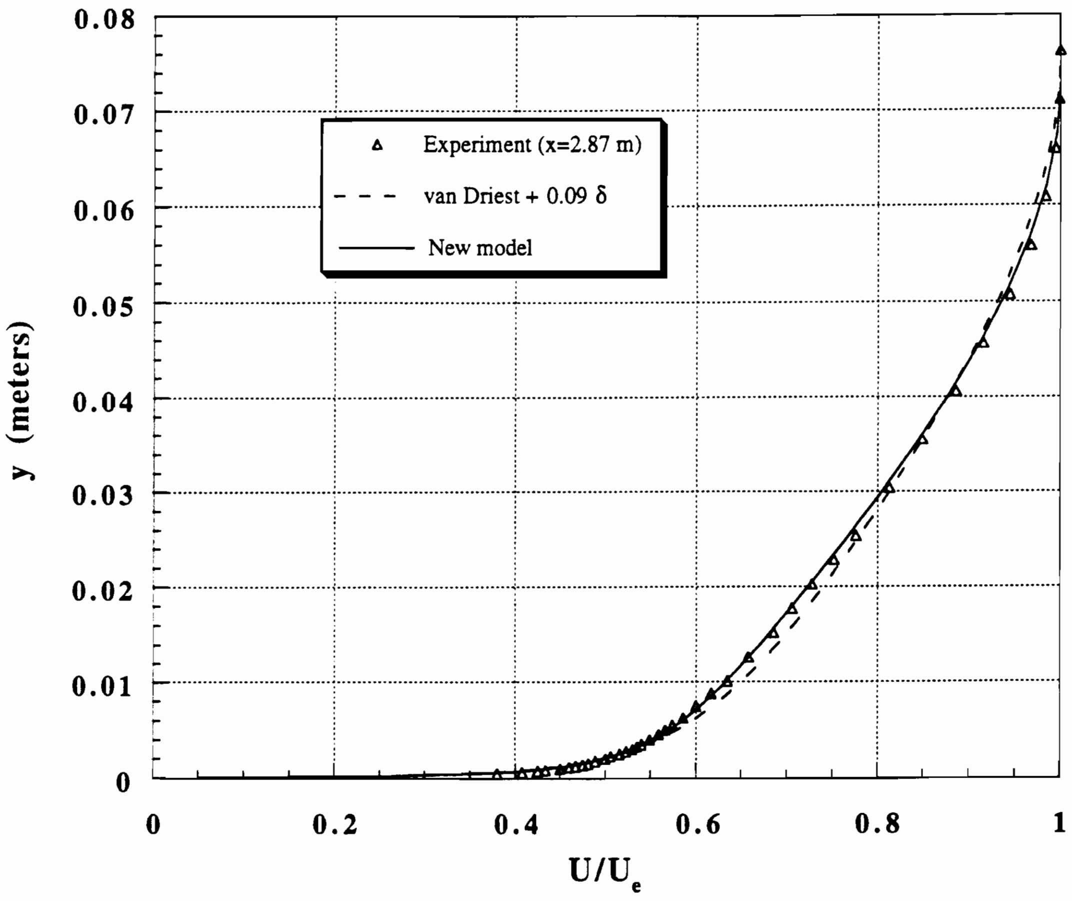

Figure 16. : Samuel and Joubert experiment. Velocity profile at x = 2.87 (m).

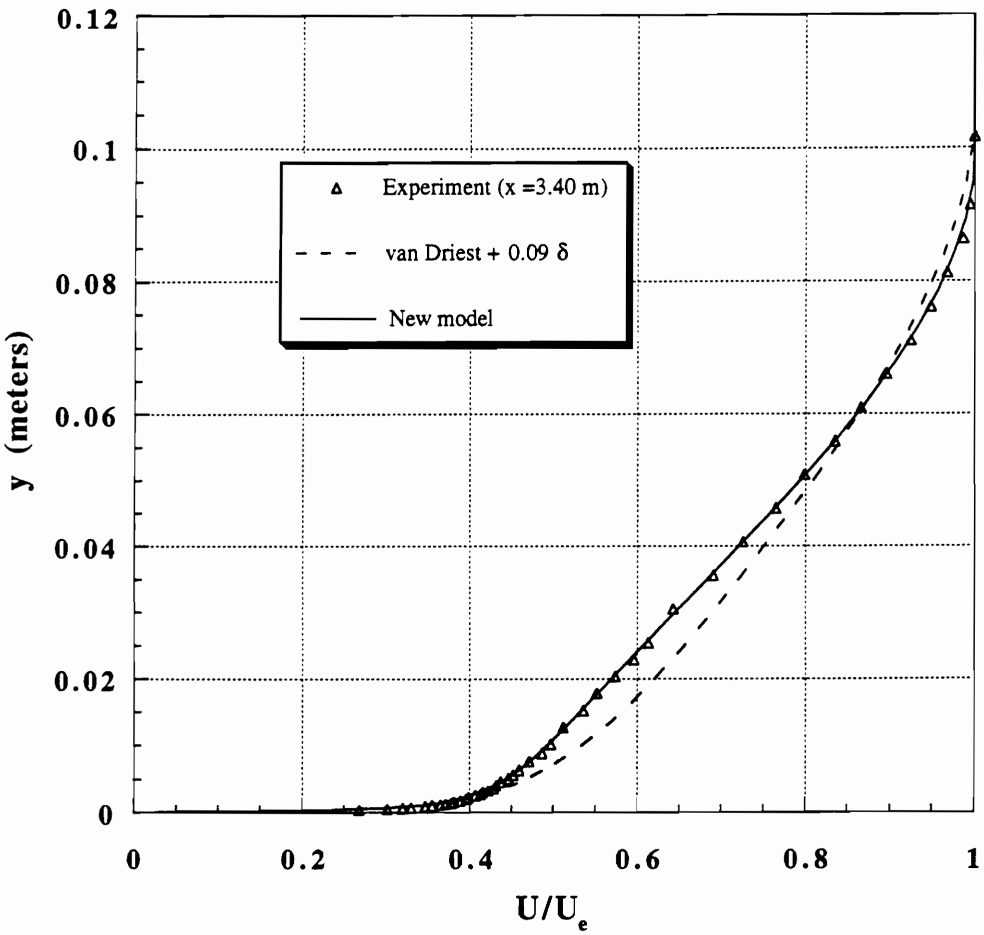

Figure 17. : Samuel and Joubert experiment. Velocity profile at x = 3.40 (m).

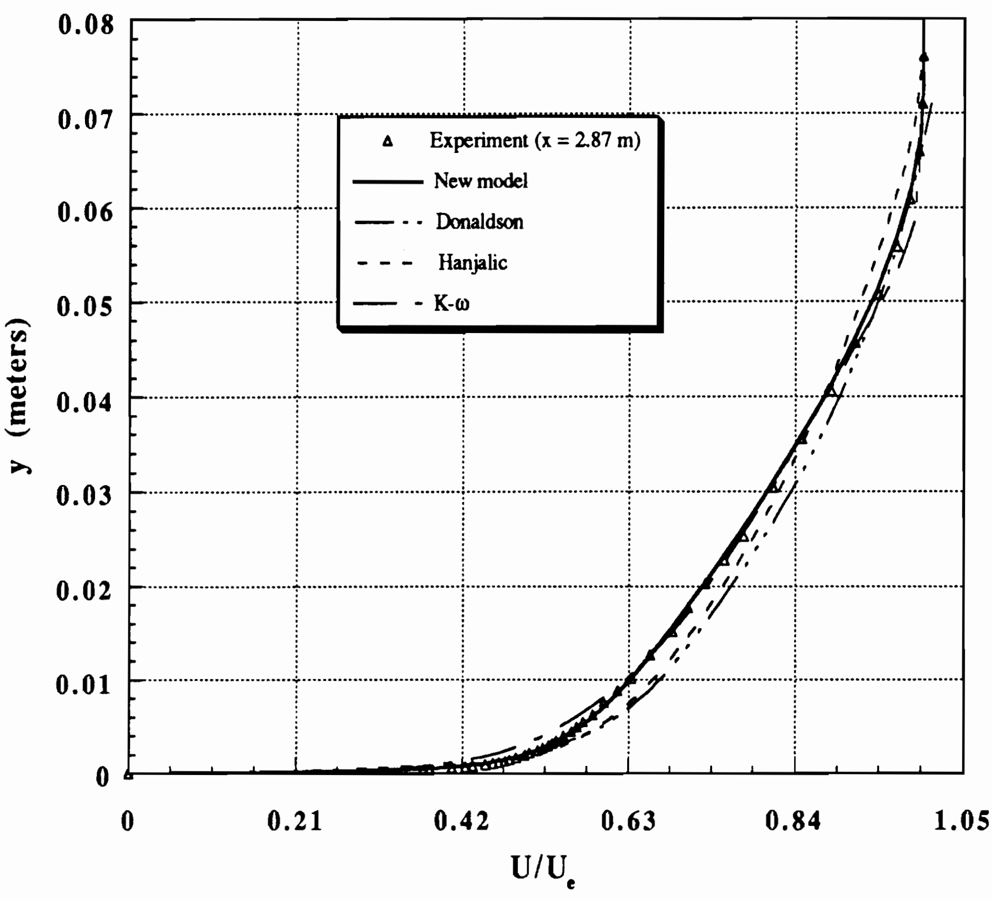

Figure 18. : Samuel and Joubert experiment. Velocity profile at x=2.87 (m). Comparison with other models.

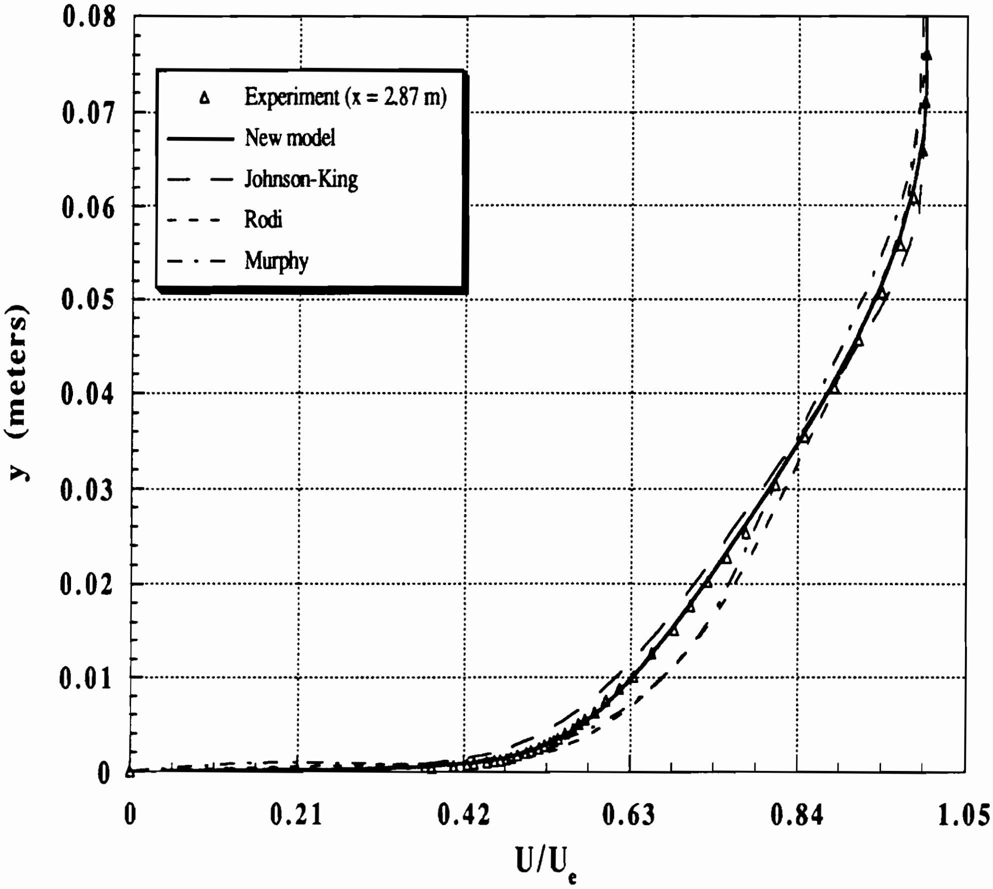

Figure 19. : Samuel and Joubert experiment. Velocity profile at x = 2.87 (m). Comparison with other models.

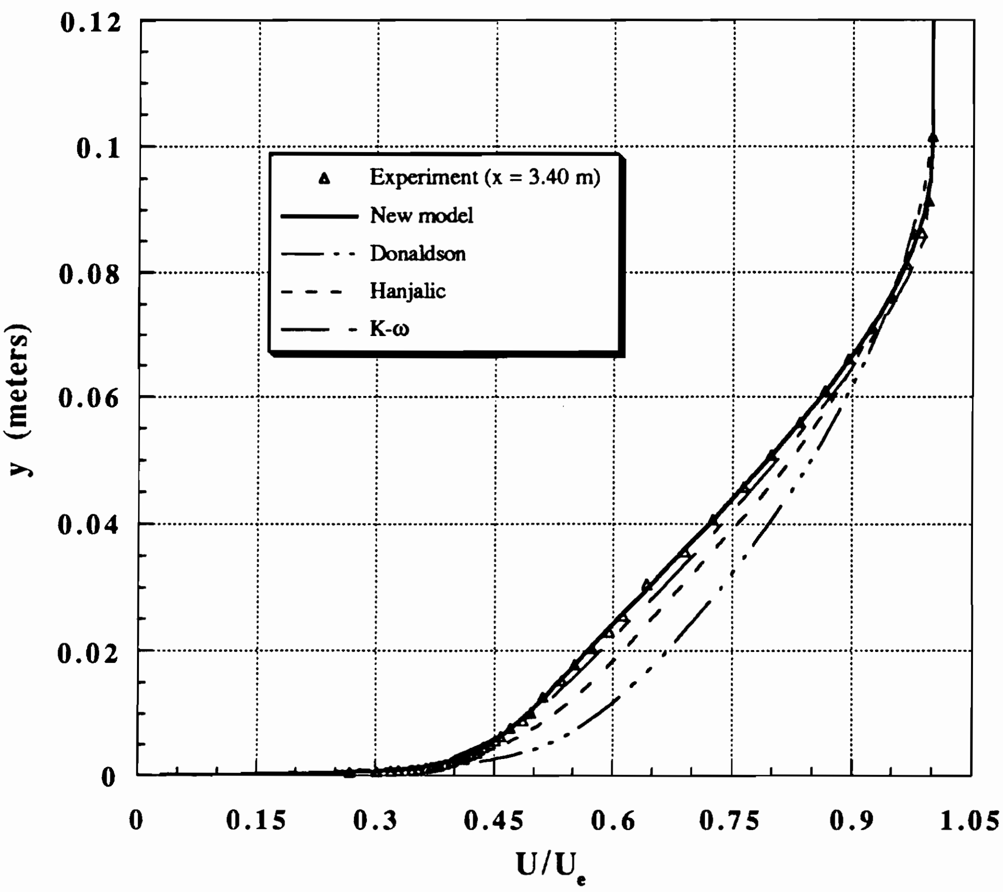

Figure 20. : Samuel and Joubert experiment. Velocity profile at x = 3.40 (m). Comparison with other models.

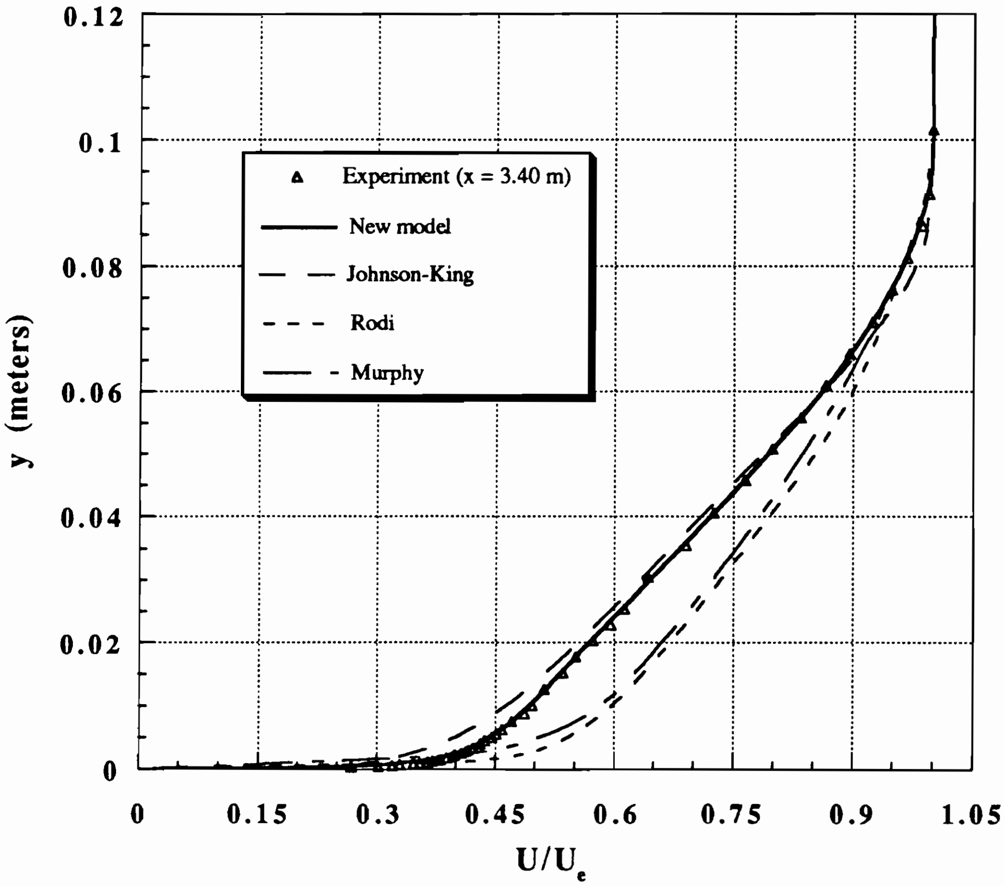

Figure 21. : Samuel and Joubert experiment. Velocity profile at x = 3.40 (m). Comparison with other models.

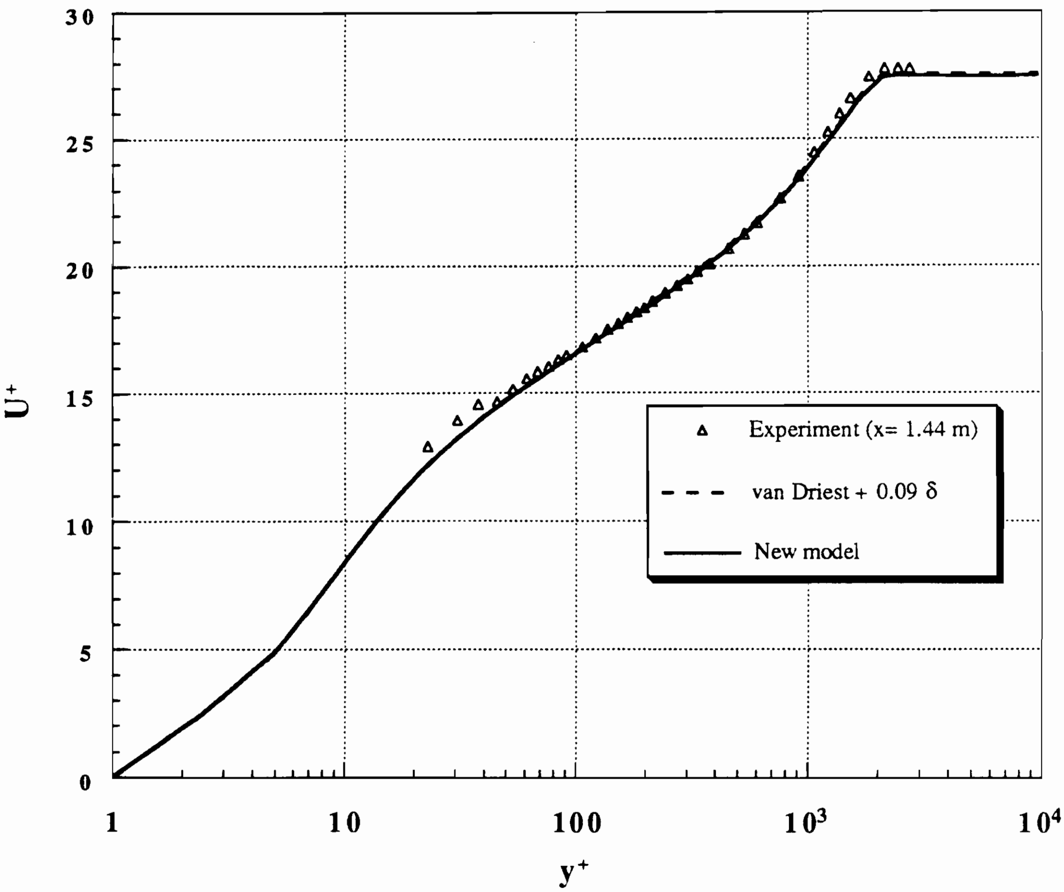

Figure 22. : Samuel and Joubert experiment. Velocity profile at x = 1.44 (m). Semilogarithmic plot.

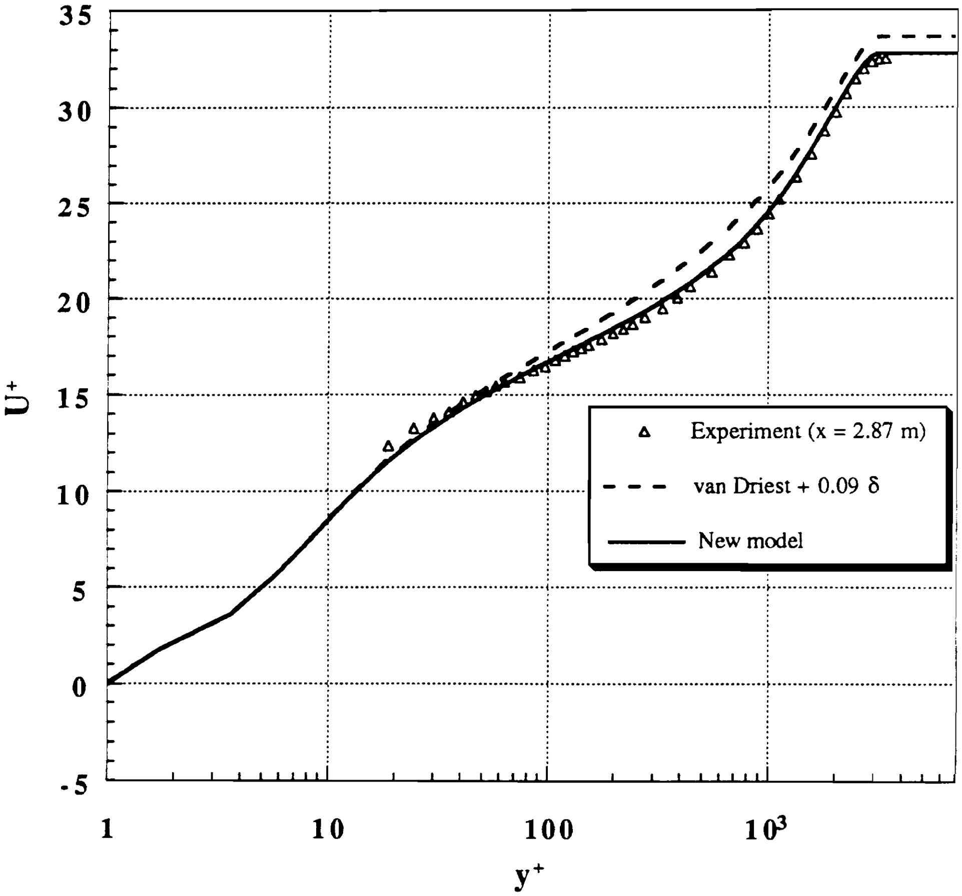

Figure 23. : Samuel and Joubert experiment. Velocity profile at x=2.87 (m). Semilogarithmic plot.

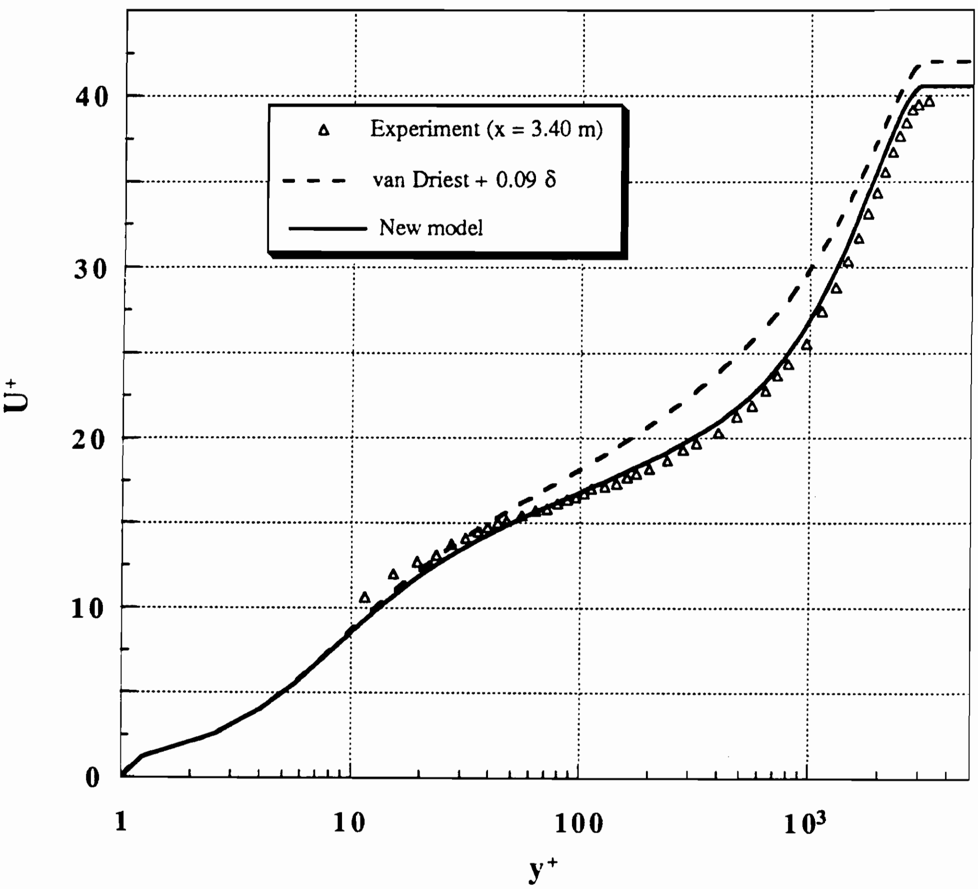

Figure 24. : Samuel and Joubert experiment. Velocity profile at x = 3.40 (m). Semilogarithmic plot.

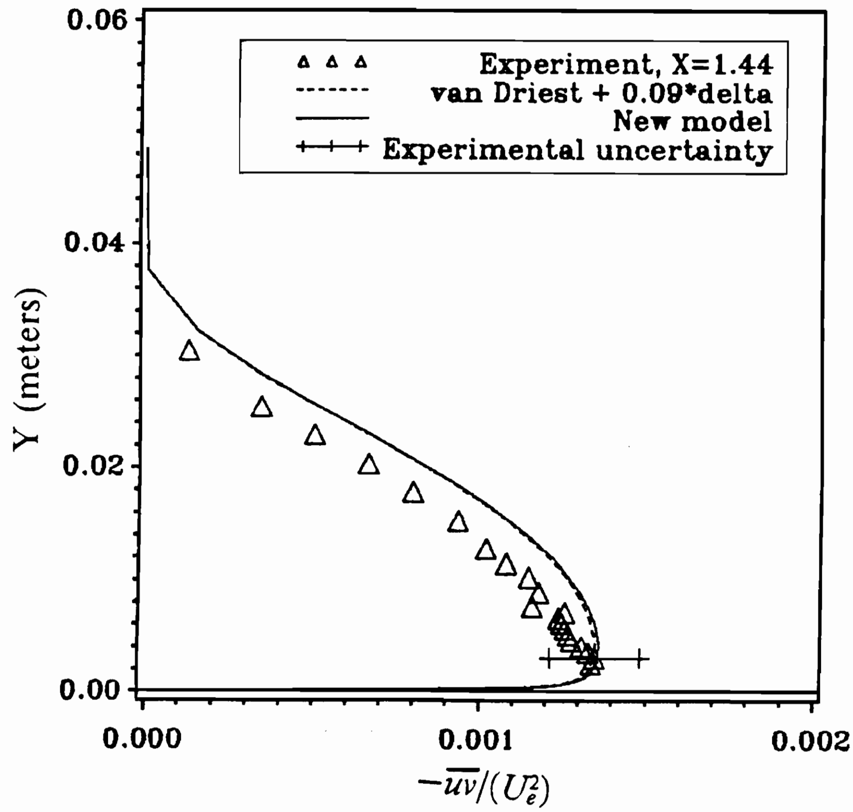

Figure 25. : Samuel and Joubert experiment. Stress profile at x= 1.44 (m).

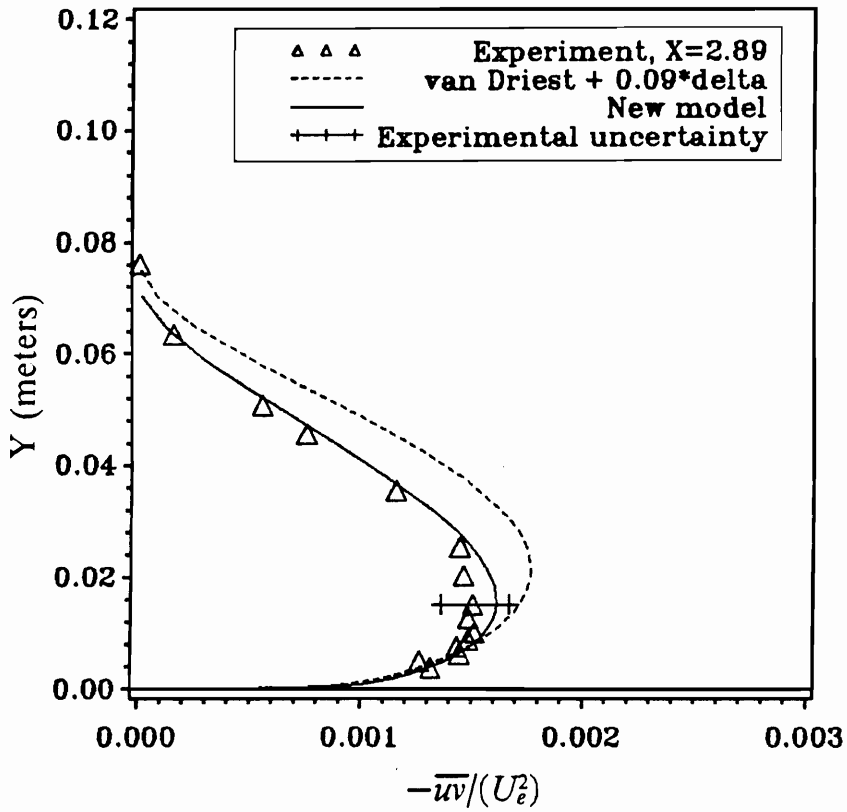

Figure 26. : Samuel and Joubert experiment. Stress profile at x = 2.89 (m).

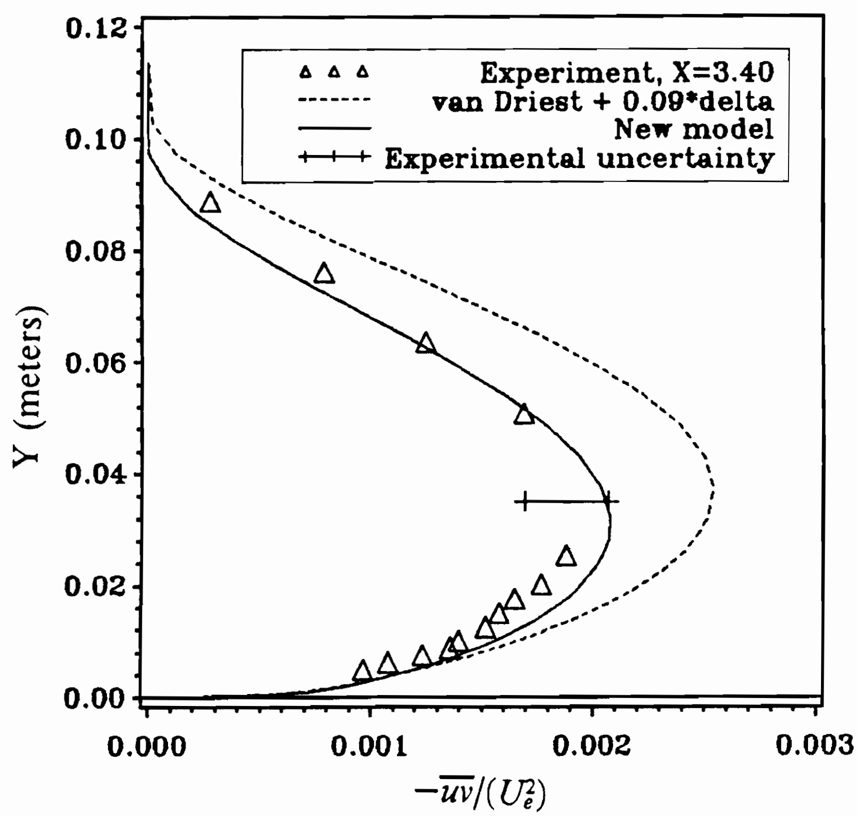

Figure 27. : Samuel and Joubert experiment. Stress profile at x = 3.4 (m).

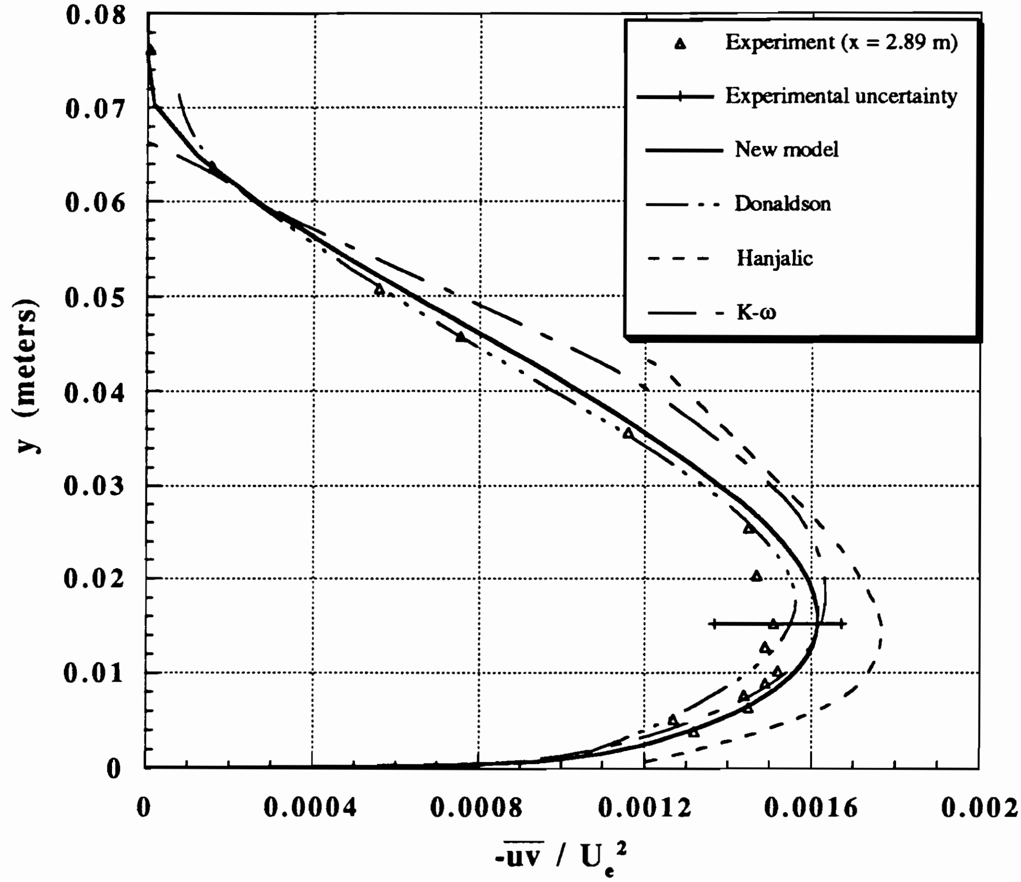

Figure 28. : Samuel and Joubert experiment. Stress profile at x=2.89 (m). Comparison with other models.

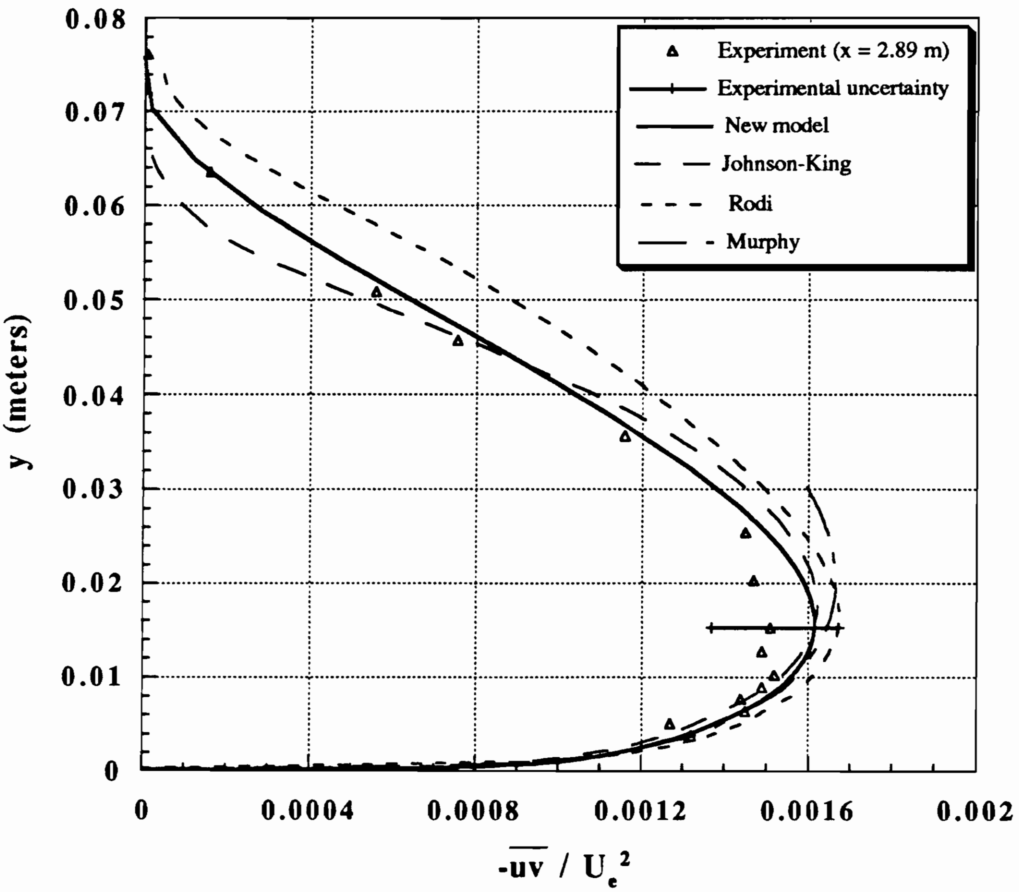

Figure 29. : Samuel and Joubert experiment. Stress profile at x=2.89 (m). Comparison with other models.

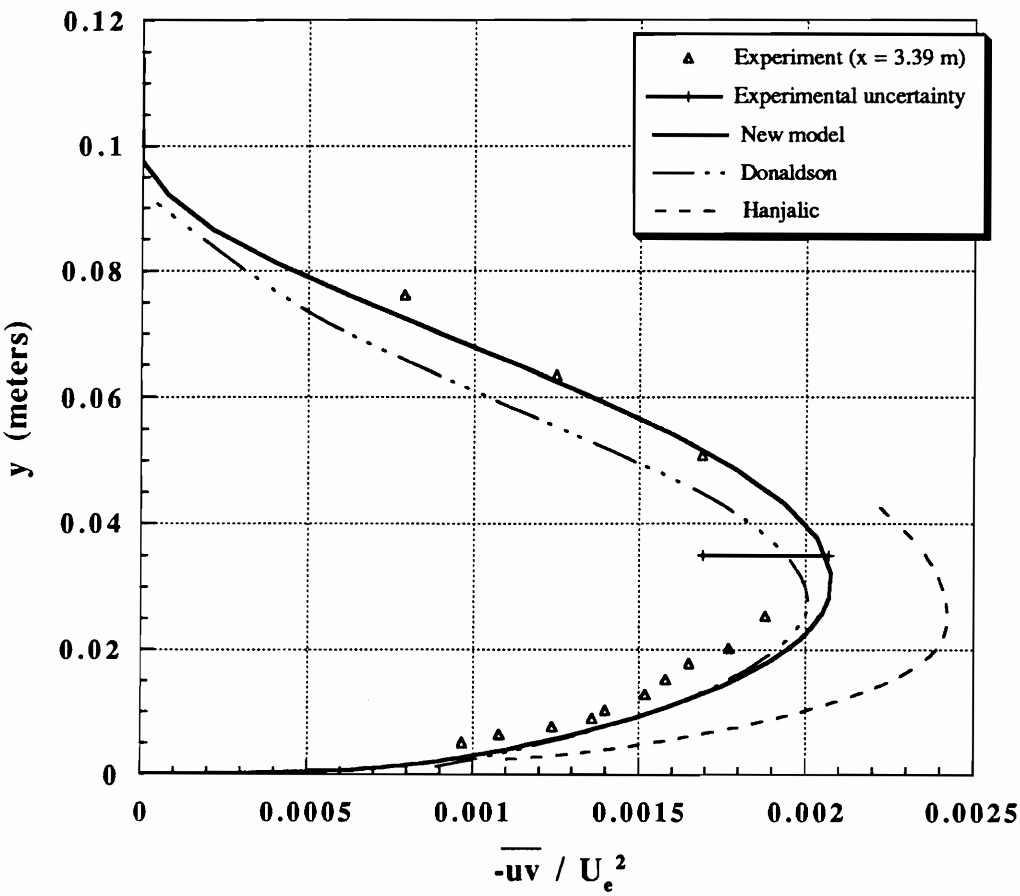

Figure 30. : Samuel and Joubert experiment. Stress profile at x = 3.39 (m). Comparison with other models.

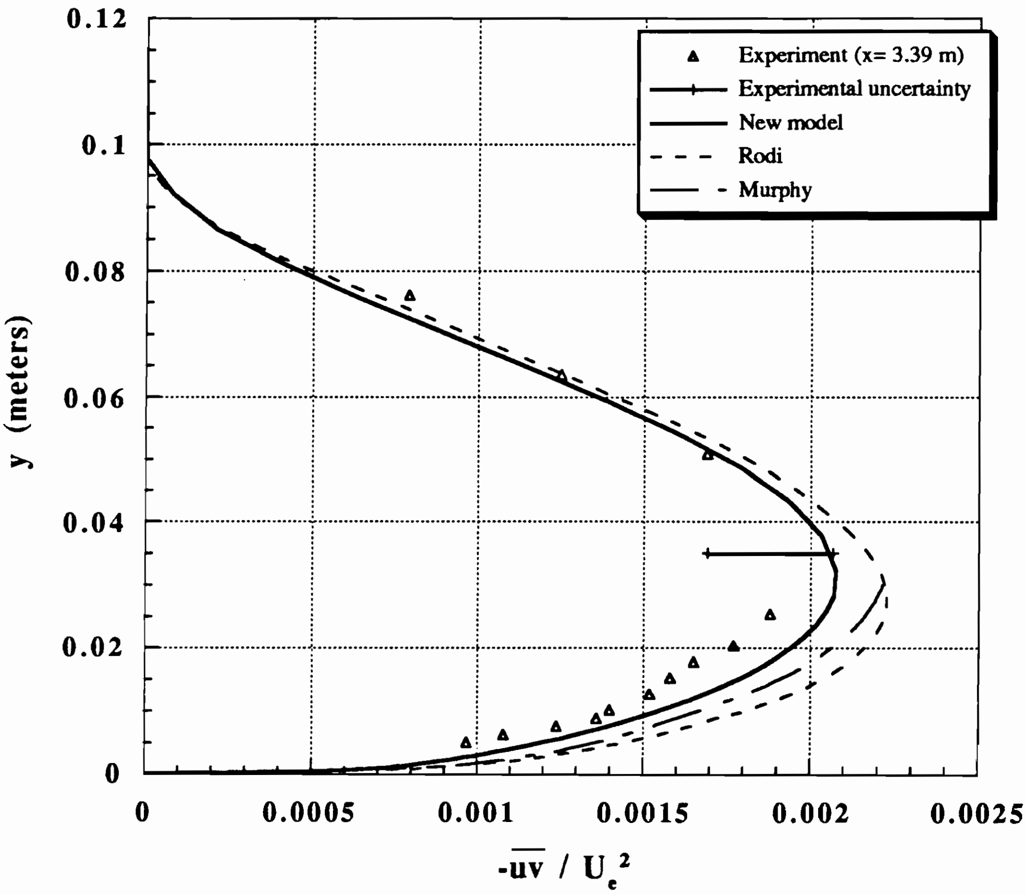

Figure 31. : Samuel and Joubert experiment. Stress profile at x = 3.39 (m). Comparison with other models.

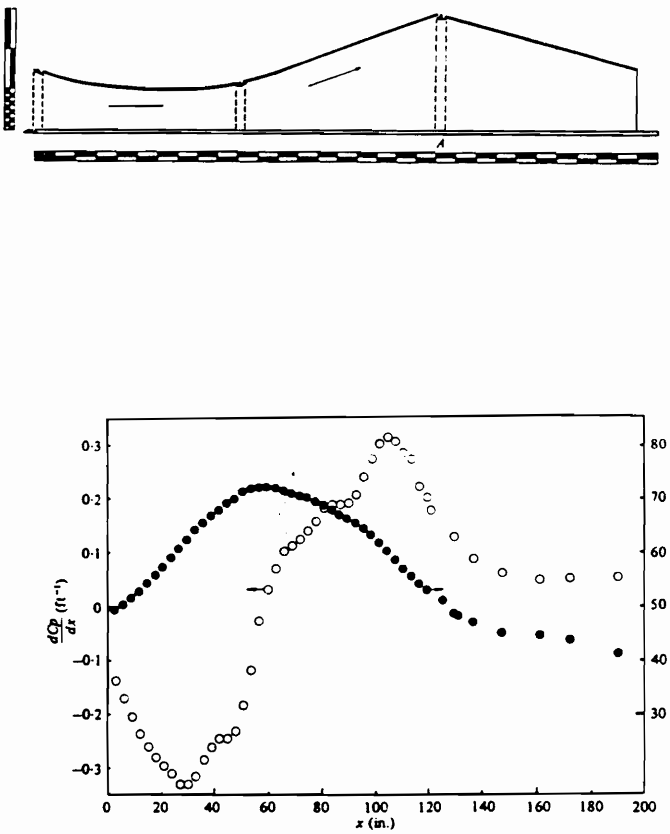

Figure 32. : Simpson, Chew, and Shivaprasad steady experiment. Freestream velocity and pressure gradient distributions.

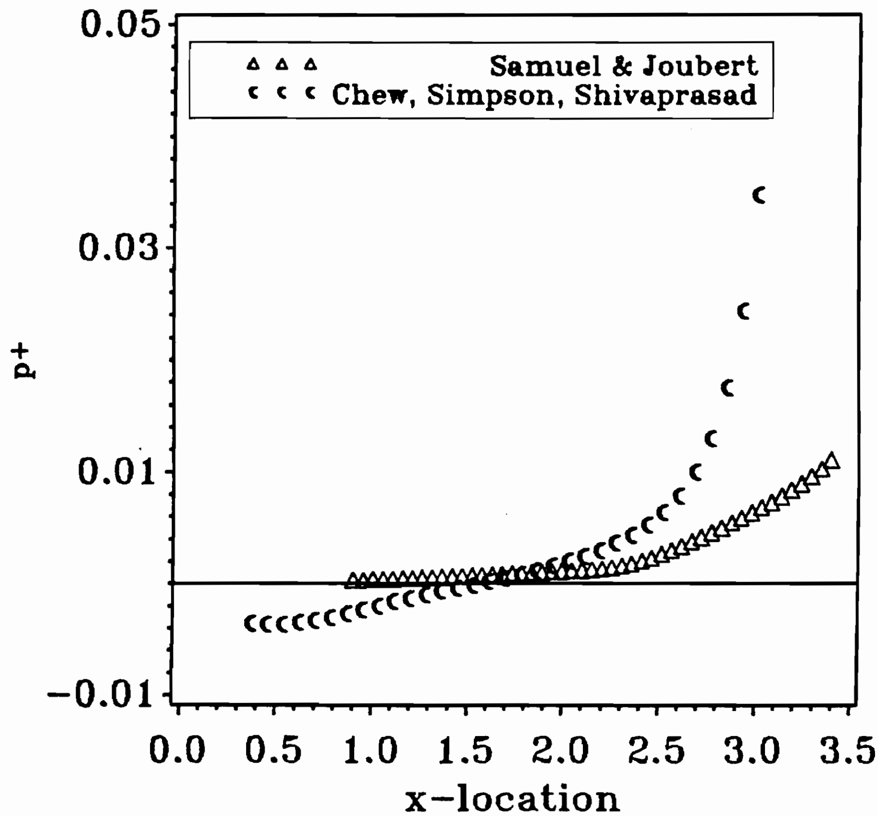

Figure 33. : p^+: Nondimensional pressure gradient for the Samuel-Joubert and Simpson-Chew-Shivaprasad experiments.

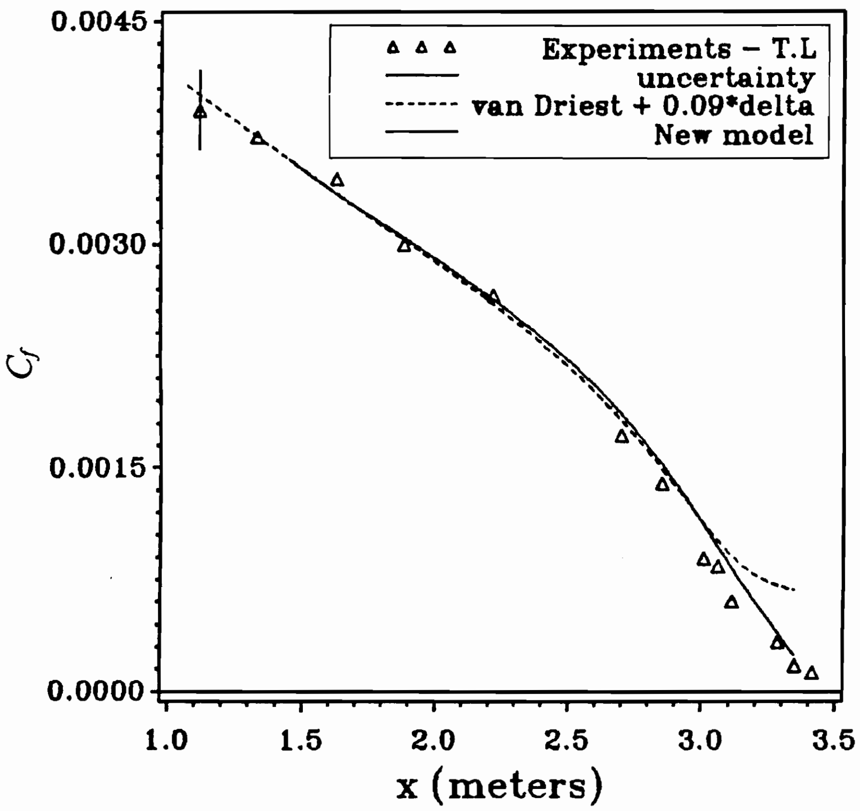

Figure 34. : Simpson, Chew, and Shivaprasad steady experiment. Skin friction coefficient.

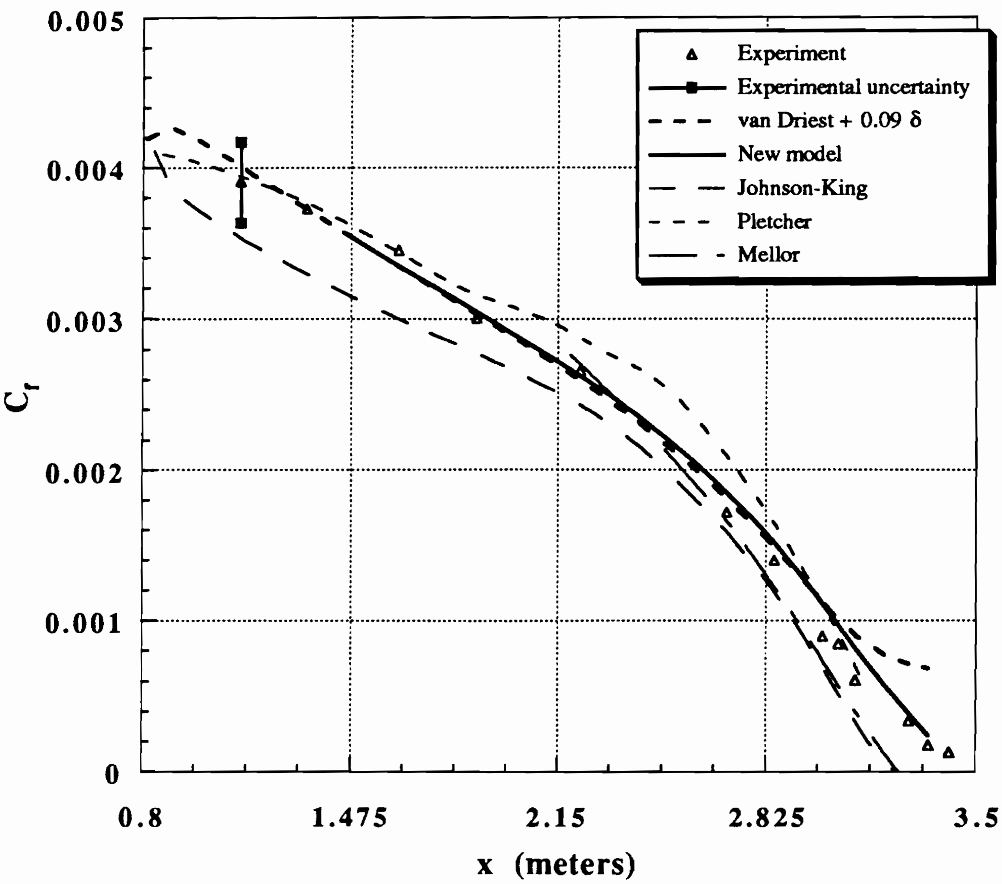

Figure 35. : Simpson, Chew, and Shivaprasad steady experiment. Skin friction coefficient. Comparison with other models.

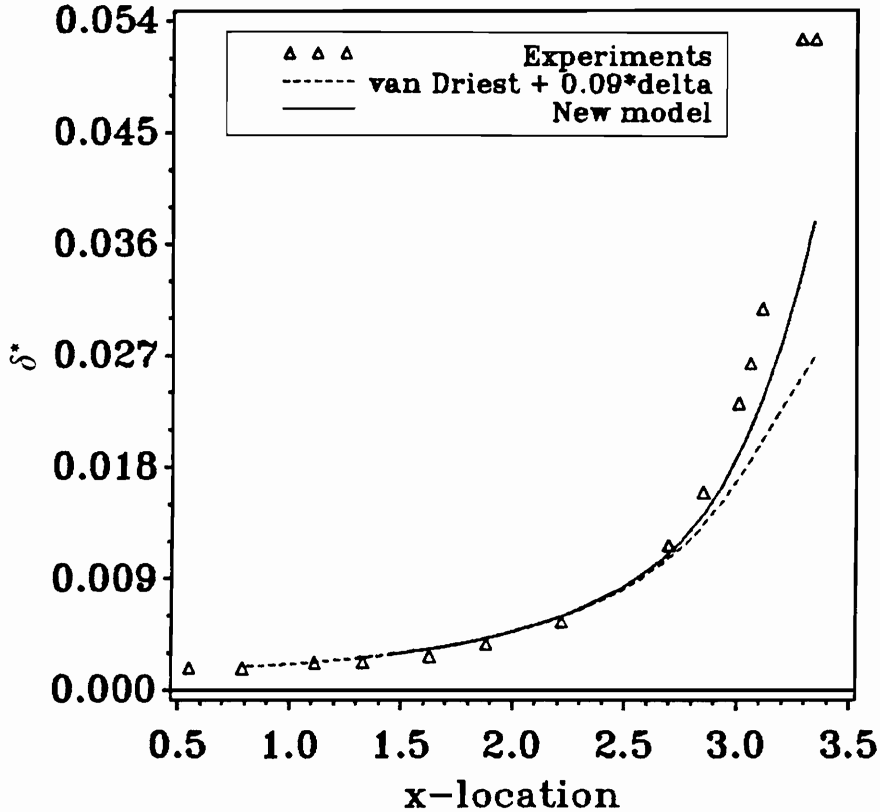

Figure 36. : Simpson, Chew, and Shivaprasad steady experiment. Displacement thickness.

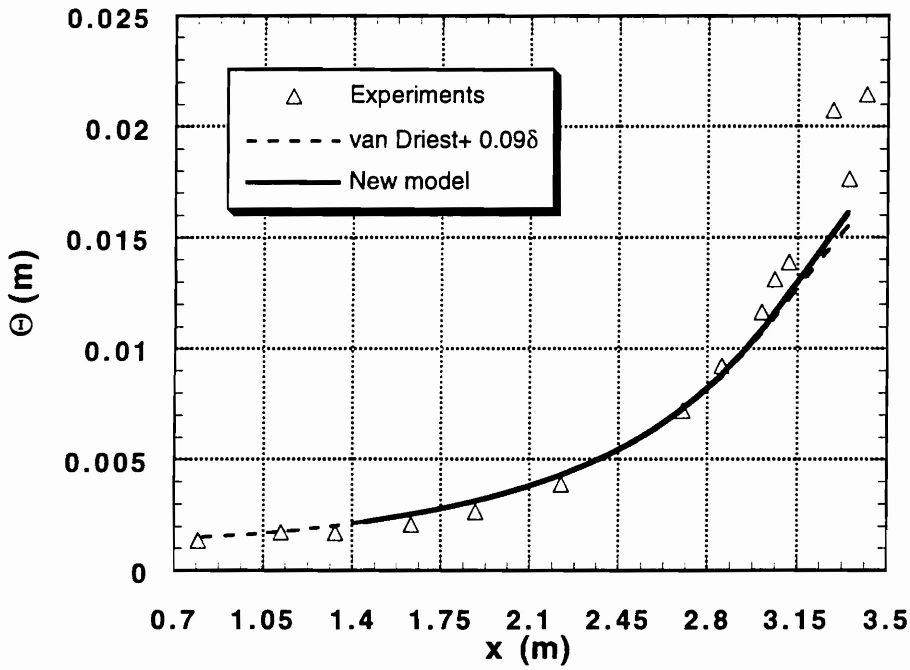

Figure 37. : Simpson, Chew, and Shivaprasad steady experiment. Momentum thickness.

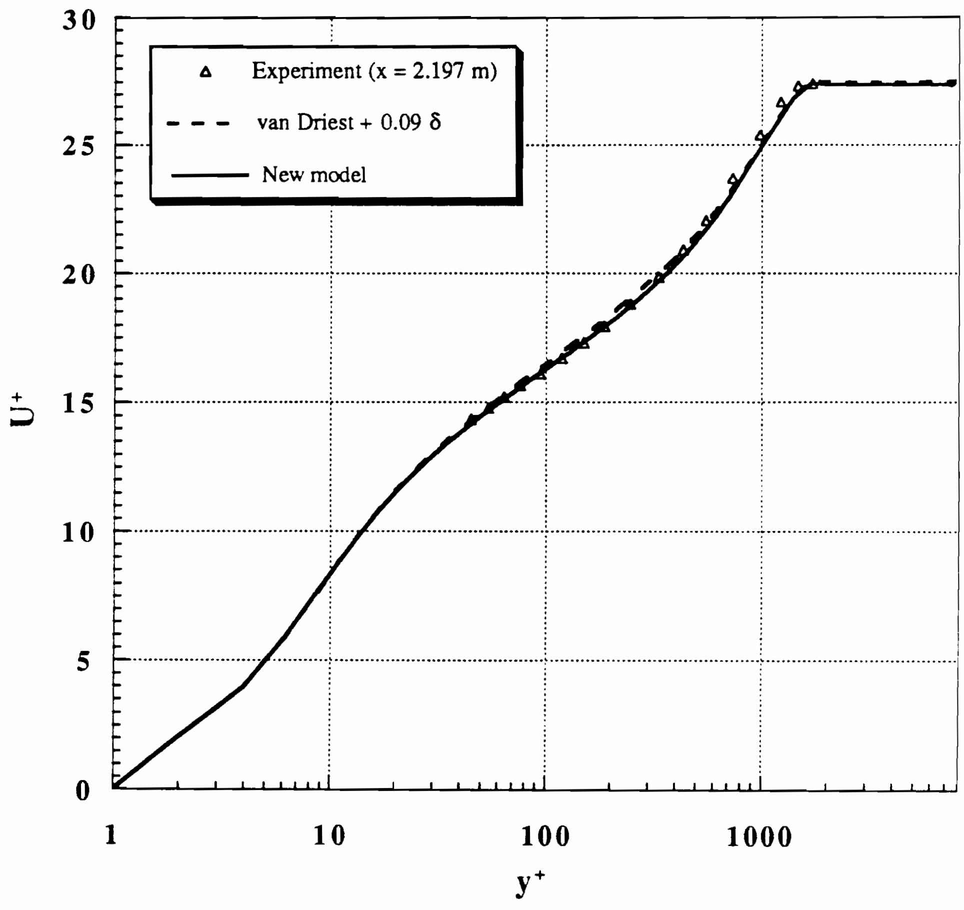

Figure 38. : Simpson, Chew, and Shivaprasad steady experiment. Velocity profile at x = 2.197 (m). Semilogarithmic plot.

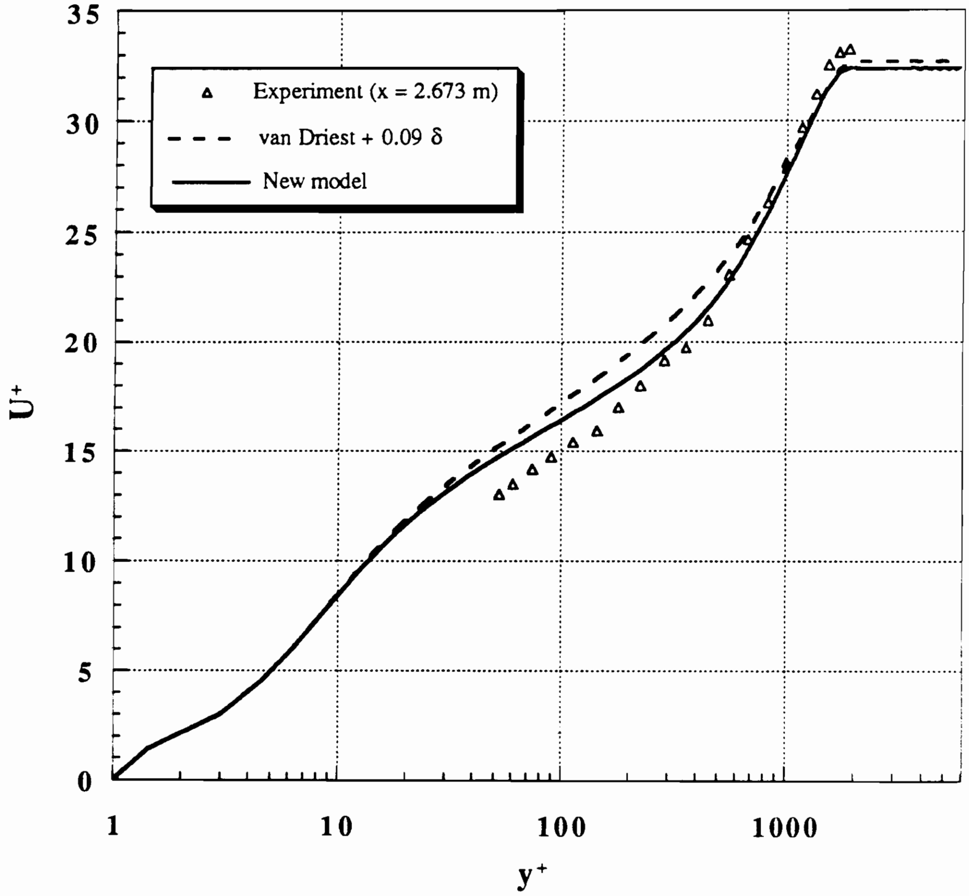

Figure 39. : Simpson, Chew, and Shivaprasad steady experiment. Velocity profile at x = 2.673 (m). Semilogarithmic plot.

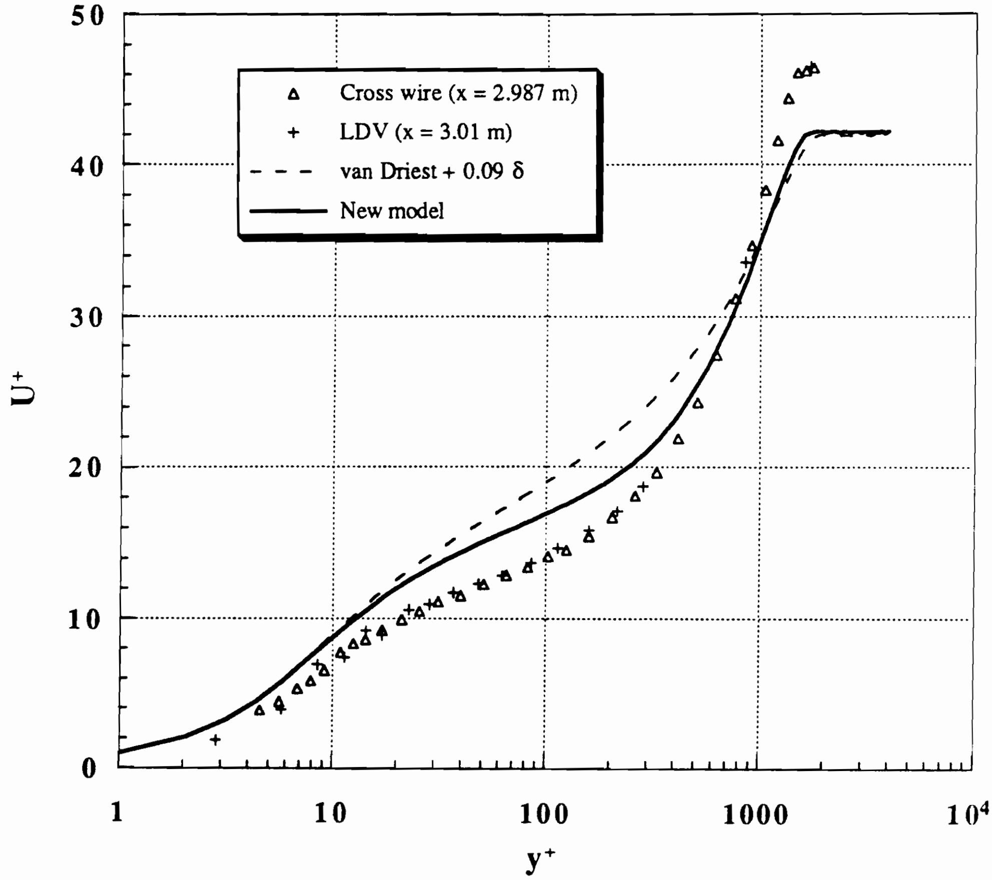

Figure 40. : Simpson, Chew, and Shivaprasad steady experiment. Velocity profile at x = 2.987 (m). Semilogarithmic plot.

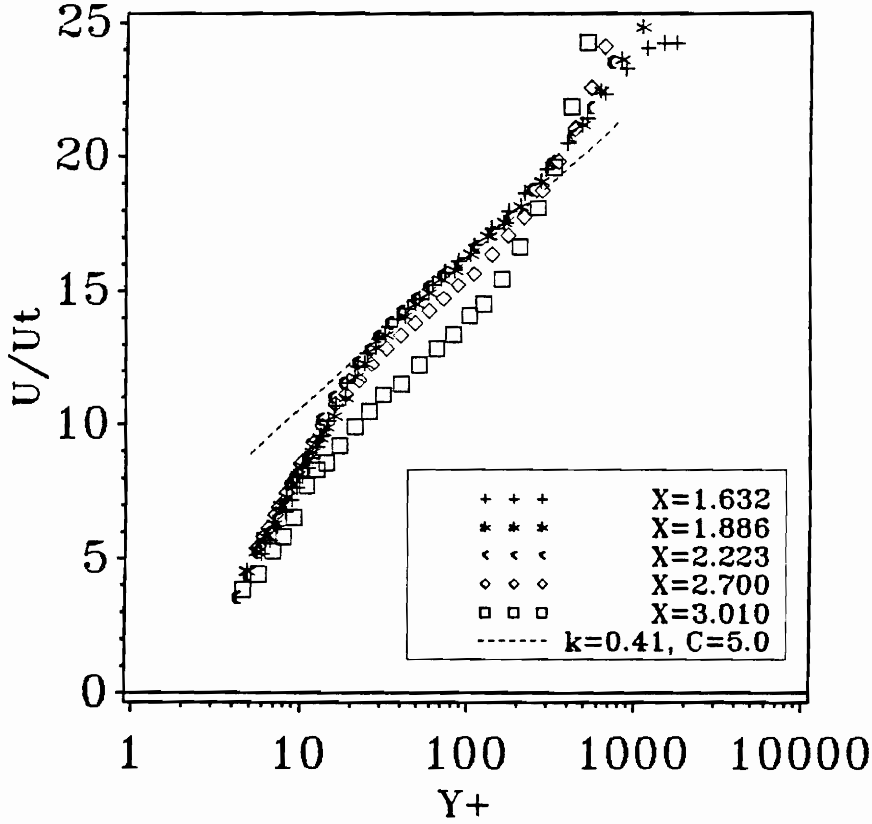

Figure 41. : Simpson, Chew, and Shivaprasad steady experiment. Experimental profiles in semilogarithmic coordinates.

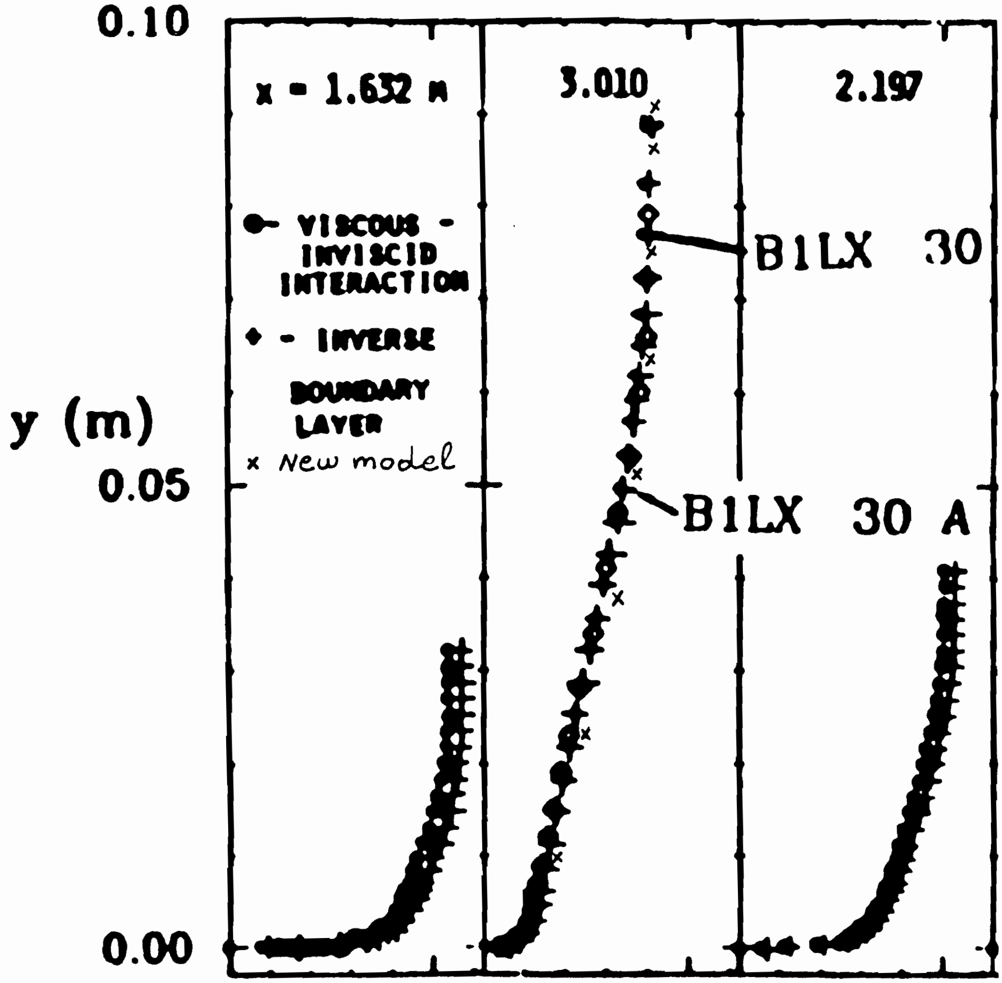

Figure 42. : Simpson, Chew, and Shivaprasad steady experiment. Velocity profile at x = 3.01 (m). Comparison with the results of Pletcher *et al* model. Taken from [31].

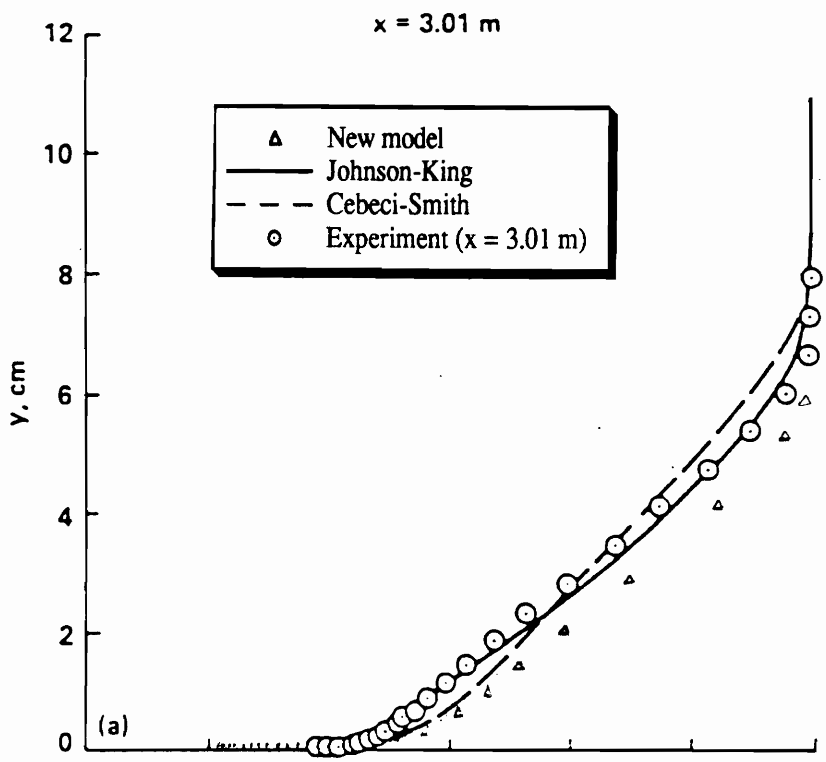

Figure 43. : Simpson, Chew, and Shivaprasad steady experiment. Velocity profile at x = 3.01 (m). Comparison with the results of Johnson-King model. Taken from [20].

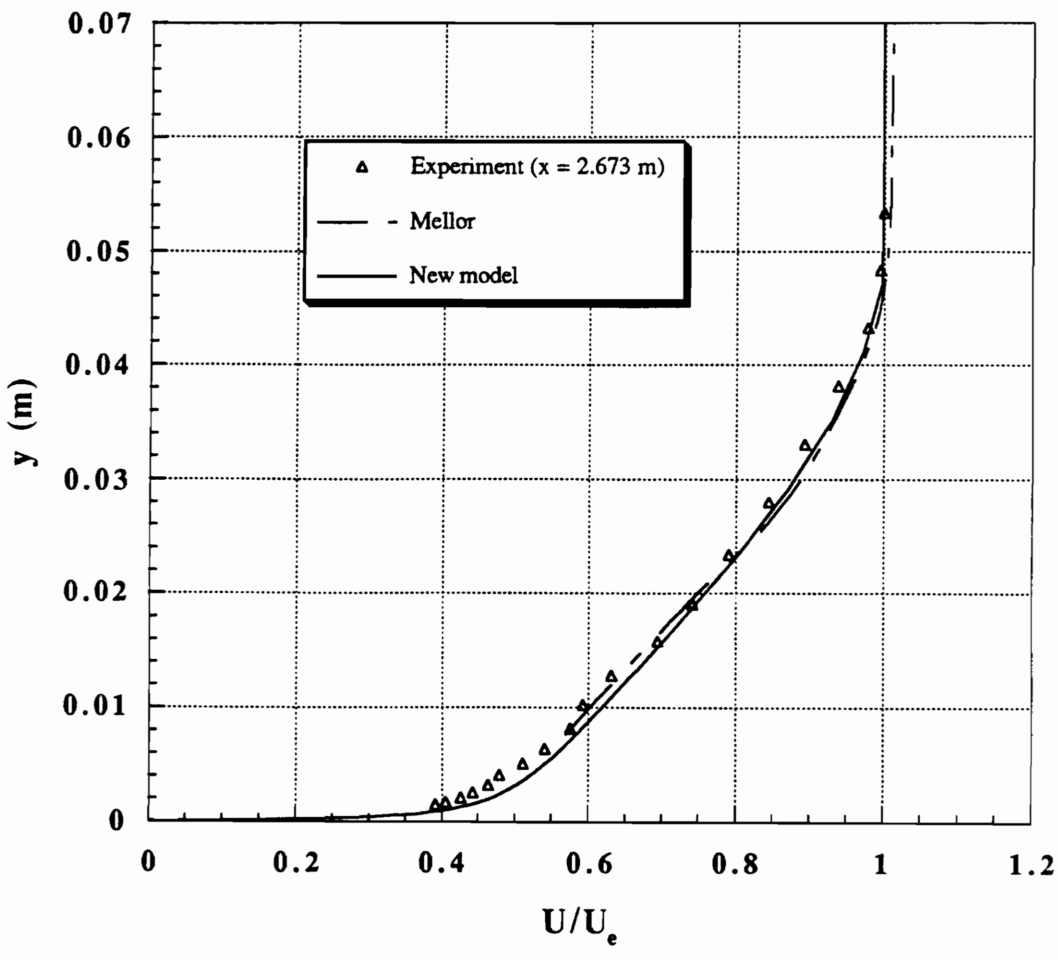

Figure 44. : Simpson, Chew, and Shivaprasad steady experiment. Velocity profile at x = 2.673 (m). Comparison with the results of Mellor model. Taken from [31].

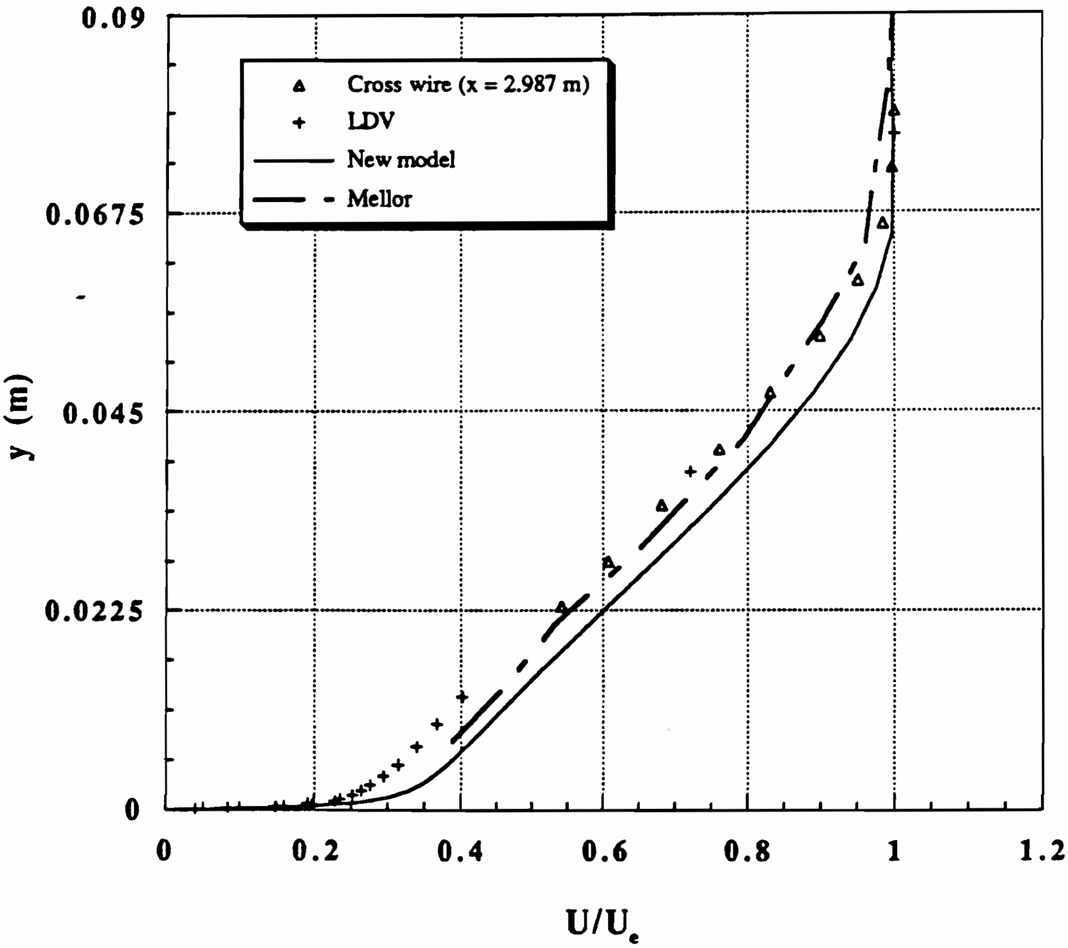

Figure 45. : Simpson, Chew, and Shivaprasad steady experiment. Velocity profile at x = 2.987 (m). Comparison with the results of Mellor model. Taken from [31].

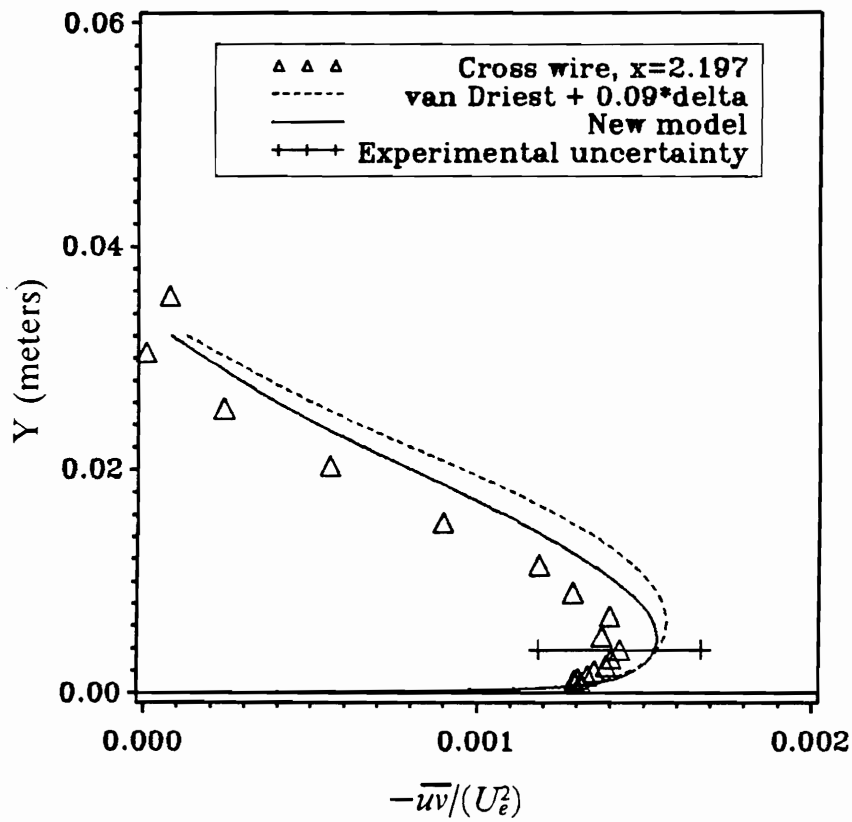

Figure 46. : Simpson, Chew, and Shivaprasad steady experiment. Stress profile at x = 2.197 (m).

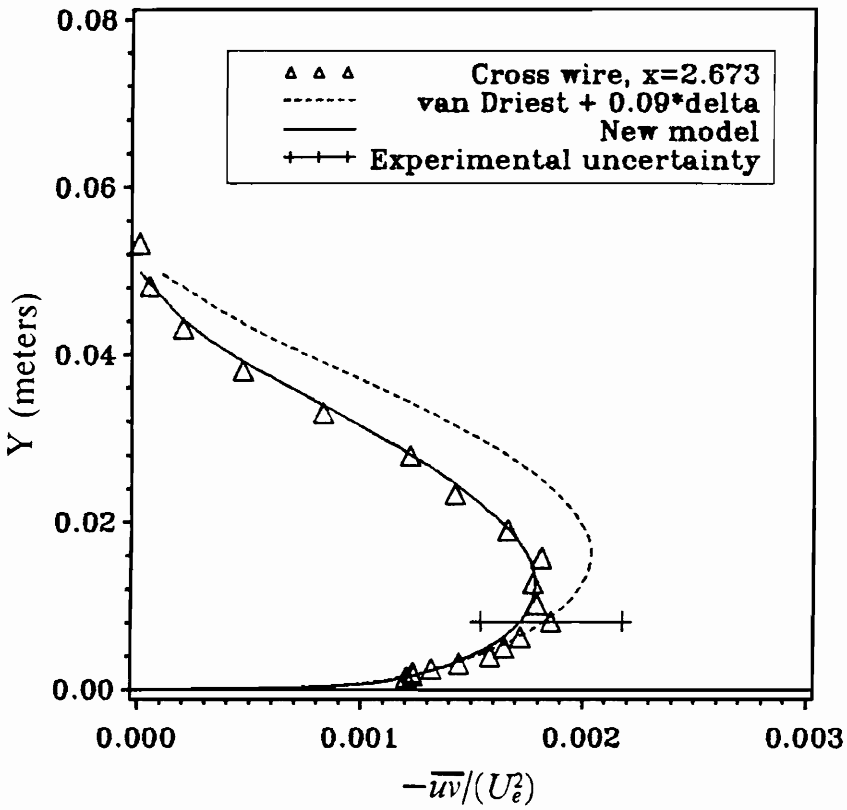

Figure 47. : Simpson, Chew, and Shivaprasad steady experiment. Stress profile at x = 2.673 (m).

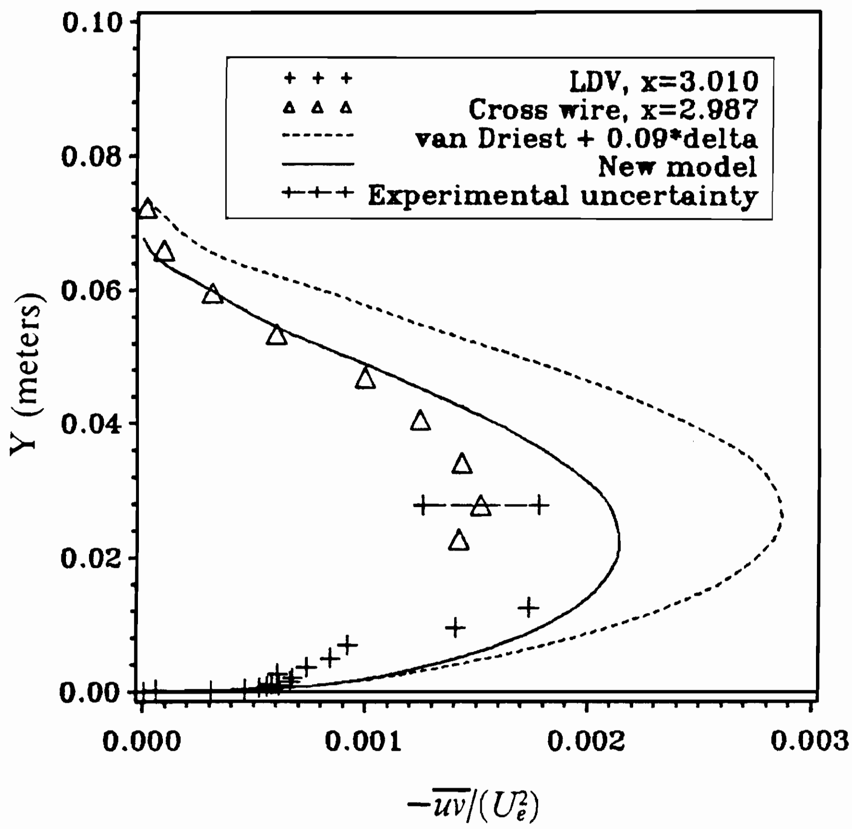

Figure 48. : Simpson, Chew, and Shivaprasad steady experiment. Stress profile at x = 3.010 (m).

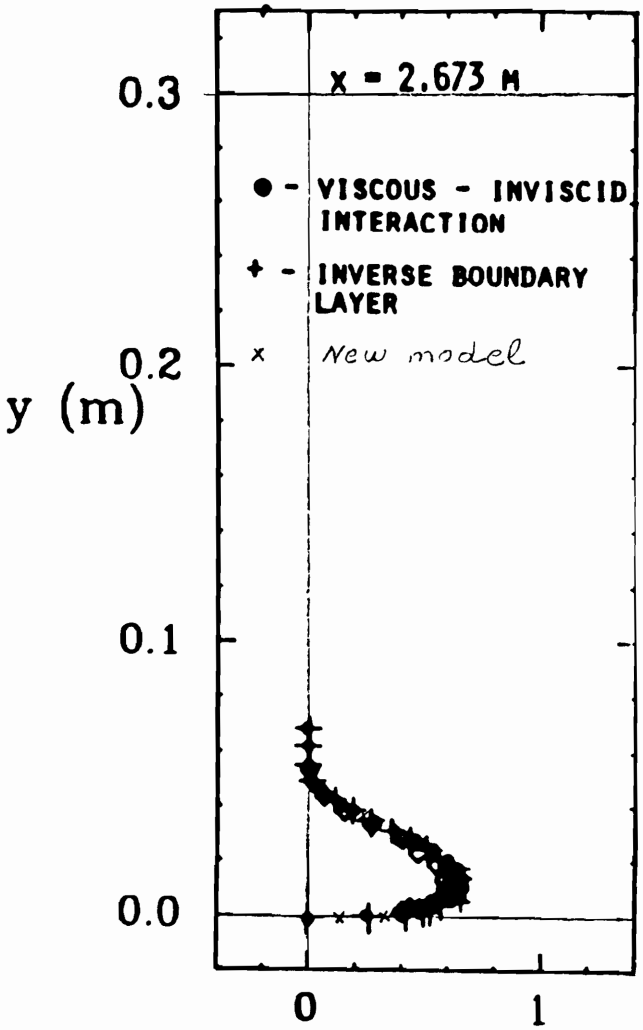

Figure 49. : Simpson, Chew, and Shivaprasad steady experiment. Stress profile at x = 2.673 (m). Comparison with the results of Pletcher *et al* model. Taken from [31].

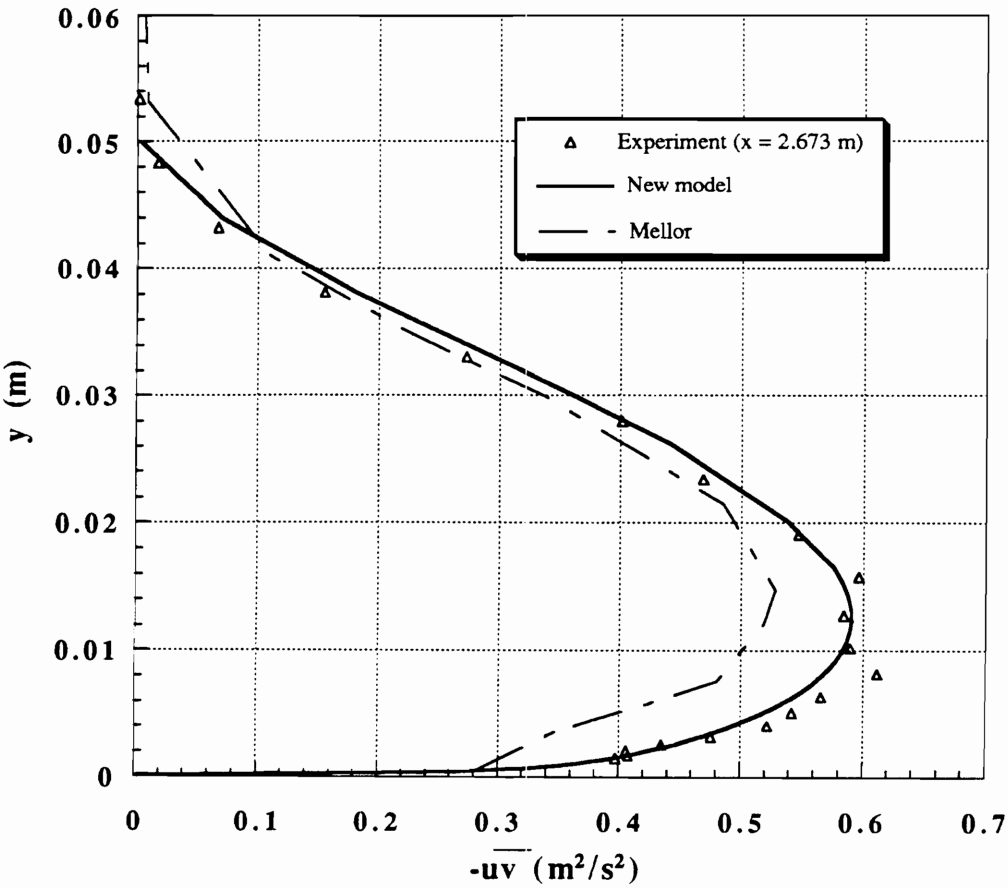

Figure 50. : Simpson, Chew, and Shivaprasad steady experiment. Stress profile at x = 2.673 (m). Comparison with the results of Mellor *et al* model. Taken from [31].

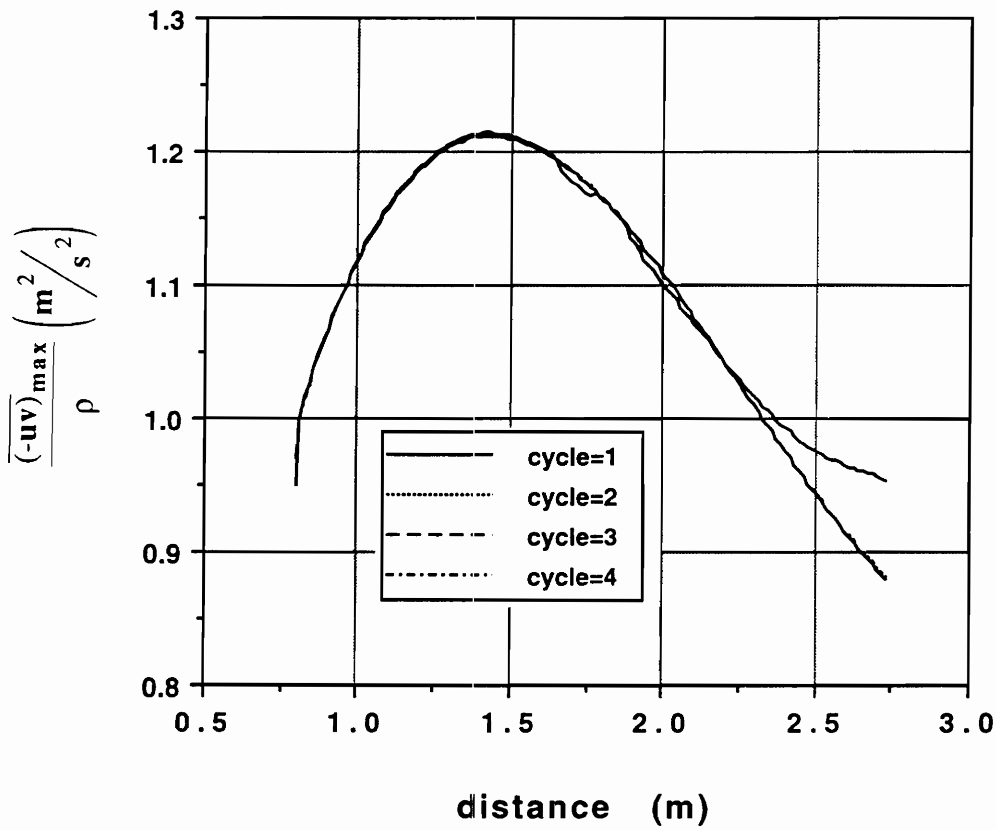

Figure 51. : Simpson, Shivaprasad, and Chew unsteady experiment. Maximum shear stress at ωt = 196 degrees. Convergence to a periodic solution. U(freestream) = max.

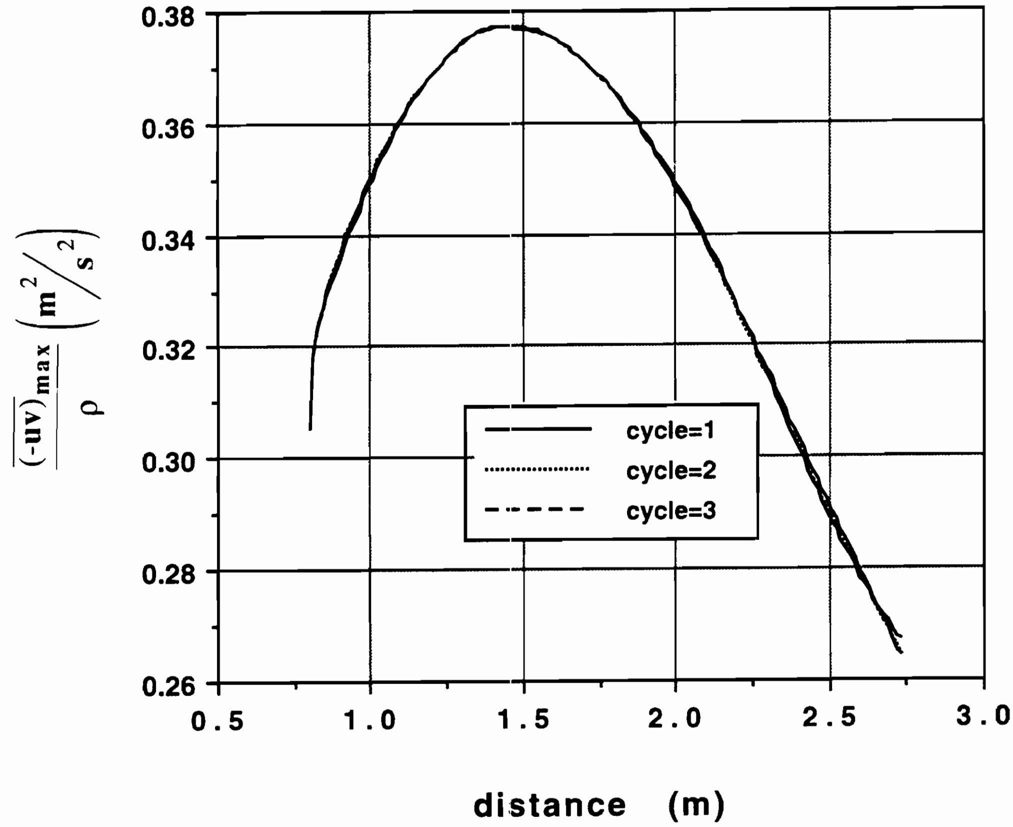

Figure 52. : Simpson, Shivaprasad, and Chew unsteady experiment. Maximum shear stress at ωt = 16 degrees. Convergence to a periodic solution. U(freestream) = min.

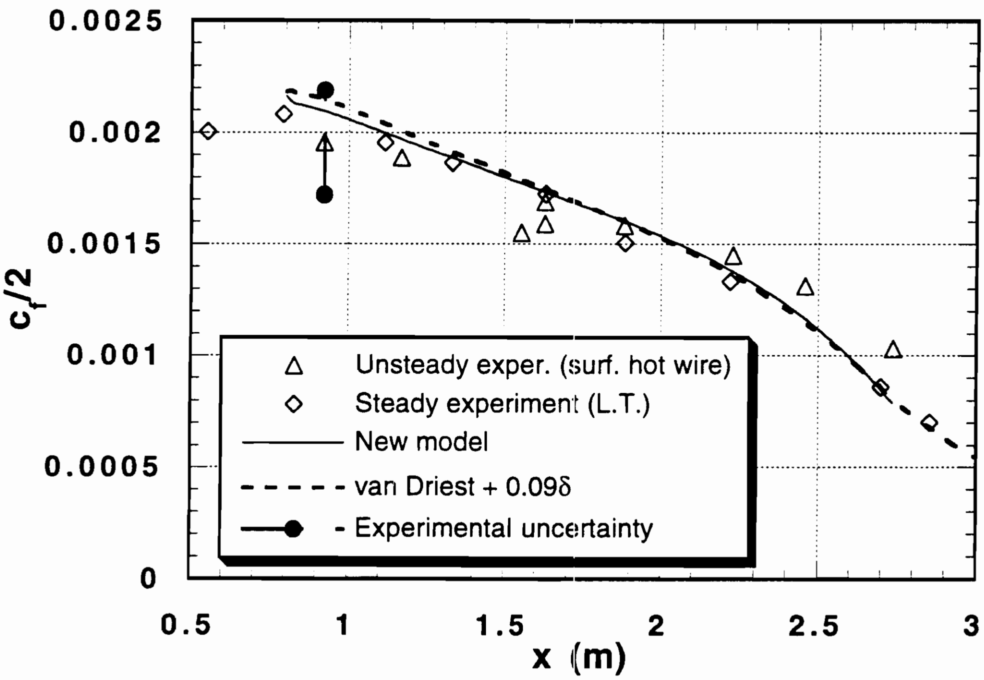

Figure 53. : Simpson, Shivaprasad, and Chew unsteady experiment. Time average skin friction coefficient.

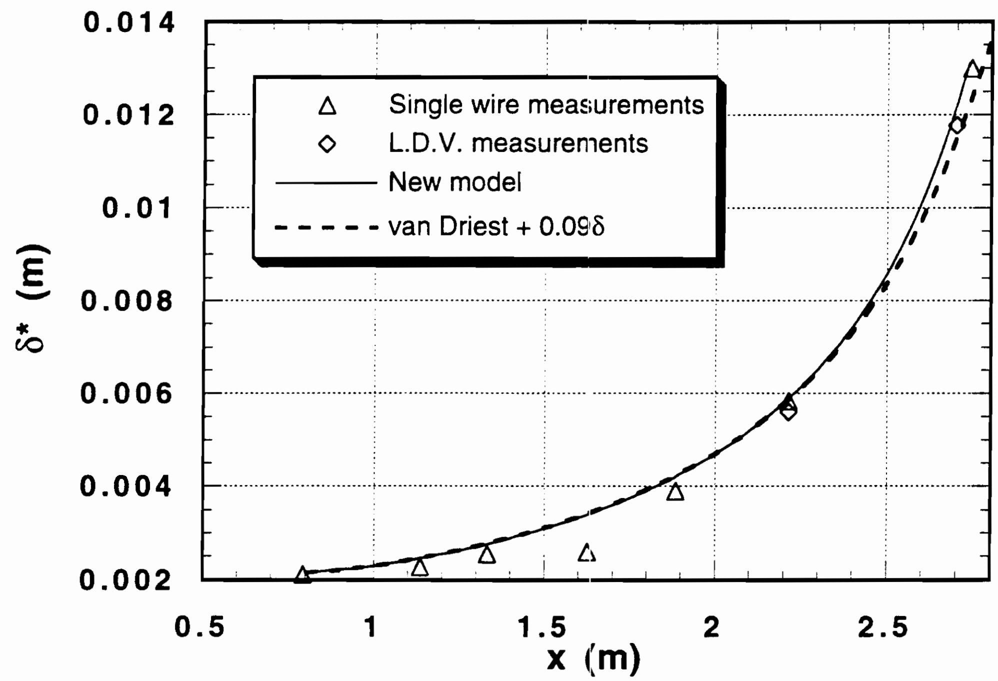

Figure 54. : Simpson, Shivaprasad, and Chew unsteady experiment. Time average displacement thickness.

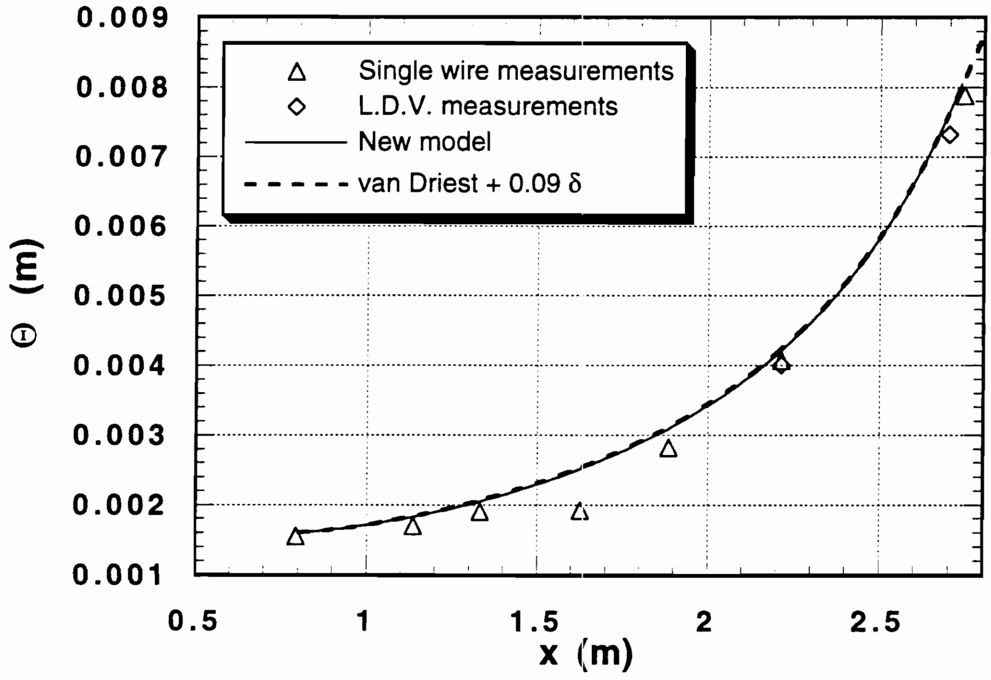

Figure 55. : Simpson, Shivaprasad, and Chew unsteady experiment. Time average momentum thickness.

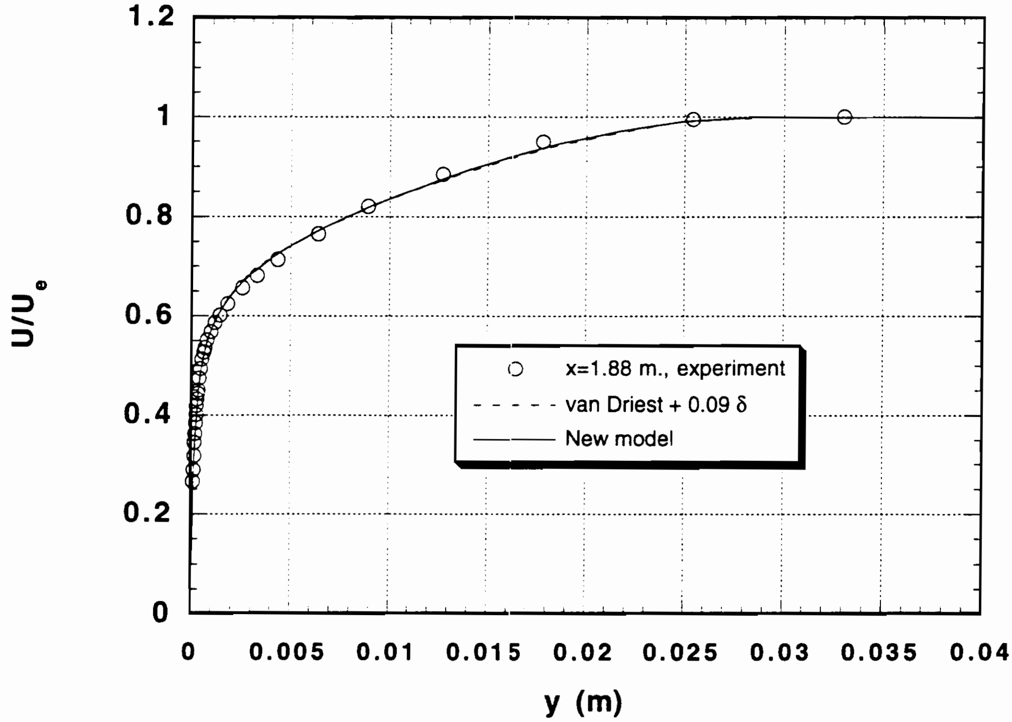

Figure 56. : Simpson, Shivaprasad, and Chew unsteady experiment. Time average velocity profile at x = 1.88 (m).

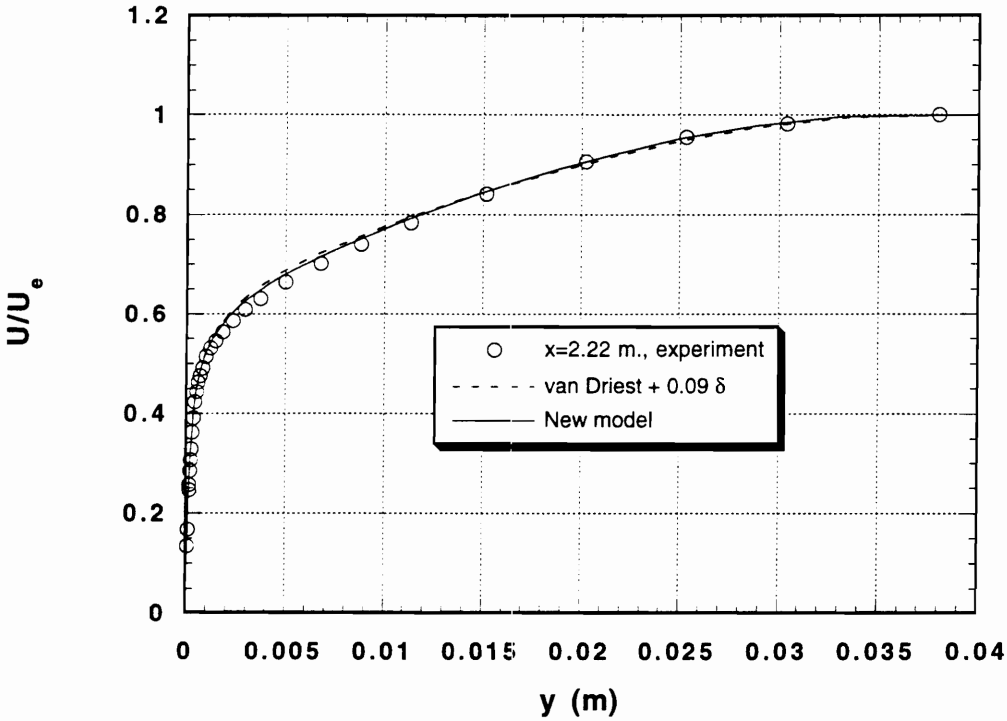

Figure 57. : Simpson, Shivaprasad, and Chew unsteady experiment. Time average velocity profile at x = 2.22 (m).

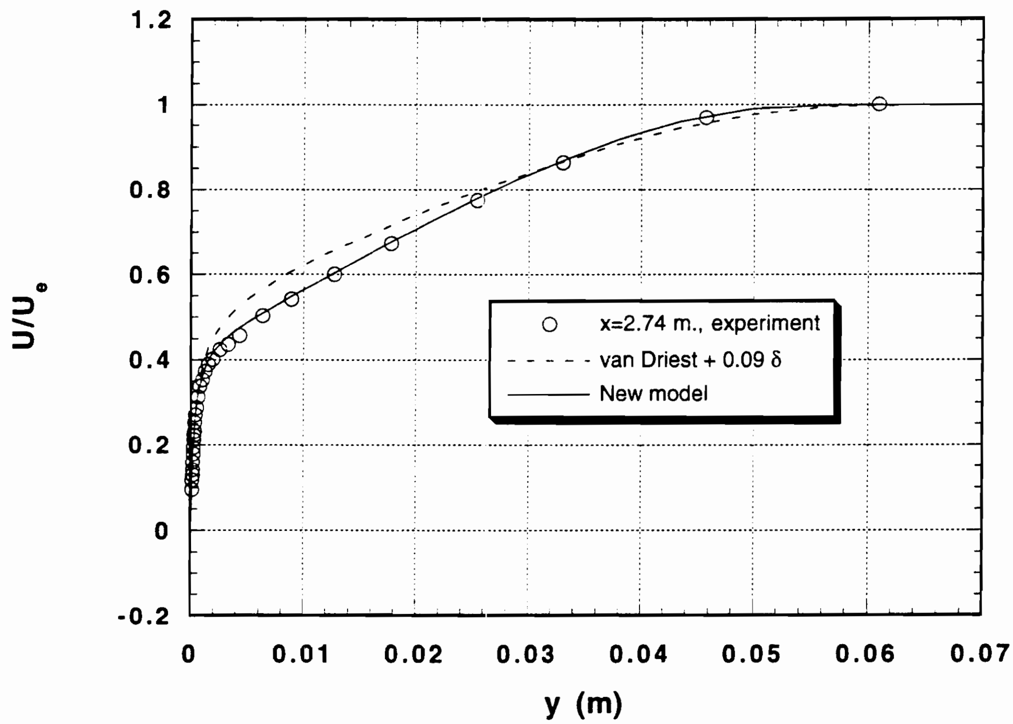

Figure 58. : Simpson, Shivaprasad, and Chew unsteady experiment. Time average velocity profile at x = 2.74 (m).

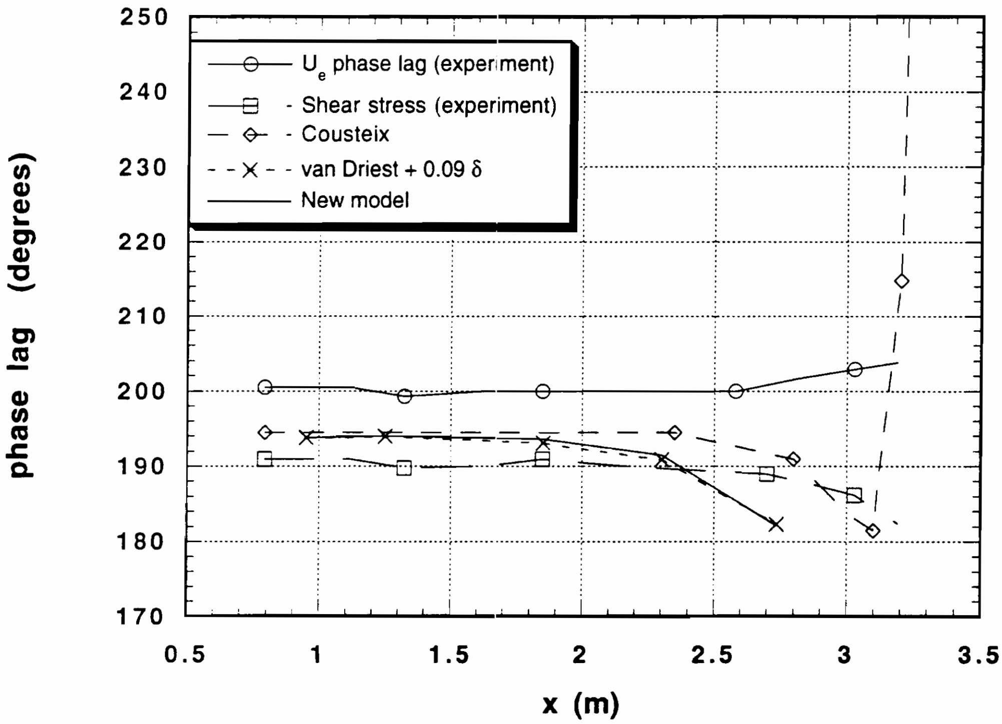

Figure 59. : Simpson, Shivaprasad, and Chew unsteady experiment. Phase lag of the wall shear with respect to the freestream velocity.

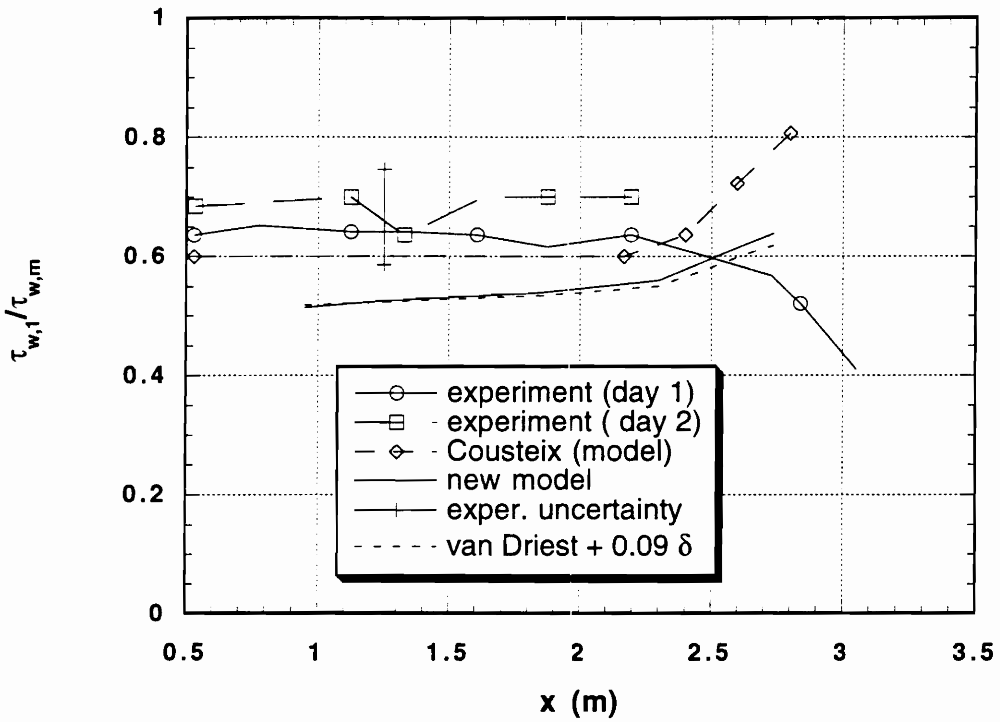

Figure 60. : Simpson, Shivaprasad, and Chew unsteady experiment. Wall shear stress. Ratio of the amplitude of the first harmonic to the time average value.

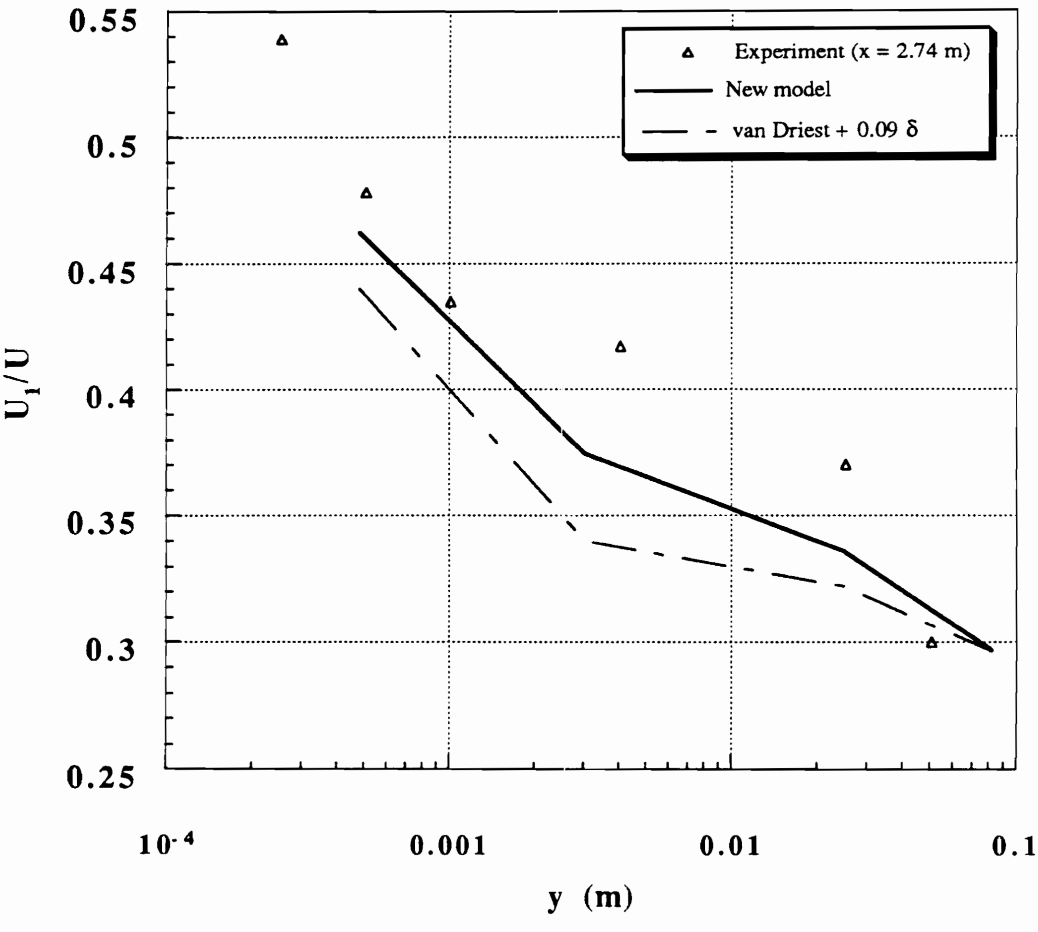

Figure 61. : Simpson, Shivaprasad, and Chew unsteady experiment. Ratio of the amplitude of the first harmonic of velocity to the time average value as a function of y.

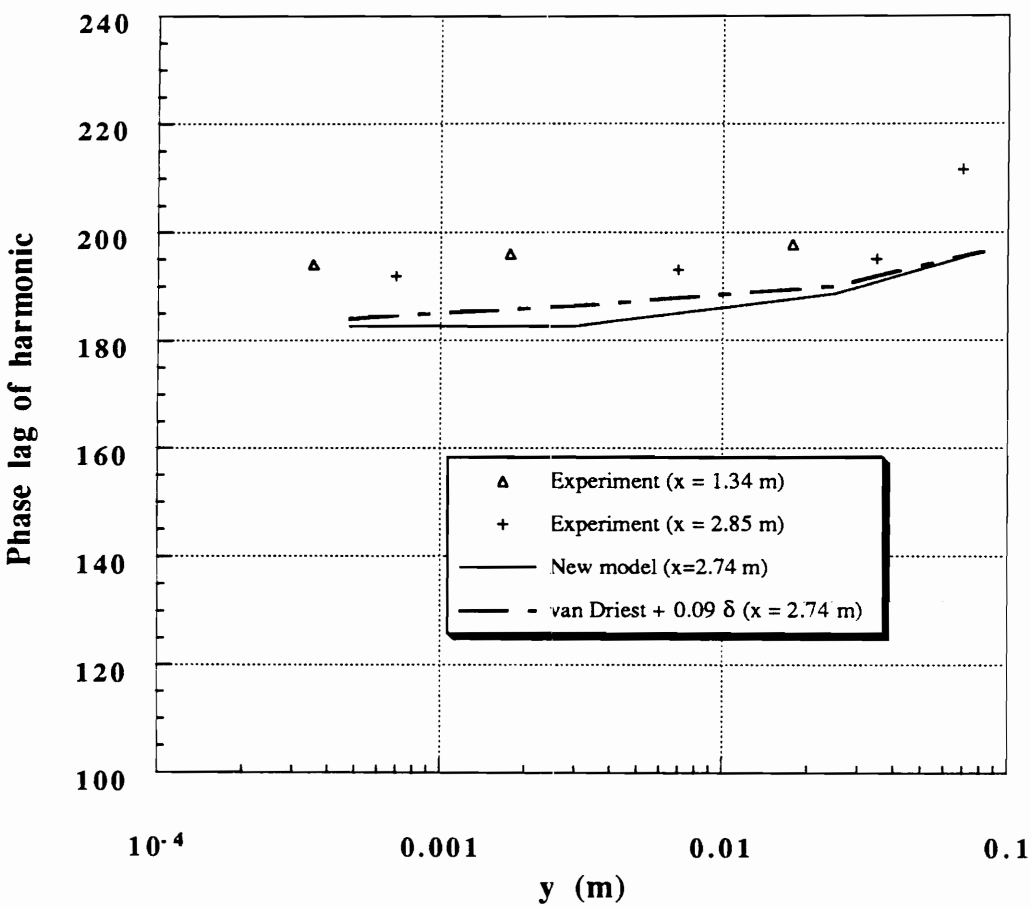

Figure 62. : Simpson, Shivaprasad, and Chew unsteady experiment. Phase angle of first harmonic of velocity as a function of distance from the wall.

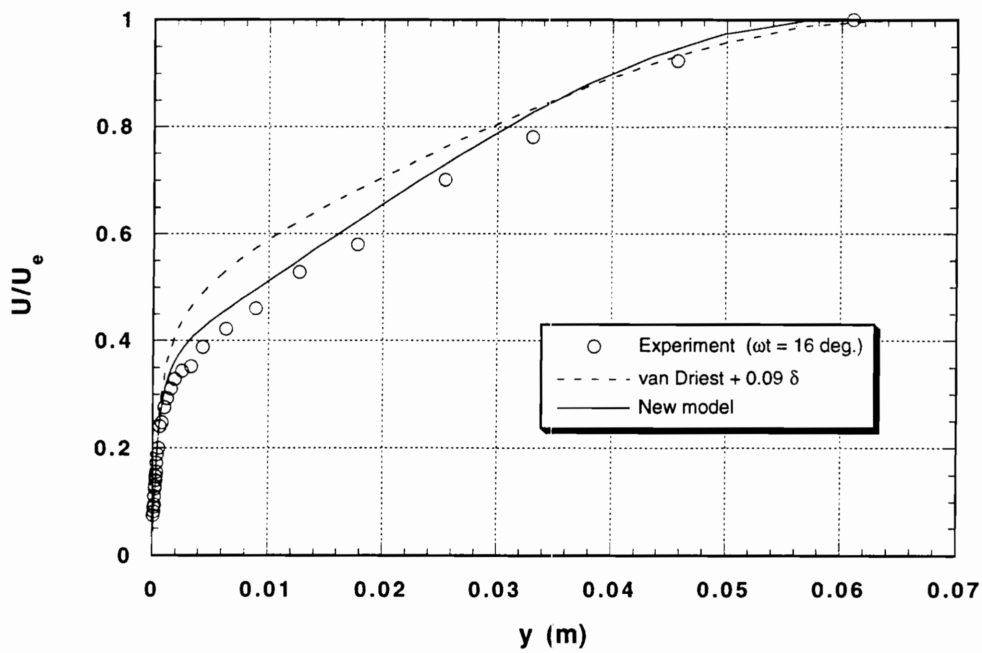

Figure 63. : Simpson, Shivaprasad, and Chew unsteady experiment. Phase average velocity profile at $x = 2.74$ (m). $\omega t = 16$ degrees, U(freestream) = minimum.

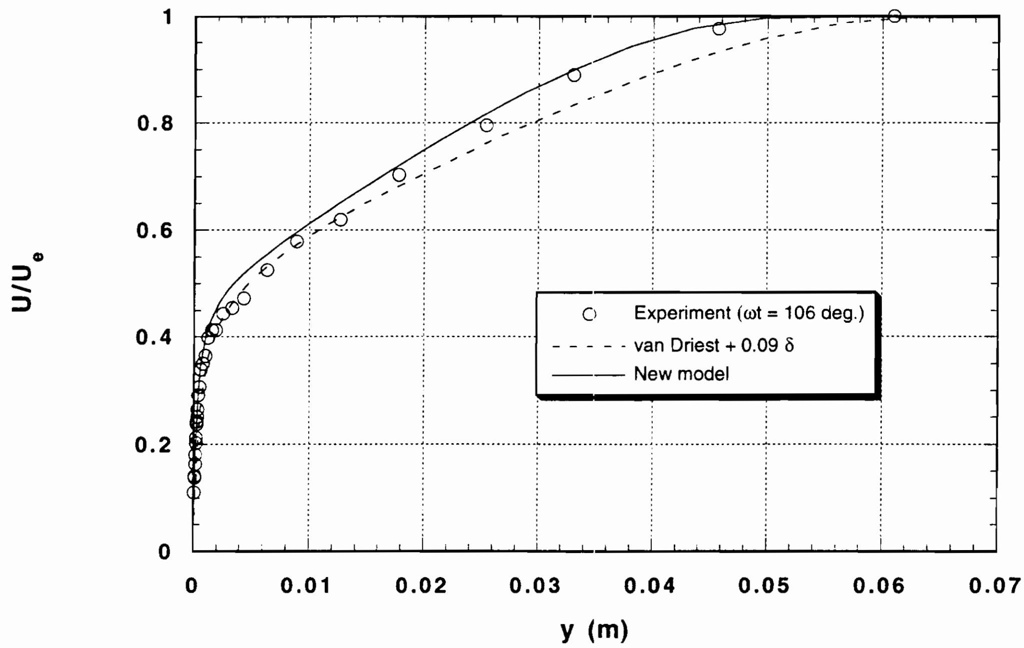

Figure 64. : Simpson, Shivaprasad, and Chew unsteady experiment. Phase average velocity profile at x = 2.74 (m). ωt = 106 degrees, U(freestream) = U(mean) and increasing.

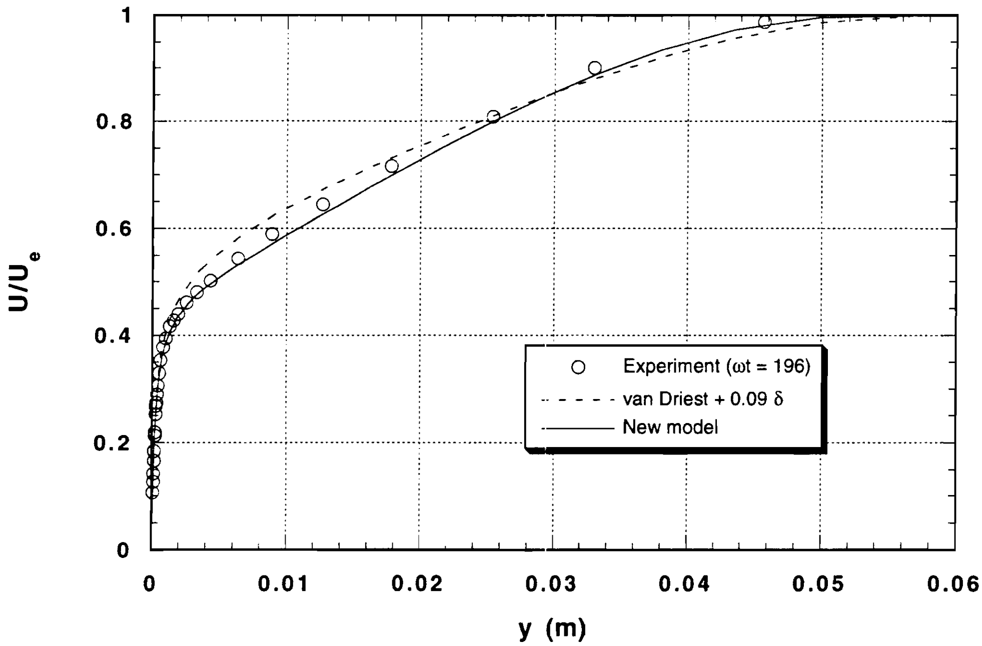

Figure 65. : Simpson, Shivaprasad, and Chew unsteady experiment. Phase average velocity profile at x = 2.74 (m). ωt = 196 degrees, U(freestream) = maximum.

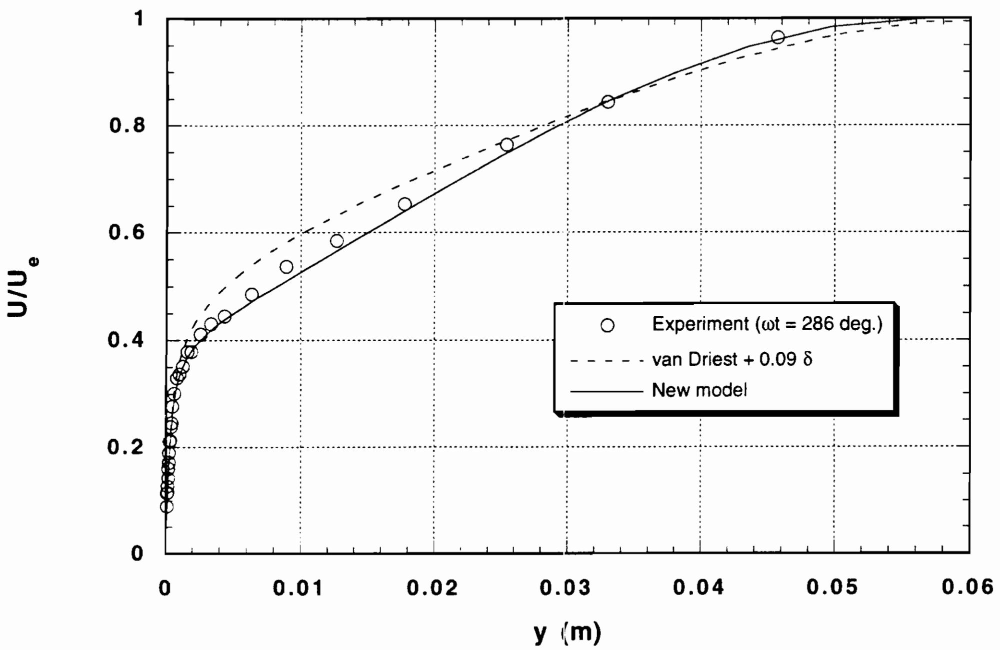

Figure 66. : Simpson, Shivaprasad, and Chew unsteady experiment. Phase average velocity profile at $x = 2.74$ (m). $\omega t = 286$ degrees, U(freestream) = U(mean) and decreasing.

References

[1] Rodi, W., *Turbulence Models and Their Application in Hydraulics - A State of the Art Review*, Second Edition, IAHR, Delft, The Netherlands, 1984.

[2] Lakshninarayana, B., "Three-dimensional turbulent boundary layers", *AIAA Journal*, Dec. 1986, pp. 1907-1917.

[3] Humphreys, D.A., and Lidhout, J.P.F., "Calculation methods for three-Dimensional turbulent boundary layers", *Progress in Aerospace Sciences,* Vol. 25, 1988, pp. 107-129.

[4] Schetz, Joseph A., *Boundary Layer Analysis*, Prentice-Hall Inc., Englewood Cliffs, 1993.

[5] Anderson, D.A., Tannehill, J.C., and Pletcher, R.H., *Computational Fluid Mechanics and Heat Transfer,*, Hemisphere Publishing Corporation, New York, 1984.

[6] Prandtl, L., "Über die ausgebildete Turbulenz" [On Fully-Developed Turbulence], ZAMM., Vol. 5, pp. 136-139 (1925).

[7] Deardorff, J.W. (1970) "A Numerical Study of Three-Dimensional Turbulent Channel Flow at Large Reynolds Numbers," *J. Fluid Mech.,* vol. 41, pp. 453-480.

[8] Schmitt, L., Richter, K., and Friedrich, R., "Large-Eddy Simulation of Turbulent Boundary Layer and Channel Flow at High Reynolds number," in U. Schyumann and R. Friedrich (eds.), *Direct and Large Eddy Simulation of Turbulence,* (Notes on Numerical Fluid Mechanics, Vol. 15 Vieweg, Braunschweig (1986)).

[9] Spalart, P.R., " Direct simulation of a turbulent boundary layer up to $Re_\theta = 1410.$," *J. Fluid Mech.,* vol. 187, 61-98, 1988.

[10] Spalart, P.R., Watmuff, J.H., "Experimental and Numerical study of a turbulent boundary layer with pressure gradients", *J. Fluid Mech.*, vol. 249, pp. 337-371, 1993.

[11] Clauser, F.H., "The Turbulent Boundary Layer," in *Advances in Applied Mechanics,*, Vol. IV, Academic press, New York, 1956.

[12] Cebeci, T., and Smith, A.M.O., *Analysis of turbulent boundary layers*, Academic Press, New York, 1974.

[13] Baldwin, B., and Lomax, H., "Thin-Layer Approximation and Algebraic Model for Separated Turbulent Flows," AIAA paper No. 78-257 (1978).

[14] Taylor, G. I., "The Transport of Vorticity and Heat through Fluids in Turbulent Motion.," Appendix by A. Fage and V. M. Falkner, Proc. R. Soc. Lond., Vol. A135, pp. 685-705 (1932).

[15] Prandtl, L., "Uber eine neues Formelsystem fur die ausgelbidete Turbulenz" [On a New Formulation for Fully Developed Turbulence], *Nachr. Akad. Wiss., Gottingen, Math. Phys. Klasse.,* pp. 6-19 (1945).

[16] Kolmogorov, A.N., "Equations of turbulent motion of an incompressible fluid," Izv. Akad. Nauk. SSR, Seria fizicheska Vi., No. 1-2, pp. 56-58 (1942) (English translation: Imperial College, Mech. Eng. Dept. Rept. ON/6, (1968)).

[17] Launder, B.E., and Spalding, D.B., (1974), "The Numerical Computation of Turbulent Flows," *Comput. Methods Appl. Mech Eng.*, Vol. 3, pp. 269-289.

[18] Bradshaw, P., Ferris D.H., and Atwell N.P., "Calculation of boundary-layer development using the turbulent energy equation," *J. Fluid Mech.*, (1967), vol. 28, part 3, pp. 593-616.

[19] McDonald , H., and Camarata, F.J., "An extended mixing length approach for computing the turbulent boundary layer development," in *Computation of Turbulent Boundary Layers, Proc. of the AFOSR-IFP-Stanford conference,* Stanford U., Aug. 18-25, 1968.

[20] Johnson, D. A., and King, L.S., "A new Turbulence Closure Model for Boundary Layer Flows with Strong Adverse Pressure Gradients and Separation", AIAA paper 84-0175, 1984.

[21] Menter, F. R., "Performance of Popular Turbulence Models for Attached and Separated Adverse Pressure Gradient Flows," AIAA-91-1784 (1991).

[22] Perry, A. E., and Schofield, W. H., "Mean velocity and Shear Stress Distributions in Turbulent Boundary Layers", Physics of Fluids, Vol. 16, No. 12, Dec. 1973, pp. 2068-2081.

[23] Townsend, A. A., *The Structure of Turbulent Shear Flow* , Cambridge University Press, Cambridge, Great Britain, 1976.

[24] Simpson, R.L., "A Review of Two-Dimensional Turbulent Separated Flow Calculation Methods," in F. T. Smith (ed.), *Boundary Layer Separation,* Springer-Verlag, Heidelberg (1987).

[25] Dindar, M., and Kaynak, U., "Effect of Turbulence Modeling on Dynamic Stall of a NACA0012 Airfoil," AIAA 92-0027, 30th Aerospace Sciences Meeting & Exhibit, January 6-9, Reno, NV.

[26] Srinivasan, G.R., Ekaterinaris, J.A., and McCroskey, W.J., "Dynamic Stall of an Oscillating Wing. Part 1: Evaluation of Turbulence Models," AIAA 93-3403, AIAA 11th Applied Aerodynamics Conference, August 9-11, 1993, Monterey, CA.

[27] Yakhot, V. and Orzag, S.A., "Renormalization Group Analysis of Turbulence. 1-Basic Theory," Journal of Scientific Computing, Vol. 1, 1986.

[28] Baldwin, B.S., and Barth, T.J., "A one-equation Turbulence Transport Model for High Reynolds Number Wall-Bounded Flows," AIAA 91-0610, January 1991; also NASA TM-102847, August 1990.

[29] Spalart, P. R., and Allmaras, S.R., "A One-Equation Turbulence Model for Aerodynamic Flows," AIAA 92-0439, January 1992.

[30] Goldberg, P., "Upstream History and Apparent Stress in Turbulent Boundary Layers," Gas Turbine Laboratory, Report No. 85, M.I.T. (1966).

[31] Kline, S.J., Cantwell, B.J., and Lilley, G.M., *1980-81 AFOSR-HTTM-Stanford Conference on Complex Turbulent Flows,* Stanford University, Ca, 1981.

[32] Saffman, P. G., and Wilcox, D. C., "Turbulence-Model Predictions for Turbulent Boundary Layers", AIAA J., Vol. 12, No. 4, 1974, pp. 541-546.

[33] Wilcox, D. C., and Traci, R. M., "A Complete Model of Turbulence" , AIAA Paper 76-351.

[34] Menter, F.R., "Zonal Two Equation K - ω Turbulence Models for Aerodynamic Flows,"24th Fluid Dynamics Conference, July 6-9, 1993, Orlando, FL.

[35] Speziale, G.S., Abid, R., and Anderson, E.C., "A critical evaluation of Two-Equation Models for Near Wall Turbulence," AIAA 90-1481, AIAA

21st Fluid Dynamics, Plasma Dynamics and Lasers Conference, June 18-20, 1990, Seattle, WA.

[36] Wilcox, D., "A Two-Equation Turbulence Model for Wall-Bounded and Free-Shear Flows," 24th AIAA Fluid Dynamics Conference, July 6-9, 1993, Orlando, FL.

[37] Speziale, C. G.,"Analytical methods for the development of Reynolds-stress closures in turbulence", Annual Review of Fluid Mechanics, vol. 23, 1991, pg. 107-157.

[38] Donaldson, C. Dup., "A computer study of an analytical model for boundary-layer transition", *AIAA J.*, vol. 7, 1969, pp. 271-278.

[39] Daly, B.J., and Harlow, F.H., "Transport equations in turbulence," J. Phys. Fluids, vol. 13, no. 11, November 1970, pp. 2634-2649.

[40] Hanjalic K., and Launder, B.E., "A Reynolds stress model of turbulence and its applications to thin shear flows", *J. Fluid Mechanics*, vol. 52, 1972, pp. 609-638.

[41] Launder, B. E., Reece, G. J., and Rodi, W., "Progress in the development of a Reynolds-stress turbulence closure", *J. Fluid Mech,*

vol. 68, pp. 537-566, 1975.

[42] Hytopoulos, E., and Simpson, R.L., "Critical Evaluation of Recent Second-Order Closure Models," AIAA 93-0081, 31st AIAA Aerospace Sciences Meeting & Exhibit, January 11-14, 1993, Reno, NV.

[43] Abid, R., and Schmitt, R., "Critical Examination of Turbulence Models for a Separated Three Dimensional Turbulent Boundary Layer", Rech. Aerosp., No 1984-6.

[44] Gatski, T.B., and Speziale, C.G., "On explicit Algebraic Stress Models for Complex Turbulent Flows", ICASE Report No. 92-58, November, 1992.

[45] Piomelli, U., Moin, P., and Ferziger, J. H., "Model consistency in large eddy simulation of turbulent channel flows," Phys. Fluids **31** (7), July 1988.

[46] Ragab, A. S., Personal communication.

[47] Speziale, C. G., "Galilean invariance of the subgrid-scale stress models in the large-eddy simulation of turbulence," *Fluid Mech,* Vol. 156, pp. 55-62.

[48] Hussaini, M. Y., Speziale, C. G., and Zang, T. A., "The Potential and Limitations of Direct and Large-Eddy Simulations", Whither Turbulence? Tur-

bulence at the Crossroads, Proceedings, Ithaca, New York, 1989, Lecture Notes in Physics, Vol. 357, Springer-Verlag.

[49] Moin, P., and Jimenez, J., "Large Eddy Simulation of Complex Turbulent Flows", AIAA 24th Fluid Dynamics Conference, July 6-9, 1993, Orlando, FL.

[50] Simpson, R.L., "Two-dimensional turbulent separated flow," AGARDograph No. 287, Vol. 1, (1985).

[51] Ragab, S., Lecture notes

[52] Launder B.E., and Spalding D.B., *Lectures in Mathematical Models of Turbulence*, Academic Press, 1972.

[53] Bradshaw, P., "The turbulence structure of Equilibrium Boundary Layers," *J. Fluid Mech.,* Vol. 29, pp. 625-645, 1967.

[54] Shiloh, K., Shivaprasad, B.G., and Simpson, R.L., "The structure of a separating turbulent boundary layer. Part 3. Transverse velocity measurements," *J. Fluid Mech.* (1981), Vol. 113, pp. 75-90.

[55] Simpson, R.L., Strickland, J.H., and Barr, P.W., "Features of a separating turbulent boundary layer in the vicinity of separation," *J. Fluid Mechanics,* vol. 79, part 3, pp. 553-594.

[56] Collins, M.A., and Simpson, R.L., "Flow-field prediction of separating turbulent shear layers," *AIAA J.,* Vol. 16, pp. 291-292, 1978.

[57] So, R.M.C., Zhang, H.S., and Speziale C.G., "Near-wall Modeling of the Dissipation-Rate Equation," *30th Aerospace Sciences Meeting and Exhibit,* January 6-9, 1992, Reno, NV.

[58] Wolfstein, M., "Convection processes in turbulent impinging jets," Imperial College, Heat Transfer Section Rep SF/R/2.

[59] Johnson, D.A. and Coakley, T.J., "Improvements to a Nonequilibrium Algebraic Turbulence Model," *AIAA J.*, vol. 28, No 11, 1990.

[60] Ludwieg, H., and Tillman, W., "Investigation of the Wall Shearing Stress in Turbulent Boundary Layers," *NACA TM 1285* (1950).

[61] McDonald, H., "The effect of Pressure Gradient on the Law of the Wall in Turbulent Flow," *J. Fluid Mech.,* Vol. 35, pp. 311-336 (1969).

[62] Spalart, P., and Watmuff, J.H., "Experimental and numerical study of a turbulent boundary layer with pressure gradients," *J. Fluid Mechanics,* Vol. 249, pp. 337-371, 1993.

[63] Nagano, Y., Tagawa, M., and Tsuji, T., "Effects of adverse pressure gradients on mean flows and turbulence statistics in a boundary layer," Eighth Symposium on Turbulent Shear Flows, Technical University of Munich, September 9-11, 1991.

[64] Coles, D., "The Law of the Wall in Turbulent Shear Flow," in *50 Jahre Grenzsschichtforshung,* F. Vieweg & Sohn, Braunschweig, 1955.

[65] Schetz, J.A., Hytopoulos, E., Gunzburger, M., "Numerical solution of the Boundary Layer Equations using the Finite Element Method," *J. of Fluids in Engineering,* Vol. 114, No. 4, p. 504, 1993.

[66] Kincaid, D., Cheney, W., *Numerical Analysis,* Brooks/Cole Publishing Company,Pacific Grove, California.

[67] Samuel, A.E., and Joubert, P.N., "A boundary layer developing in a increasingly adverse pressure gradient", *J. Fluid Mech.,* Vol. 66, Part 3, pp. 481-505, 1974.

[68] Simpson, R., Chew, Y.-T., and Shivaprasad, B.G., "The structure of a separating turbulent boundary layer. Part 1. Mean flow and Reynolds stresses," *J. Fluid Mech.* (1981), vol.113, pp. 23-51.

[69] Simpson, R.L., Shivaprasad, B.G., and Chew, Y.-T.,"The structure of a separating turbulent boundary layer. Part 4. Effects of periodic free-stream unsteadiness," *J. Fluid Mech.,* Vol. 127, pp. 219-261, 1983.

[70] "Memorandum on Data Selection," Proceedings Computation of Turbulent Boundary Layers - 1968 AFOSR-IFP-Stanford conference, vol. II, pp. 47-54, compiled data. Editors: D.E Coles, and E.A. Hirst.

[71] IMSL MATH/LIBRARY, "FORTRAN subroutines for Mathematical applications", Users Manual, Version 2.0.

[72] Glushko, G.S., "Turbulent Boundary Layer on a flat plate in an incompressible fluid," NASA TT F-10080, (1966).

[73] Cousteix, J., Desopper, A. and Houdeville, R., In *Proc. Symp on Turbulent Shear Flow,* Pa. State Univ., 18-20.

[74] Cousteix, J., Houdeville, R., and Raynaud, M., 1979 In *Proc. 2nd Symp on Turbulent Shear Flow,* Imperial College, London, 2-4 July, pp. 6.12-6.17.

[75] Kays, W.M., "Heat transfer to the transpired boundary layer," ASME paper No. 71-HT-44.

[76] Barenblatt, G.I., "Scaling laws for fully developed turbulent shear flows. Part 1. Basic hypotheses and analysis.," *J. Fluid Mech.*, vol. 248, pp. 513-520, 1993.

[77] Barenblatt, G.I., and Prostokishin, V.M., "Scaling laws for fully developed turbulent shear flows. Part 2. Processing of experimental data." *J. Fluid Mech.,* vol. 248, pp. 513-520, 1993.

Appendix A.

NUMERICAL SOLUTION OF THE BOUNDARY LAYER EQUATIONS
USING THE
FINITE ELEMENT METHOD.

Introduction

The present work is concerned with the application of the concept of Finite Element Method (FEM) to the formulation and solution of the boundary-layer equations governing the flow of incompressible fluids in two dimensions. Traditionally, numerical solutions for this set of equations have been obtained using the Finite Difference Method (FDM) and integral methods [1]. In the finite-difference approach, the continuous problem domain is " discretized " so that dependent variables are considered to exist only at discrete points. The derivatives are approximated by difference quotients resulting in an algebraic representation of the partial differential equation (PDE). For the flowfields solved by an FDM method, the accuracy of the solution depends to a large extent on the grid resolution, and a high number of nodes can be required to accurately describe regions of large gradients. Integral methods require prescribed velocity profiles and empirical relations in addition to the basic conservation laws.

In FEM, the flow region is subdivided into a number of small regions called finite elements. The dependent variables are interpolated within each element by functions of compatible order. Using these approximations in the field equations, we introduce residuals or errors. The general method seeks to reduce these errors to zero in a weighted sense and thus, the partial differential equations describing the problem in the region as a whole are replaced by algebraic equations in each element. A description of the basic method can be found in [2].

The earliest attempts to treat the boundary layer equations with what might broadly called Finite Element method date back 30 years [3, 4, 5]. With the limited computer power available at that time, it was necessary to use very large " elements " of the order of one-half the boundary-layer thickness. To achieve acceptable accuracy with such large elements, one needs to use very good basis or trial functions. The functions chosen were developed from solutions of the linearized version of the boundary layer equations for the problem of interest. These functions were then distorted by adding factors to the argument of the solutions. The values of these stretching factors were found by enforcing the simplest type of variational constraint, namely Collocation (i.e., using a Dirac Delta function as the weight function). The final "numerical" solution obtained had very good qualitative accuracy and acceptable quantitative accuracy, e.g., about 5 percent on skin friction.

In more recent times, the application of FEM to viscous flow problems has concentrated on the Navier-Stokes equations [6, 7]. Of course, small element sizes are now workable, and this mean that simpler and more general basis functions (often simply linear or quadratic) can be used. Also, more powerful variational constraints than Collocation (or more general weight functions) can be applied. The elliptic character of the Navier-Stokes problem requires in general, the resulting system of equations to be solved simultaneously for the velocities and the pressure. Continuity is treated as a constraint. Baker and Manhardt [8], have applied the FEM to the 2D boundary layer equations in one direction and 2D parabolized Navier-Stokes equations, transforming the system of partial differential equations to a first order, ordinary differential system. Solution of this system is obtained using a finite-difference numerical integration algorithm. This sacrifices some of the advantages of FEM. Dorodnitsyn [9] developed a method for the boundary layer equations transformed such that the usual variables (U,V) are replaced by essentially the local shear as a function of (x, U). This required the use of special interpolation functions. The resulting system of ordinary differential equations was solved by a Crank-Nickolson FDM. Fletcher and Fleet [10] have also applied this method. Here, a full FEM treatment is considered for approximating solutions of the parabolic, boundary-layer equations. The dependent variables are interpolated within each element, and the Galerkin method is applied in order to reduce the interpolation error to zero in a weighted sense. This procedure transforms the governing equations (PDE) to a set of algebraic equations in each element. The parabolic nature of the problem allows the solution of the algebraic system for one column of elements at a time. This leads to tridiagonal or pentadiagonal systems of linear equations, the solution of which can be obtained using very efficient algorithms. This solves one of the biggest problems in using FEM in general, the simultaneous solution of a large number of equations, which is generally associated with high computational cost. Continuity cannot be treated as a constraint anymore. It is now an ordinary differential equation, numerical integration of which yields the required solution at the nodes. Also, the pressure is not an unknown as in FEM treatment of the Navire-Stokes equations.

The FEM was chosen for three main reasons. First, this method has been successfully applied before to the full Navier-Stokes equations. It is efficient and robust. Second, the purely "local" approximations of the phenomena under consideration effectively frees the analyst from traditional difficulties associated with irregular geometries, multi-connected domains, and mixed boundary conditions. Third, applications are firmly rooted in the physics of the problem and for a given accuracy, the resulting equations are better conditioned than those obtained by, say, finite difference approximations of the governing differential equations [6].

The new method is applied to a number of classical problems of laminar boundary layer flows. The accuracy of the method as compared to the theoretical estimates is investigated. Results concerning the effect of aspect ratio of the elements, the type of interpolation functions and the different rules used for the numerical integration of the continuity equation on the accuracy of the solution are presented. The efficiency of the method in terms of CPU time and storage requirements is also discussed.

Equations of motion

For high Reynolds number, attached flow, the boundary layer assumptions lead to the following expressions for the two momentum equations and the continuity:

$$U \frac{\partial U}{\partial x} + V \frac{\partial U}{\partial y} = -\frac{1}{\rho}\frac{dP}{dx} + \nu \frac{\partial^2 U}{\partial y^2} - \frac{\partial \overline{(uv)}}{\partial y} \qquad [A-1]$$

$$\frac{\partial P}{\partial y} \approx 0 \qquad [A-2]$$

$$\frac{\partial U}{\partial x} + \frac{\partial V}{\partial y} = 0 \qquad [A-3]$$

Formulation of the discrete problem

Finite Element Method

The objective of the Finite Element Method is to reduce the continuous problem of the governing equations to a discrete problem described by a system of algebraic equations. To construct the finite element model of the fluid, we subdivide the continuous region of interest into a number of simply shaped regions called elements. Within each element, the dependent variables, here the components of velocity (U,V) are interpolated by functions of compatible order in terms of values to be determined at a set of nodal points. Specifically, let U(x,y) and V(x,y) denote the approximations of the two components of velocity over an element, u_i, v_i the values of velocity at node i of the element, and ϕ_i the interpolation functions over an element. Then, the finite-element approximations over the element can be written in the following form:

$$U(x,y) = \sum_{i=1}^{N} u_i \phi_i(x,y) \qquad [A-4]$$

$$V(x,y) = \sum_{i=1}^{N} v_i \phi_i(x,y) \qquad [A-5]$$

Introducing these approximations in the momentum equation, one gets a set of equations:

$$f_1(\phi, U_i) \;=\; R \qquad [A-6]$$

where R is a residual resulting from the use of the approximations.

The Galerkin Method of Weighted Residuals seeks to reduce these errors to zero, in a weighted sense, by making the residuals orthogonal to the interpolation functions of each element. The Galerkin method, when applied to the momentum equation, leads to the following matrix problem for each element:

$$[K]_e[u]_e \;=\; [F]_e \qquad [A-7]$$

where:

$$K_{\mathrm{ij}}^e \;=\; \int_{\Omega_e} (\tilde{U}\frac{\partial \phi_j}{\partial x}\phi_i \;+\; \tilde{V}\frac{\partial \phi_j}{\partial y}\phi_i \;+\; (\nu + \nu_T)\frac{\partial \phi_j}{\partial y}\frac{\partial \phi_i}{\partial y})dxdy \qquad [A-8]$$

$$F_i^e \;=\; -\int_{\Omega_e} \frac{1}{\rho}\frac{dP}{dx}\phi_i dxdy \;+\; \int_{\Gamma_e} (\nu + \nu_T)\frac{\partial U}{\partial y}\phi_i \eta_y ds \qquad [A-9]$$

where $\tilde{U}$ and $\tilde{V}$ are evaluated using the most recent nodal values. The last term in eqns. $(A-8)$ and $(A-9)$ is the result of the application of the Divergence Theorem on the viscous term. Normally, two iterations are sufficient to determine converged values for U and V.

The general FE method requires the continuity equation to be integrated using weight functions that are one degree lower than the interpolation functions. When linear polynomials are used as interpolation functions, the constant function should be used as weight function. This approach leads to the discrete integral form of the continuity equation. The use of this approach, leads to v components that change sign from one x location to the next. Actually, a von Neumann analysis of the discrete continuity equation leads to an amplification factor equal to -1, which explains the numerical behavior. The problem lies in the treatment of the continuity equation. The character of this equation is now changed, from that of a constraint to that of an initial value problem. Thus, the continuity equation should be integrated along the vertical direction, starting from the known value for the v-component on the lower boundary, after the x-momentum equation is solved for the u-nodal values. The choice of the integration rule used for the continuity equation depends on the accuracy of the elements used.

Two elements have been used in this work. The first one is the 4 node quadrilateral element, with bilinear interpolation of the velocity (see Fig. A-1). The second element attempts to exploit the physics of the problem. Since the gradients in the y-direction are much higher compared to the ones in the x-direction, the element incorporates quadratic interpolation functions in the y-direction and linear functions in the x-direction. The 2D shape functions associated with each node are given as the tensor product of the one-dimensional linear and quadratic interpolation functions. The element,which will be called

QLBL from now on, consists of 6 nodes and is also shown in Fig. (A-1). Some details of these two elements are given at the end of Appendix A.

The numerical evaluation of the integrals in eqns. $(A-8)$ and $(A-9)$ is performed using a quadrature rule compatible with the order of the elements used. For the linear element, a 2×2 quadrature integrats the expressions exactly. In the case of the second element a 2×3 quadrature is used. The K-matrix for each element has dimensions 4×4 for the linear element and 6×6 for the QLBL element. The F-vector has 4 and 6 elements respectively. The values of the nodal unknowns 1 and 4 for the linear element and 1,5 and 6 for the LQ element (see Fig. A-1) are known from the solution of the previous column and thus, they can be applied as boundary conditions in the element level. Modification of the element matrix leads to a 2×2 matrix for the linear element and a 3×3 matrix for the QLBL element. Solution for the column of elements requires the assembly of the element stiffness matrix into a global matrix and assembly of the element force vector into a global force vector. The assembly procedure leads to a tridiagonal system of equations for the nodes on the downstream side of the column in the case of the linear elements, and to a pentadiagonal system in the case of the QLBL elements. The Thomas algorithm is used for the solution of the tridiagonal system. The pentadiagonal system is reduced to upper diagonal form by Gaussian Elimination and then solved by back substitution.

An initial profile for the U and V components of the velocity is required at the first station. On the lower boundary of the domain, the no-slip, no-penetration condition is applied. For the upper boundary, the formulation allows the application of either natural (stresses) or essential (velocities) boundary conditions. Since the solution of the boundary layer equations should be matched with the one given from the inviscid solution, the $U_e(x)$ is used on the top boundary.

The pressure gradient is also imposed from the inviscid solution and is considered constant across the boundary layer. The term appearing on the RHS of equation $(A-9)$ is thus known and is treated as a forcing function.

Implementation of turbulence models

For turbulent flows, a turbulence model must be used. The implementation of the models is straightforward. The FE method requires an eddy viscosity value at the Gauss points, which is provided by the turbulence model.

Unsteady flows

The governing equation for the unsteady flows is as follows:

$$\frac{\partial U}{\partial t} + U\frac{\partial U}{\partial x} + V\frac{\partial U}{\partial y} = -\frac{1}{\rho}\frac{dP}{dx} + \nu\frac{\partial^2 U}{\partial y^2} - \frac{\partial\overline{(uv)}}{\partial y} \quad [A-10]$$

The only difference with the steady one is the addition of the $\partial U/\partial t$ term. For time dependent problems we consider the following form of the finite approximations over an element:

$$U(x,y) = \sum_{i=1}^{N} u_i(t)\phi_i(x,y) \quad [A-11]$$

$$V(x,y) = \sum_{i=1}^{N} v_i(t)\phi_i(x,y) \quad [A-12]$$

The interpolation functions are still considered to depend on the spatial coordinates only, while the nodal values are now depending on time. The Galerkin method, when applied to the momentum equation, leads to the following matrix problem:

$$[M]_e\left[\frac{\partial u}{\partial t}\right]_e + [K]_e[u]_e = [F]_e \quad [A-13]$$

where the K and F matrices are identical with those in the steady flow and M is given as follows:

$$M_{ij}^e = \int_{\Omega_e} \phi_i \phi_j dxdy \qquad [A-14]$$

The aforementioned equation is a matrix differential equation in time. Transformation to an algebraic matrix equation can be obtained by introducing a a family of approximations [2], which can expressed as follows:

$$a\left[\frac{\partial u}{\partial t}\right]_{n+1} + (1-a)\left[\frac{\partial u}{\partial t}\right]_n = \frac{[u]_{n+1} - [u]_n}{\Delta t_{n+1}} \qquad [A-15]$$

The reader should observe that for special values of a, one obtains a number of well-known difference schemes. Writing eqn. ($A-13$) at time t_{n+1} and time t_n, and making use of eqn. $A-15$, one obtains the following expression:

$$\begin{aligned}&\Big[[M] + a[K]_{n+1}\Delta t\Big][u]_{n+1} = [[M] - (1-a)[K]_n\Delta t][u]_n + \\ &[a[F]_{n+1} + (1-a)[F]_n]\Delta t\end{aligned} \qquad [A-16]$$

or

$$[\overline{K}][u] = [\overline{F}] \qquad [A-17]$$

where:

$$\begin{aligned}[\overline{K}] &= [[M] + a[K]_{n+1}\Delta t] \\ [\overline{F}] &= [[M] - (1-a)[K]_n\Delta t][u]_n + [a[F]_{n+1} + (1-a)[F]_n]\Delta t\end{aligned} \qquad [A-18]$$

This system has the same form that the one corresponding to the steady case does. It can thus be solved using the same solver that is used for the steady cases. This concludes the presentation of the algorithm for unsteady cases

Test cases and discussion

To validate the approach presented in this work, two classical problems are presented. These are: a) the laminar flow over a flat plate with zero pressure gradient (Blasius problem), b) laminar flow with adverse pressure gradient (Howarth's problem) [11]. The behavior of the method will be discussed separately for each case.

1. Flow over a flat plate with zero pressure gradient

The Blasius profile at $x/L = 0.0625$ with $\delta/L = 0.02$ was used as an initial condition. The results are shown in Figs. A-2 to A-4, for linear elements. Similar results have been obtained for the QLBL elements. Figures A-2 and A-3 show a comparison between the initial and final nondimensional velocity profiles for the U and V components. Since the solution is self-similar, we expect no changes in the non-dimensionalized profiles. Figure A-4 shows the skin friction coefficient. The agreement is excellent.

This problem is also an ideal case for checking the convergence characteristics of the method, since an "exact" numerical solution exists. The solution was obtained transforming the Blasius equation into a system of three initial value problems. The solution was calculated at discrete points and a cubic spline was used for interpolating for intermediate points. This was required since the error is measured in the L^2 norm, which is defined as:

$$|u_e \; - \; u_{num}| = \left[\int_{\Omega_e} (u_e \; - \; u_{num})^2 d\Omega \right]^{0.5} \qquad [A-19]$$

Figure A-5 shows the convergence rate for the case of linear elements of aspect ratio [dx/dy] equal to 1. Two approaches have been used for evaluating $\tilde{U}$ in equation $(A-8)$ and they are compared to each other. The first uses all the nodal values; the second is equivalent to upwinding since only nodes 1 and 4 (for the linear element) and 1,5,6 (for the LQ element) are used for interpolating $\tilde{U}$ within each element. The advantage of the latter approach is that there is no need for iterative solution; $\tilde{U}$ is evaluated using known values from the last station, and thus the solution time is greatly reduced. Without upwinding, two or three iterations are required at each station to obtain a convergent solution. The results are almost identical. Since, it is known that upwinding reduces the accuracy of the FDM schemes, it should be assumed that this result occurs mainly due to the small gradients in the streamwise direction. The convergence rate agrees with the theoretical result; the global error behaves like h^2. Figure A-6 shows the same comparison for an aspect ratio of 3. Again the results are very close. The CPU time per node was $\approx 2.3 \times 10^{-4}$ seconds. This result was obtained on an IBM 3090.

Convergence rate data for the QLBL element is given in Fig. A-7. For aspect ratio equal to 1, the convergence rate is ≈ 2.95 for no upwinding. This result approaches the theoretical result for quadratic elements. Thus, this element taking advantage of the physics governing the problem, is able to produce a high convergence rate. Upwinding hurts the accuracy of the method for this element. Also, the aspect ratio affects the accuracy, and it is expected that for high aspect ratio (dx/dy), the convergence will be quadratic instead of cubic.

The CPU time per node was $\approx 3.35 \times 10^{-4}$. But, the LQ element was found to be on average, 11 to 13 times faster than the linear element for the same level of accuracy.

2.Laminar flow with an adverse pressure gradient

The solution to the problem of the flow with external velocity $U_e = b_o - b_1 x$ has been given by Howarth [11], in the form of a series. The flow separates somewhere near x/L = 0.96. Unfortunately, the series converges slowly in the neighborhood of separation and sufficient terms have not be obtained to give the point of separation with great accuracy. For our purposes here, the "exact" solution is given by the first 9 terms as in the original paper by Howarth. This problem has also been treated with modern FDM methods by Smith and Clutter [12] Cebeci and Smith [13] and others.

The initial profile was taken as constant, equal to 1.0. The results obtained using linear elements are presented in Figs. A-8 to A-12. Figure A-8 shows a comparison between the analytic and numerical solution for the skin friction coefficient. The comparison is very good and a difference exists only near the separation point, which imight be expected since the location is not well established analytically. Numerical values for the current FEM results are compared with the values, two sets of FDM results and a solution using Gortlet Series in Table 1. Our results compare favorably with other published results for the problem, even though our solution was obtained in the (U, V), (x,y) plane with no special treatment of the leading edge singularity. The uncertainty in the results from all the methods increases near separation. Figure A-9 compares the velocity profiles for (x/L) equal to 0.45 and .90. The agreement is again good. Figure A-10 shows the effect of the aspect ratio of the elements, when dy is kept constant and only dx is allowed to vary. The solution deteriorates as the aspect ratio increases.

The effect of upwinding is shown in Fig. A-11. The solution obtained using upwinding predicts separation later than the solution without upwinding. The consensus of all previous workers is $x/L \simeq 0.96$ as the point of separation. This prediction is closer to the result obtained using the method with no upwinding. A comparison between linear and QLBL elements is shown in Fig. A-12. The comparison indicates that the use of the QLBL element reduces the number of points required across the boundary layer by more than half. The CPU time required for the solution, keeping the number of stations the same in both cases, is reduced by 35 percent.

Table 1 Accuracy of various methods for Howarth's flow: dimensionless wall shear values, $[\tau_w/\rho U_\infty^2]\ (U_\infty L/\nu)^{1/2}$

x/L	Current Work (FEM)	Cebeci-Smith (FDM) (1974)	Howarth series (1938)	Smith-Clutter (FDM) (1963)	Görtler series
0.1	0.948312	0.968524	0.968382	—	0.968781
0.2	0.621218	0.626392	0.626496	0.626249	0.626567
0.3	0.461754	0.462645	0.462801	—	0.462815
0.4	0.358186	0.357197	0.357442	0.357301	0.357427
0.5	0.281123	0.279150	0.279307	—	0.279611
0.6	0.218613	0.216119	0.216728	—	0.217221
0.7	0.164328	0.161602	0.162281	—	0.164296
0.8	0.113563	0.110918	0.111369	0.111546	0.117472
0.88	0.071128	0.068963	—	0.068942	0.082980
0.9	0.059194	0.057228	0.057629	—	0.074667
0.92	0.045898	0.044295	—	0.045254	0.066458
0.94	0.029653	0.028807	—	—	0.058344
0.956	0.008934	0.009863	—	—	0.051917
0.9588	0.001716	0.001602	—	0.006717	0.050798

References

[1] Schetz, Joseph A., *Boundary Layer Analysis*, Prentice-Hall Inc., Englewood Cliffs, 1993.

[2] Reddy, J.N., *An Introduction to the Finite Element Method*, McGraw-Hill, 1984.

[3] Schetz, J. A., 1963, "On the Approximate Solution of Viscous Flow Problems," ASME *J. of Applied Mechanics,* Vol. 30, No. 2, pp. 263-268.

[4] Schetz, J.A., 1966, "Analytic Approximations of Boundary Layer Problems," ASME *J. of Applied Mechanics,* Vol. 33, No. 2, pp. 425-428.

[5] Schetz, J.A., and Janonne, J., 1965, "A study of Linearized Approximations to the Boundary Layer Equations," ASME *J. of Applied Mechanics,* Vol. 32, No. 4, pp. 757-764.

[6] Oden, T.J., and Wellford, L.C., "Analysis of Flow of Viscous Fluids by the Finite-Element Method," *AIAA Journal,* Vol. 10, No 12., pp. 1590-1599.

[7] Gunzburger, M., *Finite Element Methods for Viscous Incompressible Flows: A Guide to Theory, Practice and Algorithms.* Academic Press, Boston, 1989.

[8] Baker, A.J., and Manhardt, P.D., "Numerical Prediction of Mean and Fluctuating Velocities for Jet-Flap Flows," *AIAA Journal,* Vol. 16, No. 8, August 1978.

[9] Dorodnitsyn, A.A., *Advances in Aeronautical Sciences*, vol. 3, Pergamon Press, New York, 1960.

[10] Fletcher, C.A. and Fleet, R.W., 1982, "A Dorodnitsyn Finite Element Boundary Layer Formulation," *8th International Conference on Numerical Methods in Fluid Dynamics,* Aachen.

[11] Howarth, L., "On the Solution of the Laminar Boundary Layer Equations," Proc. R. Soc. Lond., Vol. 164, p. 547, 1938.

[12] Smith, A.M.O., and Clutter, D.W., 1963,"Solution of the Incompressible Laminar Boundary-Layers Equations," *AIAA J.,* No 1, pp. 2061-2071.

[13] Cebeci, T., and Smith, A.M.O., 1974, *Analysis of Turbulent Boundary Layers*, Academic Press, New York.

Interpolation functions for the linear and QLBL elements

The interpolation functions used for the Finite Element Method, written in the local coordinate system with the origin created at the centroid of the element, are:

(a) Bilinear element (see Fig. A-1(a))

Location of nodal point in the local system

1 (-1, -1)

2 (1, -1)

3 (1,1)

4 (-1,1)

$$\phi_1 = \frac{1}{4}(1-\xi)(1-\eta)$$
$$\phi_2 = \frac{1}{4}(1+\xi)(1-\eta)$$
$$\phi_3 = \frac{1}{4}(1+\xi)(1+\eta)$$
$$\phi_4 = \frac{1}{4}(1-\xi)(1+\eta)$$

(b) Quadratic element (see Fig. A-1(b))

Location of nodal point in the local system

1 (-1, -1)

2 (1, -1)

3 (1,0)

4 (1,1)

5 (-1,1)

6 (-1,0)

$$\phi_1 = -\frac{1}{4}(1-\xi)(1-\eta)\eta$$
$$\phi_2 = -\frac{1}{4}(1+\xi)(1-\eta)\eta$$
$$\phi_3 = \frac{1}{2}(1+\xi)(1-\eta^2)$$
$$\phi_4 = \frac{1}{4}(1+\xi)(1+\eta)\eta$$
$$\phi_5 = \frac{1}{4}(1-\xi)(1+\eta)\eta$$
$$\phi_6 = \frac{1}{2}(1-\xi)(1-\eta^2)$$

The interpolation functions are given over the square master element, since evaluation of the integrals of Eqs. (A-8, A-9) are easily performed over the element. The mapping corresponds each point (x,y) of each element of the general FEM mesh to a unique point of the master element. The mapping can be written as:

$$x = \sum x_i\phi_i$$
$$y = \sum y_i\phi_i$$

where x_i and y_i are the coordinates of the nodal points. Details about the numerical evaluation of the integrals can be found in any general book on the Finite Element Method [2].

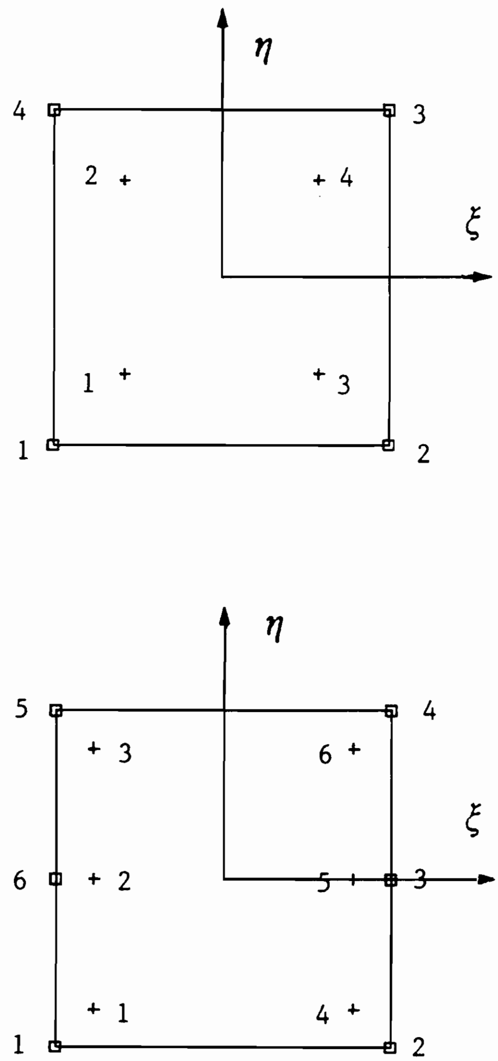

Figure A-1. : Linear and QLBL master elements. Numbering conventions for the nodal and quadrature points.

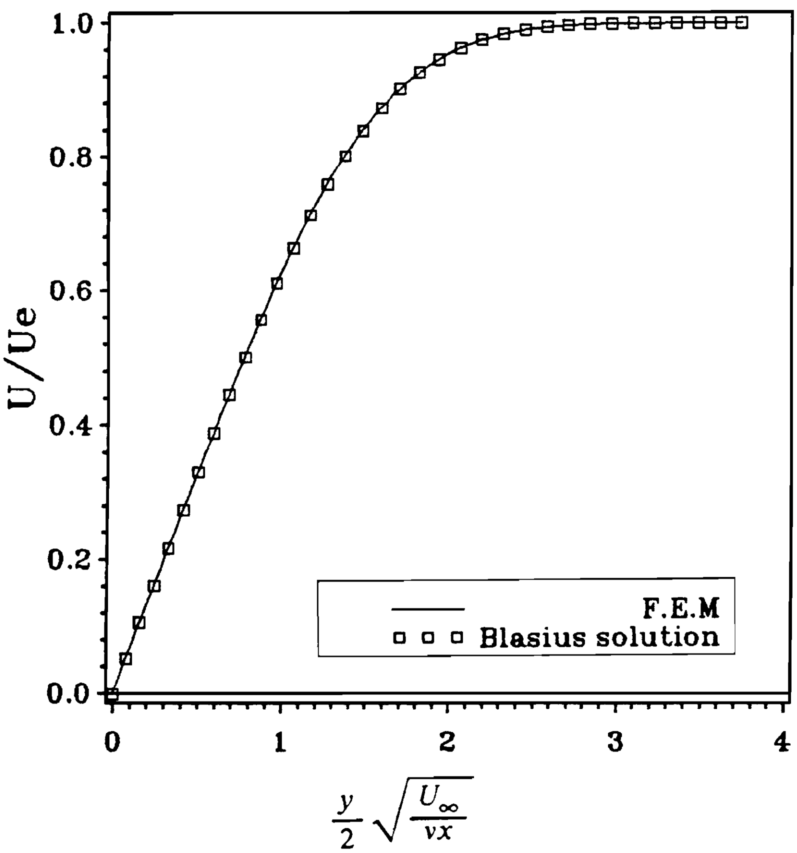

Figure A-2. : U-profiles for the laminar flow over a flat plate.

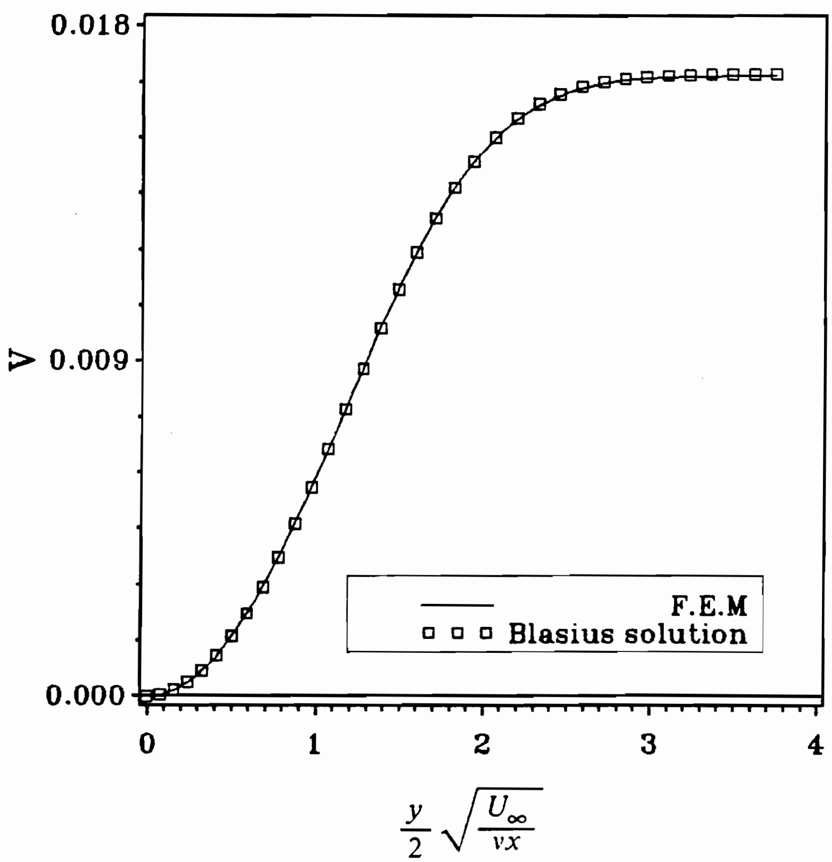

Figure A-3. : V-profiles for the laminar flow over a flat plate.

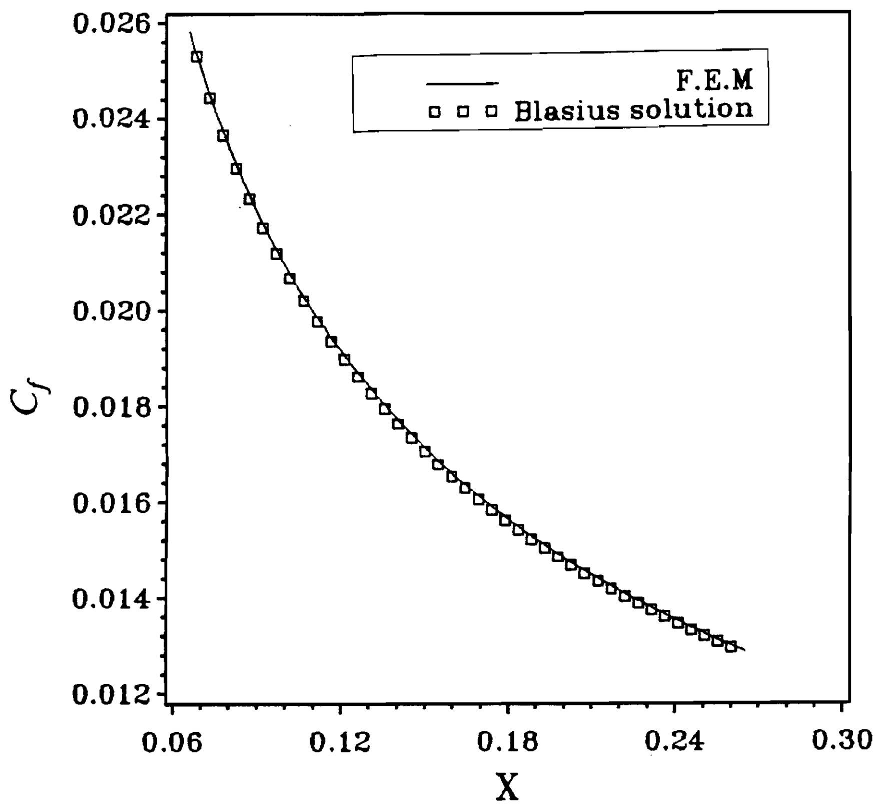

Figure A-4. : Skin friction coefficient for laminar flow over a flat plate.

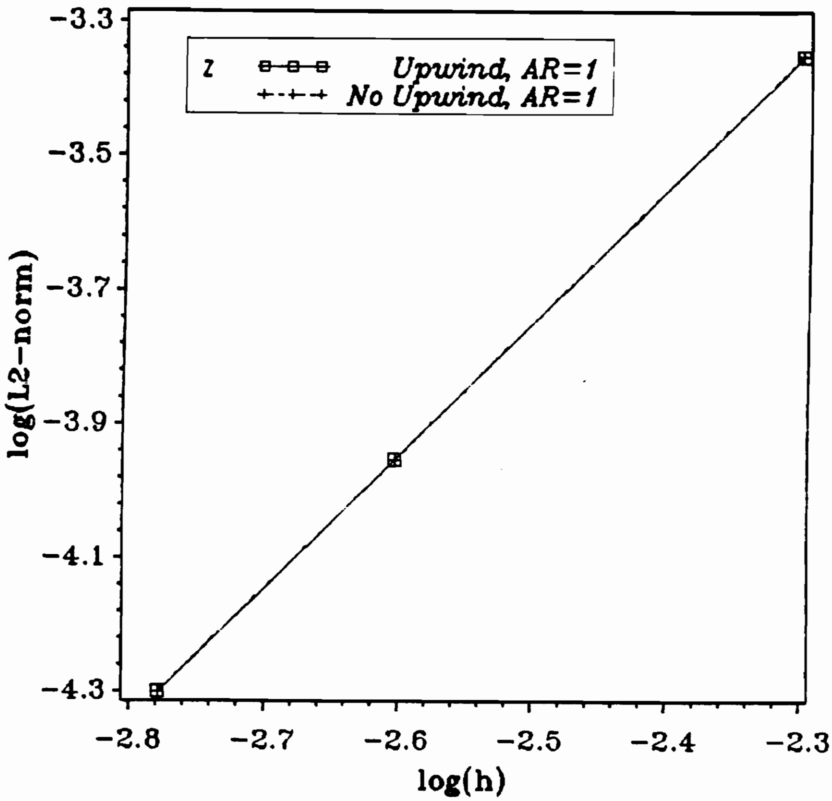

Figure A-5. : L-2 norm versus characteristic dimension of element. Uniform grid, linear element for Blasius problem.

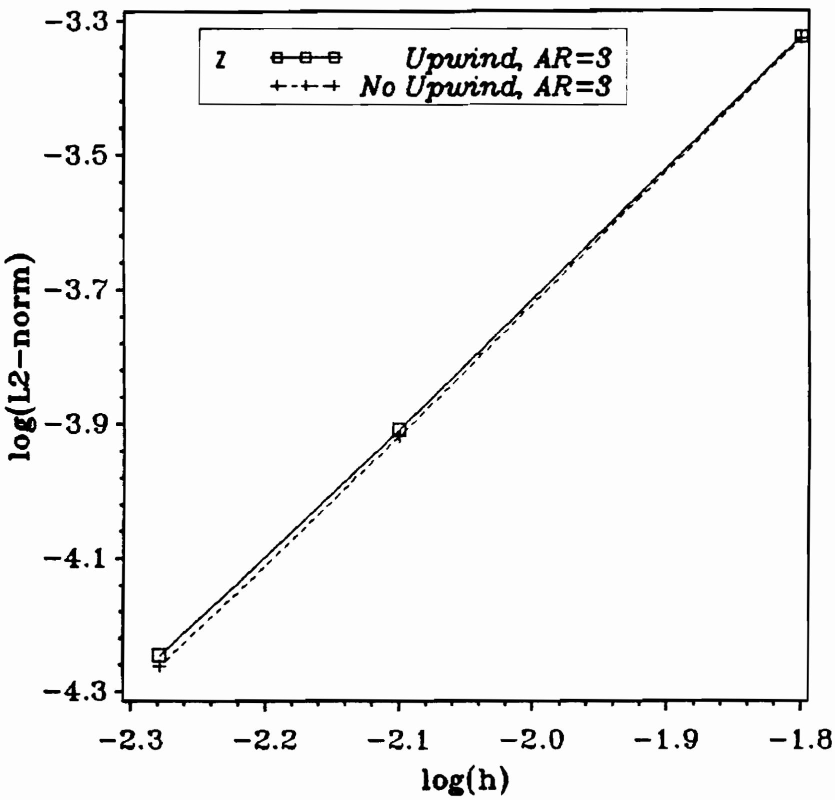

Figure A-6. : L-2 norm versus characteristic dimension of element. Linear elements, AR = 3 for Blasius problem.

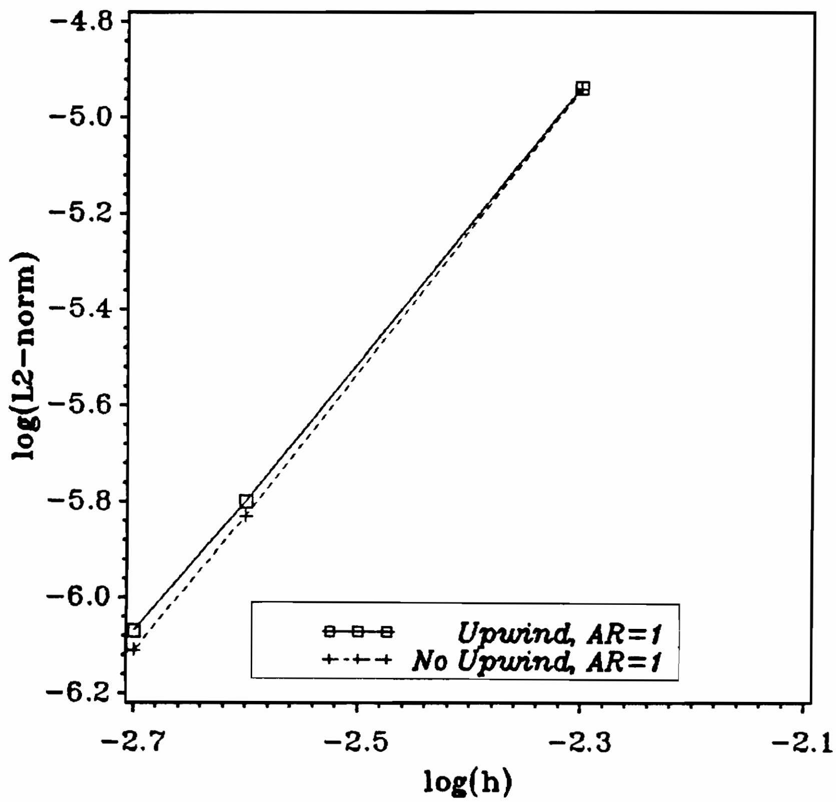

Figure A-7. : L-2 norm versus characteristic dimension of element. Uniform grid, QLBL elements for Blasius problem.

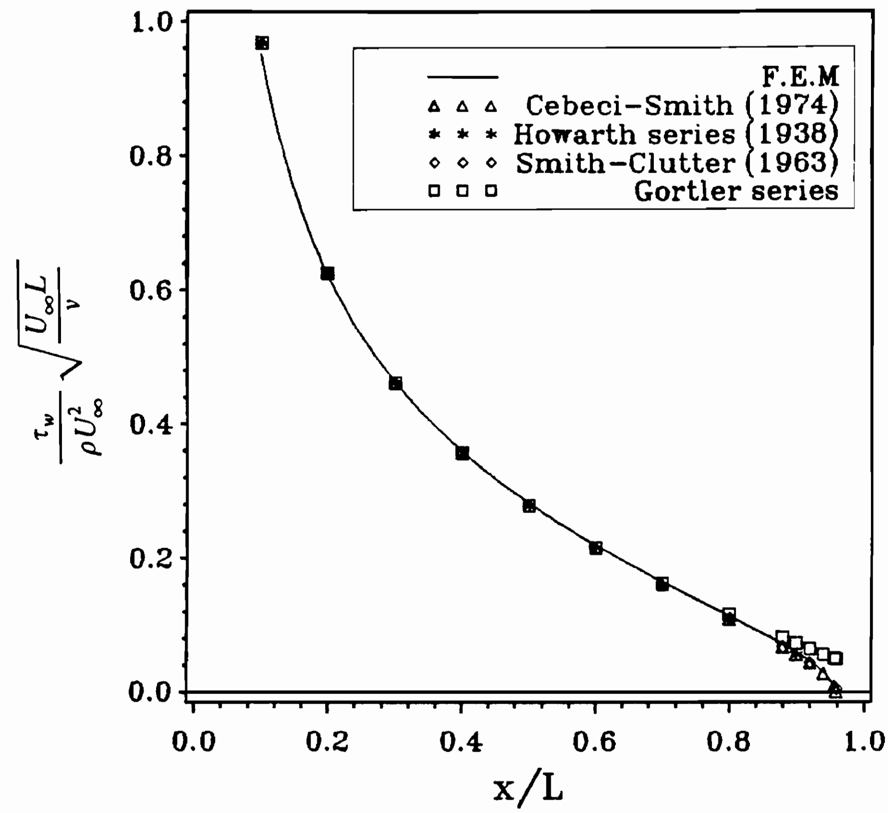

Figure A-8. : Nondimensional wall stress for the Howarth problem.

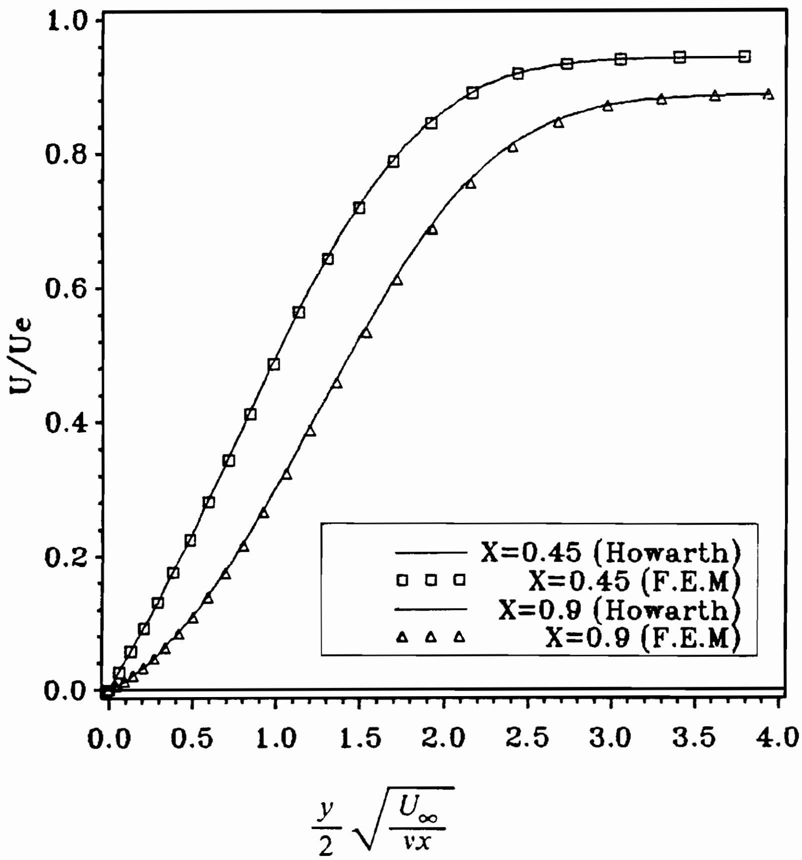

Figure A-9. : U-velocity profile for the Howarth problem.

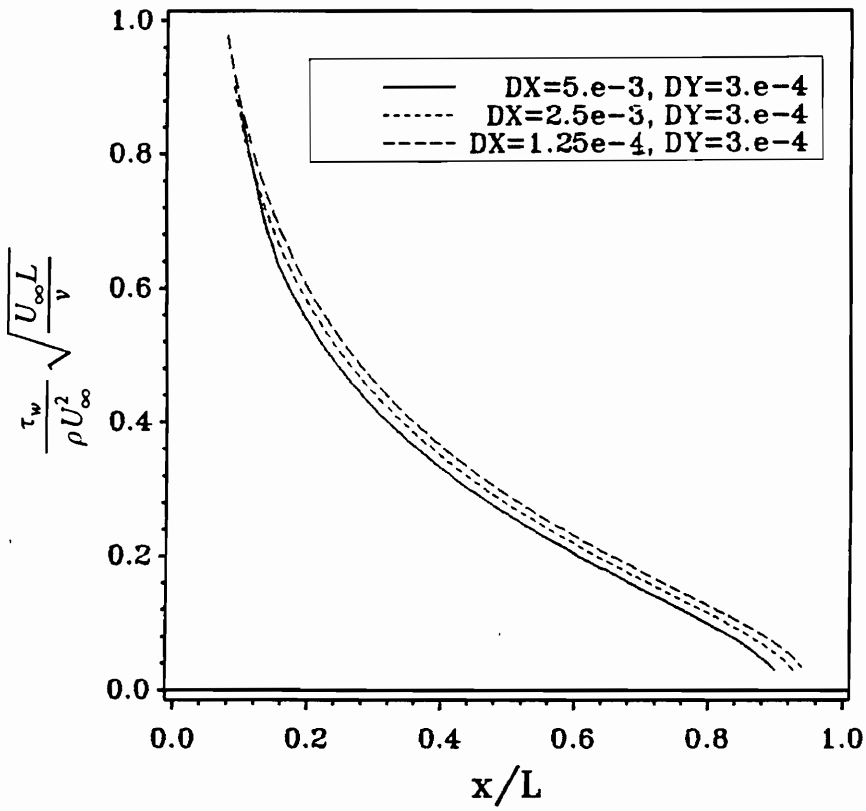

Figure A-10. : Effect of the aspect ratio. dx = varying, dy = constant for the Howarth problem.

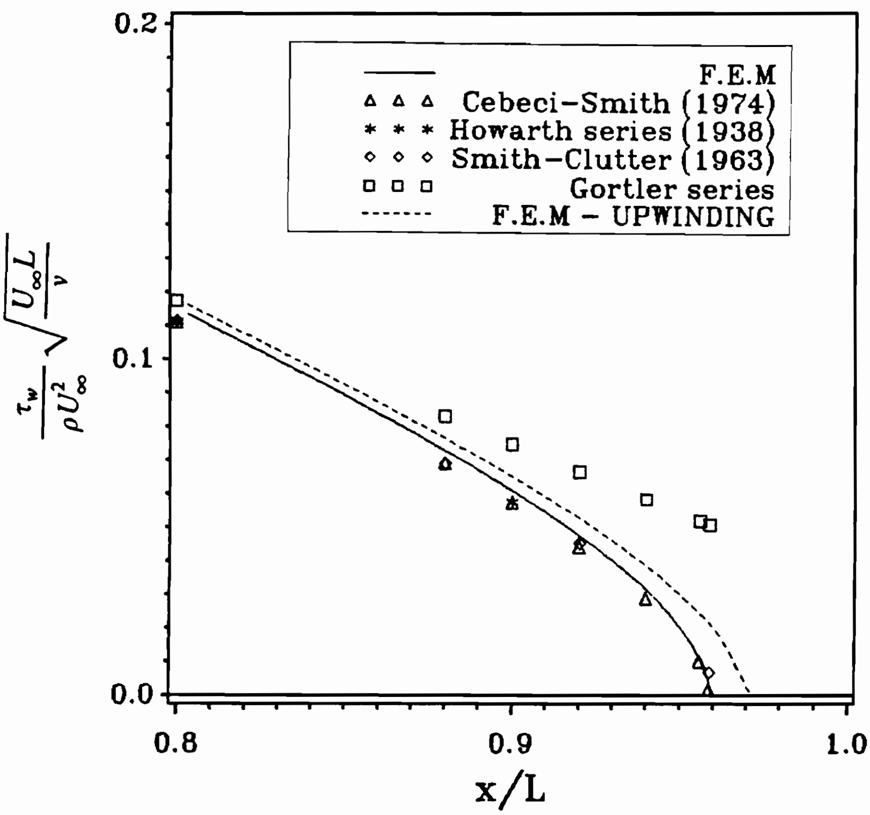

Figure A-11. : Nondimensional wall stress for the Howarth problem. Upwinding versus non-upwinding.

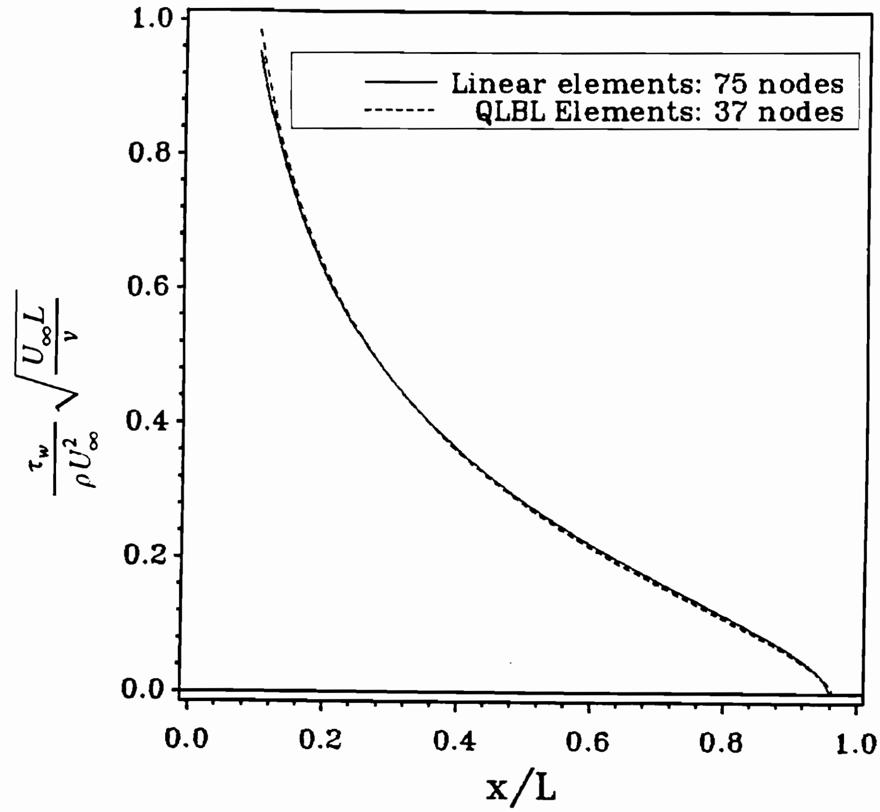

Figure A-12. : Nondimensional wall stress for the Howarth problem. Linear versus QLBL elements.

Appendix B.

Introduction

The physics of a separated flow differ considerably from that of an attached boundary layer. As the adverse pressure gradient increases in strength, the near wall flow decelerates until some backflow first occurs. The large-scale eddies supply the turbulence energy and momentum to the near wall detaching flow. The production of of T.K.E. in the near wall region is negligible. Diffusion and dissipation are the dominant terms. The velocity fluctuations in the backflow region are greater than or at least comparable to the mean backflow velocities. These fluctuations are mainly due to turbulence within the detached flow. Although the outer region mean velocity profiles look like those for a free mixing layer, the inner third is substantially different [1]. The law of the wall shearing type of mean velocity profile that uses the wall shear as a characteristic velocity is not applicable for the backflow. An extensive review of the physics of separated flows can be found in [1,2].

Modeling ideas for the separated zone

The modeling of the separated zone must be accomplished using two zones. The inner zone will be extended up to the point where the velocity U is equal to zero. The height from the wall where this occurs is denoted by δ_b. In this region, the mixing length and eddy viscosity ideas have no physical meaning. The near wall velocity profile presented in [3] that collapses most of the experimental data can be used as a building block. The equation is:

$$\frac{U}{|U_N|} = 0.3\left(\frac{y}{N} - \ln \left| \frac{y}{N} \right| - 1 \right) - 1$$

which is valid for $0.02 < y/N < 1.0$ and

$$\frac{U}{|U_N|} = -C\left(\frac{y}{N} \right) + \frac{P_1}{2}\left(\frac{y}{N} \right)^2$$

which is valid for $y/N < 0.02$. In the previous expressions, the symbols have the following meaning:

U_N Maximum negative velocity

N y location from the wall where the negative velocity is maximum

C constant

P_1 $\dfrac{N^2}{\rho \nu |U_N|} \dfrac{dP}{dx}$

This expression is not valid all the way to δ_b. Thus a polynomial expression ($U = f(y)$) must be used between N and δ_b. This polynomial expression must satisfy the following conditions:

$$f(N) = U_N$$
$$\frac{\partial f}{\partial y}(N) = 0$$
$$f(\delta_b) = 0$$
$$\frac{\partial f}{\partial y}(\delta_b) = \frac{\partial U}{\partial y}\Big|_b^{outer}$$

These conditions indicate that a cubic profile is the lowest order profile that can be used.

For the outer region, the approach presented for the attached portion of the flow can be used. The maximum shear stress is still the correct scaling parameter, thus the auxiliary equation that predicts its variation can be used. The mixing length approach can also be used in the outer region of the flow. This gives us a way of relating the turbulent shear stress to the mean velocity profile. This model must provide the value and the derivative of turbulent shear stress at δ_b as well as the derivative of the mean velocity profile at the same location. The derivative of the shear stress is needed for evaluating an entrainment velocity of the form:

$$V_{re} = 0.6 \frac{l_m}{K^{1/2}} \frac{\partial K}{\partial y}\Big|_{\delta_b}$$

This equation can be expressed in terms of the maximum shear stress following the ideas presented earlier. The value of the entrainment velocity must be equal to the integral of the velocity profile in the backflow region. This entrainment relationship is the link between the variables of the inner and the outer region.

The evaluation of the integrals of the auxiliary equation need special consideration. The production of T.K.E. in the backflow region is almost zero, and the dissipation is almost equal to diffusion. Integration of the auxiliary equation across the boundary layer eliminates the diffusion term, but the dissipation term still remains. The expression that was used before for the dissipation is not valid in the backflow. This creates a problem that must be addressed first.

References

[1] Simpson, R.L., "A review of Two-dimensional Turbulent Separated Flow Calculation Methods," in *Boundary-Layer Separation,* IUTAM Symposium London 1986, F.T. Smith, S.N. Brown, (Eds.), Springer-Verlag Berlin, Heidelberg 1987.

[2] Simpson, R.L., "Two-Dimensional Turbulent Separated Flow," AGARDograph No. 287, Vol. 1, June 1985.

[3] Agarwal, N.K., and Simpson, R.L., "Backflow Structure of Steady and Unsteady Separating Turbulent Boundary Layers," *AIAA J.*, vol. 28, No. 10, 1990.

Vita

Evangelos Hytopoulos was born in June 1965 in Athens, Greece. He studied Naval Architecture and Marine Engineering at the Technical University of Athens and obtained his Diploma in 1988. The same year, he enrolled at VPI & SU in the Aerospace & Ocean Engineering department. He received his Master's degree in Aerospace Engineering in May of 1990, under the direction of Dr. Joseph A. Schetz. With Dr. Joseph A. Schetz and Dr. Roger L. Simpson as his advisors, he completed his doctoral work in February of 1994. Mr. Evangelos Hytopoulos is currently employed with Automated Analysis Corporation in Ann Arbor, Michigan. Mr. Hytopoulos is a member of the Society of Naval Architects and Marine Engineers (SNAME) and the American Institute for Aeronautics and Astronautics (AIAA).